Cast solidification structures of high aluminium steels

Neil Hollyhoke

A thesis submitted in partial fulfilment of the degree of Doctor of Philosophy

University of Warwick, WMG

September 2018

0.1 Contents

0.2 List of Figures

0.3 List of Tables

0.4 Acknowledgements

Thanks to my supervisors, Carl Slater, Claire Davis and Sridhar Seetharaman, the people at TATA IJmuiden for both providing input and materials, and other staff and students at the University of Warwick, particularly those that provided much needed breaks, the rest of the Steels Processing Group and everyone else involved in maintaining the WMG workshops and labs.

0.5 Declaration

This thesis is submitted to the University of Warwick in partial fulfilment of the requirements for the degree of Doctor of Philosophy.
The author declares that except where acknowledged, the work contained in this thesis is his own work and has not been submitted for a degree at any other university.

0.6 Related Work

This is a list of work published elsewhere based on the same results as the contents of this thesis
Materials World, October 2017, Use of the CLSM as a novel SDAS measuring technique

SP17 Conference Proceedings, p322, Columnar Grain Competition in Low Density Steels

Ironmaking and Steelmaking: Processes, Products and Applications - The influence of alloy composition on the as-cast grain structure in near net shape low density steels (Secondary author)

Columnar Grain Competition during Solidification in Low Density Steels – Due to submit

0.7 Abbreviations and names

CC – Continuous cast.

CASTRIP – A twin roll casting process developed by NUCOR and seeing some limited use in the United States.

MEFOS – A Nordic research group with a trial single belt caster.

CLSM – Confocal laser scanning microscope.

LDS – Low density steel, typically one or more of the grades below.

BH - Bake hardenable LDS, sample VS5578B.

Nano 1 / N1 - Nano precipitate hardened LDS, sample VS5579A.

Nano 2 / N2 - Nano precipitate hardened LDS, sample VS5579B.

SDAS – Secondary dendrite arm spacing.

Grain Width – The distance across a columnar grain perpendicular to the growth direction, as opposed to the grain length which often exceeds the size of the samples used.

EBSD – Electron Backscatter Diffraction, a technique available in scanning electron microscopes to characterise crystallographic properties of a sample.

PF – Pole Figure, a complete description of the orientation data of a sample.

IPF – Inverse Pole Figure, a method of displaying the distribution of grain orientations in a sample, simpler to read than a pole figure but at the cost of losing some data.

CALPHAD – Calculation of phase diagrams, the mathematics of generating phase diagrams for materials based primarily on thermodynamic properties

Thermo-Calc – Software for simulating the development of materials based on the CALPHAD approach

DICTRA – DIffusion Controlled TRAnsformations, an add-on to Thermo-Calc that includes kinetics and is intended for simulating diffusion controlled processes

MICRESS – MICRostructure Evolution Simulation Software, software for simulating materials using phase field theory

RNG – Random Number Generator, computer code that produces a series of (pseudo)random numbers with a chosen distribution across a given range.

FEM – Finite element modelling, a method of modelling systems by using a mesh to break them up into small sections which is then solved approximately and these approximations recombined

COMSOL – Software that uses the FEM to model systems, it includes the ability to produce geometries and then take material properties from a database and is then able to model a wide range of physical changes

0.8 Abstract

Low density steels (LDS) are of industrial interest as lightweight vehicle body panels to improve fuel efficiency. However, they are difficult to manufacture using conventional steel processing: for example they suffer from the formation of large grain sizes during solidification, which affects hot ductility causing cracking. Alternative processing, such as twin roll or belt casting, with higher cooling rates offer options for casting these grades. It is important that the effects of composition and cooling rate on the solidification structures (secondary dendrite arm spacing, and grain size development) are understood, as has been considered in this thesis, specifically for LDS, but also the more general applicability of the approach to other grades of steel.

A new technique (using a confocal scanning laser microscope, CLSM) for SDAS measurements based on in situ observation of the metals surface during solidification is described and verified by comparison to bulk solidification measurements for both the LDS grades and 304 stainless steel, giving confidence it is suitable for wider application. The main benefit of this technique is that it can be used on grades where conventional techniques for ex-situ room temperature characterisation can not be applied, for example where phase transformations alter the microstructure removing evidence of solidification structures. SDAS values with respect to cooling rate were obtained for the LDS using the CLSM, however it was found that grain size measurements could not be made as the sample size / field of view was too small considering the grain sizes in the materials.

EBSD grain analysis was used to characterise the development of grain sizes and misorientation ranges through the columnar region for laboratory ingot castings which gave a range of cooling rates that covers both conventional casting techniques and near net shape techniques. It was found that the bake hardenable LDS had a very narrow mushy zone and very large grain width, whist the nano-precipitate strengthened LDS had a wider mushy zone and relatively finer grain width on solidification. For both steels the grain width increased with depth into the cast ingot due to grain competition. Relationships between the cooling rate and rate of columnar grain competition, and the rate of competition and SDAS:mushy length ratio are proposed based on these results.

The modelling section discusses the development of a model in MICRESS to simulate the solidification of the LDS with respect to cooling rate with the intent that it can be more broadly applied to other grades, this is then tested against a TWIP grade. There were some discrepancies between the simulations and experimental results, suggested to be due to 2d compared to 3d effects, however the trends of grain coarsening were broadly similar, giving the current model qualitative predictive capacity that appears to be generally applicable to different grades undergoing single phase (delta ferrite or austenite) solidification.

The hypothesise developed during study of the LDS with respect to the effect of cooling rate on solidification structure were tested against the TWIP results, using laboratory and commercial cast samples. while relating coarsening rate to cooling rate directly did not carry over to this new grade, the TWIP results are consistent with the SDAS:mushy length based hypothesis, suggesting an avenue for further study and potentially advancing understanding of metallic solidification in general.

0.9 INTRODUCTION

Global annual continuous cast steel production is in the region of 1.5 billion tonnes, accounting for 96% of steel production, with two-thirds of the continuous cast material produced in Asia and 10% in the EU, to which the UK contributes 7.5 million tonnes. Using conventional techniques typically generates about 2 tonnes of CO_2 per tonne of steel, using 20GJ/t (WorldSteel.org 2016) (WorldSteel.org 2017). With such high production volume and energy requirements, techniques that offer 80+% savings in energy consumption are going to be used at every available opportunity, for both financial and environmental benefits. Therefore, the challenge is to understand how to best make use of these new techniques.

Steels have achieved this enormous production volume by being a vitally important class of materials. Due to the diverse range of potential properties and relative cheapness, they are used in a large number of applications - from large heavy-duty structures and vehicles, to every day handheld items. While cheaper than many other materials, conventional sheet steel production currently involves casting in the range of 200mm thick before rolling down to the desired thickness. There is a large cost in energy expenditure during this secondary processing; this inefficiency needs to be addressed in order to remain competitive against potential alternative materials, especially for thinner gauge products. Several direct or near net shape casting processes are being developed which, while technically challenging, offer the opportunity to cast steels with thicknesses in the range of 1-15mm, allowing for large savings on energy consumption for thinner gauge products. These facilities also have a significantly smaller footprint than conventional steel casting plants and require less start-up capital. These processes result in very high cooling rates during solidification, far from equilibrium (in the range of 10^2 to 10^4 K/s) (Sosinsky et al. 2008) (Daamen et al. 2014), and with different geometries to the casting process (e.g. horizontal belt casting compared to vertical to horizontal transition for conventional continuous casting). This, firstly, opens up the possibility for the production of novel steel grades that are difficult to manufacture with conventional casting methods, and, secondly, requires extensive research into the cooling process and final microstructures produced, in order to ensure products are suitable for their intended applications. This thesis presents research that used a combination of experiment and modelling to look at the microstructure of several grades of high aluminium steel at moderately fast cooling rates, beyond those which are achievable by conventional casting methods, eventually leading to an evaluation of their suitability for bulk production using the new casting techniques. An intended use for these steels is vehicle body panels, since the high Al content makes them lower density and similar strength levels can be achieved, improving the fuel efficiency of the vehicles.

Since these steels are likely to be best suited to high volume products but are unsuitable for established high volume production methods, relatively little work has been done on them and interest is only starting to grow now, as more suitable mass production techniques approach maturity.

Literature Review

Section 1 – Manufacturing Methods

Section 1 will look at the various processes used in manufacturing steel products. After a brief look at ingot casting, more attention will be paid to conventional continuous casting methods in order to effectively contrast them with the direct casting methods discussed afterwards. Particular attention will be paid to twin roll casting and horizontal belt casting, since these methods are currently the most promising for commercialisation and are the furthest developed.

Traditional methods

1.1 Ingots

Ingot casting has been surpassed by other casting techniques for most products, only making up around 3% of produced steel. However, it is still used for low volume specialist grades and a small number of heavy duty single piece components, such as the pressure vessels used in nuclear power plants (Pickering 2013), and it still acts as a good example of a typical solidification microstructure. In ingot casting, a large amount of liquid metal is poured into a mould and left to cool over a period of time which lasts from hours to days. This slow cooling means that the ingot has large grains and cools at close to equilibrium conditions, thus closely following the segregation behaviour expected from tracing its path through the phase diagram or using common models that predict segregation based on equilibrium conditions, such as the Scheil equation. The specifics of solidification are discussed in section 2. Ingots show a specific pattern of microstructures throughout their sections, shown in

Figure 1. At the mould surface is the 'chill zone', where relatively rapid cooling from contact with the mould produces a fine, randomly orientated grain structure. This gives way to the 'columnar zone', where directional dendrite growth takes over, which, since the dendrites growing perpendicular to the surface progress deepest fastest while more angled dendrites hit the sides of other dendrites that have already grown past them, creates the collection of parallel long narrow crystals growing into the material. Eventually there is the 'equiaxed zone' in the centre, where dendrite arms that have been broken off by convection, alongside other nucleation points, are scattered throughout the remaining liquid, causing a structure made of large, randomly oriented grains (Krauss 2003).

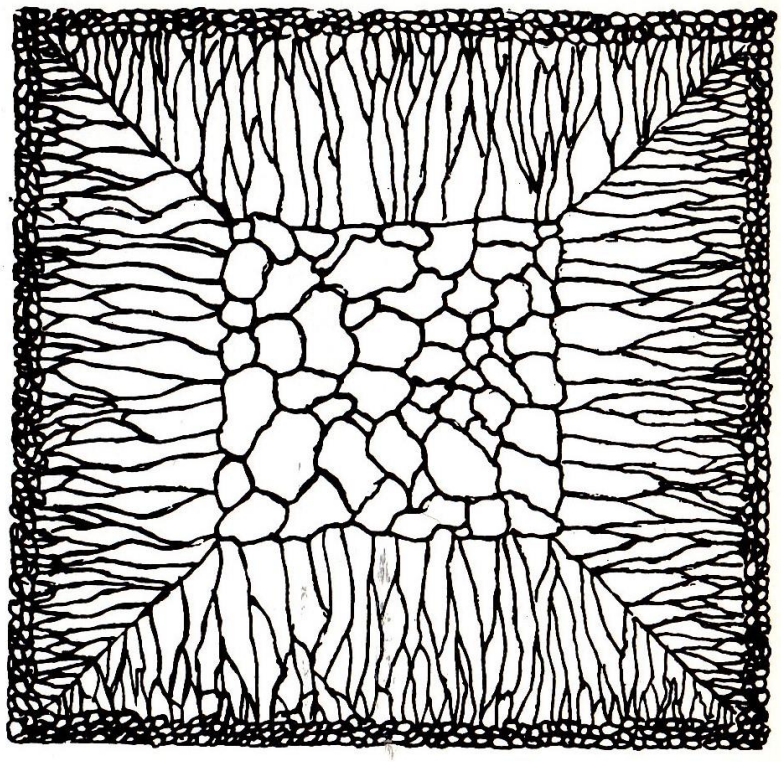

Figure 1 Typical continuous cast grain structure (Flemings 1974)

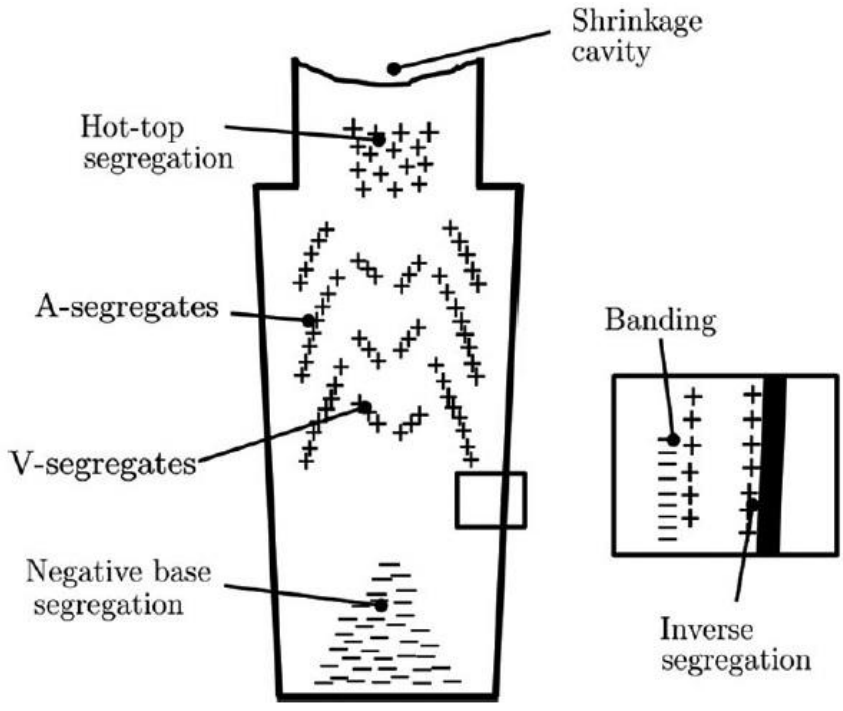

Figure 2 The segregation pattern found in ingots. (Pickering 2013)

There can be significant but predictable negative characteristics in ingot casts, for example various segregation patterns forming due to the slow cooling rate, these patterns are shown in *Figure 2*.

While the patterns of segregation are discussed here, the underlying mechanisms are discussed in Section 2, which deals with the details of solidification. The centre of ingots shows several standard macrosegregation patterns. Early forming equiaxed dendrites can break off and, since they are denser than the surrounding liquid phase, then have enough time to settle to produce a region of negative segregation (more of the bulk element and less of the alloying elements) towards the bottom of the ingot. Interdendritic flow leads to positive segregation (greater concentrations of alloying elements) in diagonal bands higher up in the ingot. There is also a region of positive segregation near the top centre - this is the final solidifying material. (Pickering 2013) *Figure 3* shows examples of C segregation through the depth of 8 tonne steel ingots with a variety of compositions (Yamada et al. 1995), showing that the concentration of carbon in the centre can be two to three times higher than near the surface.

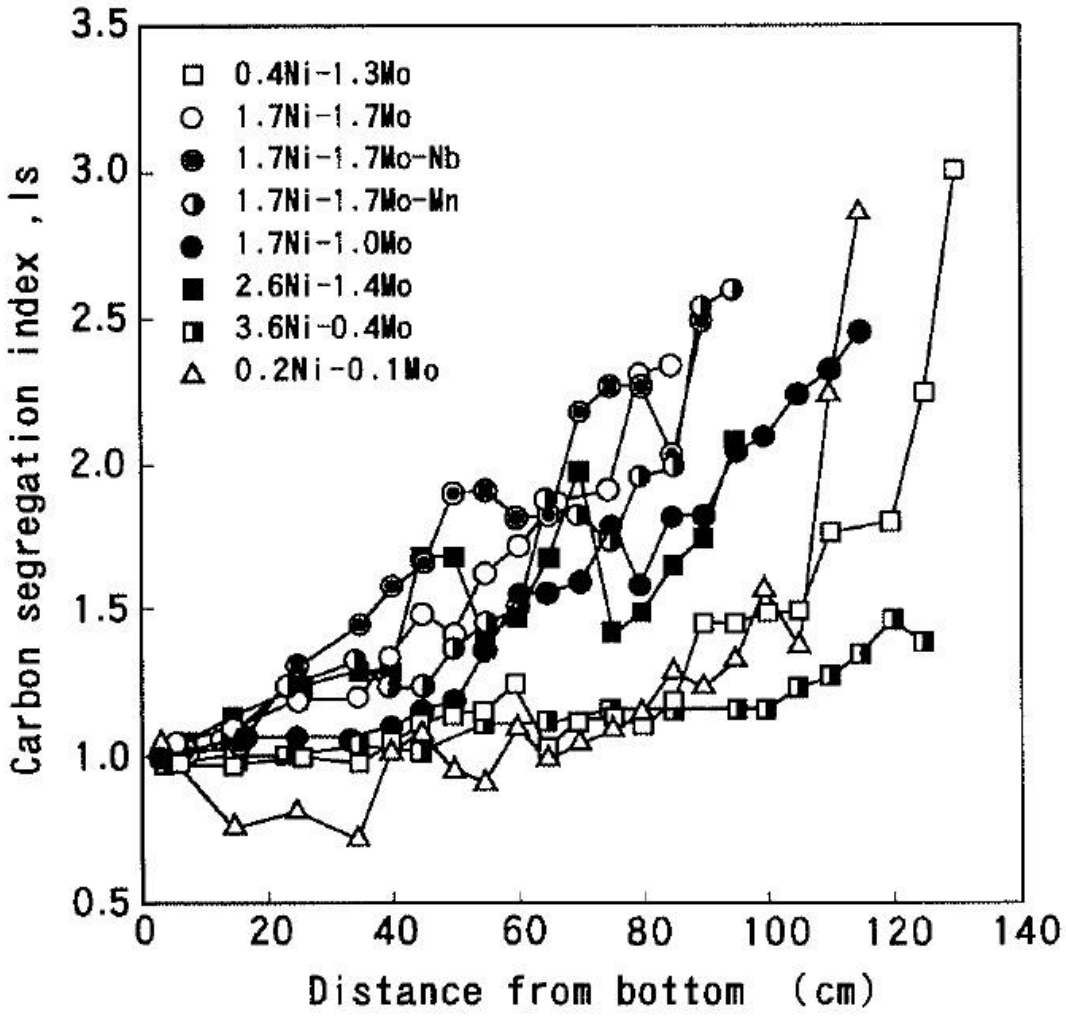

Figure 3 C segregation patterns for a selection of steel compositions (Yamada et al. 1995)

1.2 Continuous casting

Conventional continuous casting (as shown in *Figure 4*) produces a continuous piece of steel of a fixed cross section, but with a theoretically infinite length. A variety of cross-sectional shapes and sizes are

possible (BJJD 2010), but most of this work will focus on slab casting due to its high relevance for comparing to direct casting techniques and the intended uses of the grades studied. Continuous cast slabs are typically 800-1600mm wide and 120-250mm thick, although some facilities produce slabs that are either thicker or wider than this, and thin strip facilities produce slabs down to about 50mm thick (Liu, Li and Tsukihashi 2015). Ladles of molten steel are poured into a tundish, which maintains a steady stream of steel out into a bottomless mould. The mould allows a surface layer to freeze and become sufficiently thick to support itself against the liquid in the centre, prevent any leaking as the steel passes out of the mould and is further cooled by water jets. The mould is also vibrated parallel to the liquid flow and a lubricant/mould flux is used. Both of these measures are in order to prevent sticking, but also come at the cost of reducing contact between the mould and the solidifying steel, therefore drastically reducing heat flow. Since relatively little of the steel surface is exposed to the atmosphere while at very high temperatures, there is no need to control the atmosphere - this is in contrast to the direct casting techniques discussed later where the material is thin enough that losing surface material to oxides sacrifice a significant fraction of the produced material. Microporosity can occur in the centre of castings as solidification finishes, when the dendritic structures are advanced enough to hinder fluid flow, and the contraction of the liquid as it solidifies causes micropores due to the lack of a reservoir of liquid to refill the gaps left by contraction. This is more prevalent in grades with wider mushy zones (Piekarski 2010). However, this is mitigated by soft reduction late in the solidification process (the L2 region in Figure 4), where the steel is passed through rollers to slightly reduce its thickness - this 'soft reduction' technique prevents both voids and reduces segregation developing along the centreline.

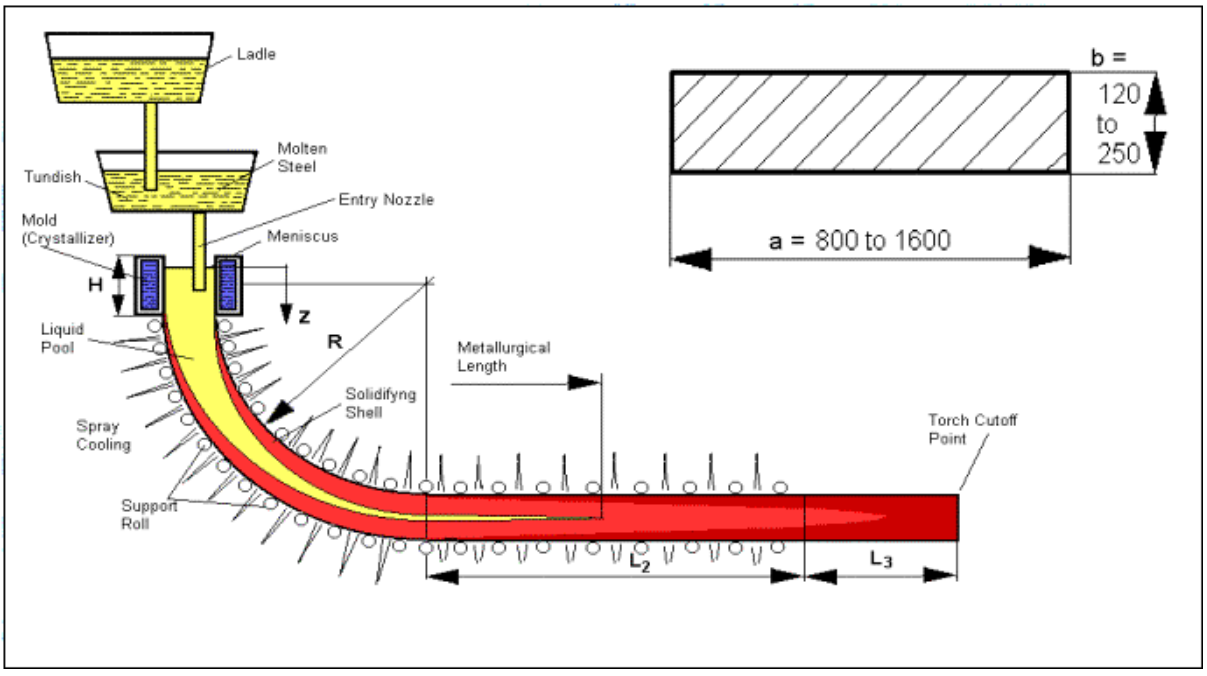

Figure 4 Schematic of the conventional continuous casting process (BJJD 2010)

In the same region, between a suitably thick solid shell forming and complete solidification occurring, the steel is gently curved until it is horizontal, providing space for further working of the material. This bending can lead to hot tearing, a type of cracking where cracks form in the semi solid region because the dendrites contains a network of weak points (liquid pockets) and impedes fluid flow, meaning the remaining liquid cannot flow freely to fill the gaps that form.

Since atoms along grain boundaries are less strongly bound than atoms in the bulk lattice, strain tends to concentrate along grain boundaries. In grades with particularly large grains, such as high Al steels the relatively small number of boundaries means that each individual boundary is far more likely to suffer excessive strain causing plastic deformation, and cracking.

The outside of the curved material suffers tensile stress during bending, while the inside is under compressive stress, when straightening these are reversed. The regions under tensile loads are the ones prone to cracking (Calvo et al. 2007). The magnitude of the tensile load is proportional to some function of the thickness of the steel along the radius of curvature and is inversely proportional to that radius - this means that thinner castings can have greater curvature, making the process easier, although temperature and composition also play an important role. This also means that regions under tensile loads that are most prone to failure, due to hot tearing of semi solid steel, or at lower temperatures due to other factors which lower the ductility of the solidified steel – this is discussed next.

Ductility will tend to gradually decrease as the steel cools, corresponding to an increase in crack susceptibility, but for many materials there is a region called the ductility trough (*Figure 5*) - in this region, inconsistencies in the changing microstructure make the material far more prone to cracking. This is particularly relevant for thick cast materials, because the thickness of the material means that different depths are at different temperatures, making it more likely that one of the discussed mechanisms (below) will be occurring in part of the material and initiating potential routes of failure, or at least weakening of the material. While there are several different mechanisms affecting ductility (Connolly, Paules and DeArdo 2015), they all rely on a relatively strong bulk with a small amount of softer material spread in a network throughout the material - in steels this can be the austenite to ferrite transition, an uneven precipitate distribution, or segregation, particularly of light residual elements such as phosphorus. The relevance of different mechanisms varies with steel grade, but at least three mechanisms have been proposed - precipitate distribution, local

solidification fraction, (Ridolfi 2014) (Bellet et al. 2009), and phase transformation (Li et al. 1999) (Kato et al. 2003).

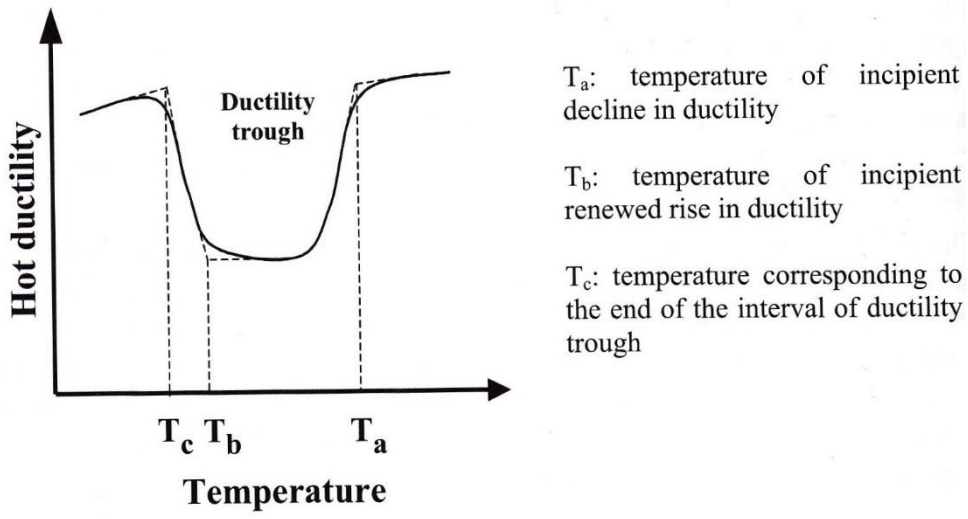

Figure 5 Schematic of ductility variation across a ductility trough. (Rodriguez-Ibabe 2007)

In the case of the phase transformation mechanism, there are two phases present with different mechanical properties, where the softer of the two (ferrite in steels) will deform more readily, leading to strain concentration and a collection of voids which coalesce into cracks. The worst-case scenario here is the austenite to ferrite transformation, where the ferrite grains nucleate on the austenite boundaries, creating an interconnected web of ferrite along the prior austenite grain boundaries, allowing cracks to propagate large distances. However, in industrial settings, the major deformation from bending during continuous casting is more likely to be present during the high temperature delta-ferrite to austenite transition, where the islands of ferrite are separated from each other by the newly forming austenite, meaning many small cracks can develop, but they are less likely to connect on a large scale. Nevertheless, these small cracks throughout the steel still compromise the material by creating stress focusing points. When precipitates are the primary factor, the bulk of the steel is hardened by many small precipitates, but the strain causes preferential precipitate growth directly on grain boundaries, depleting the material near the boundary and restricting precipitate nucleation nearby. This makes the material near grain boundaries softer, and the thin layer of softer material once again suffers the bulk of the strain, leading to voids forming around the grain boundaries (Rodriguez-Ibabe 2007). Al- and Nb-containing steels are particularly prone to the precipitation mechanism, since the precipitates, which typically harden these materials, form around the temperature range that is otherwise most suitable for deformation.

Cooling in continuous casting is significantly more rapid than industrial scale ingot casting (in the region of 1K/s, rather than <1K/s), but this is still slow enough for grains to grow to a fairly large size. The most prominent solidification difficulties with continuous cast grades are centreline segregation, where there is a narrow strip of highly enriched material down the middle, and porosity in the same region due to shrinkage during solidification. Fortunately both of these can be controlled by soft reduction, as mentioned earlier. Continuously cast steels also show a chill, columnar, and equiaxed structure as is found in ingots.

As the cast product is much thicker than the required final product, secondary processing is required, which involves passing the steel through a series of rollers until it is at the desired thickness. When the steel is hot rolled, dislocations are introduced into the matrix, which, given enough stored energy, temperature, and time, can cause recrystallisation to occur. This typically refines the grains and, with many hot deformation passes, the resulting austenitic grain size can be reduced from 1000+ μm to less than 100 μm.

1.3 Direct Casting

Several metals have been commercially cast directly into thin strips for many years now, and the idea of applying these techniques to steels has been around since Henry Bessemer suggested it in the mid-1800s (Ge, Isac and Guthrie 2012). But this approach has proven to pose sufficient technical challenges, meaning it is only this century that several potential methods are approaching and reaching commercial viability for use with steels.

An extreme example of the benefits achievable with direct casting can be seen in the Al industry; the Alcoa Micro Mill has cut the time from molten metal to coiled sheet metal from 20 days to 20 minutes by eliminating the numerous rolling and heating cycles that the conventional approach requires. This obviously also reduces energy usage and can be performed in a smaller plant (Djukanovic 2016). While many steel grades do not require the same heat treatment stages as Al alloys, there are still significant savings in time, effort, and space to be made with more net shape casting approaches for strip production. A benefit of these approaches is that the thin cast sheet allows much higher cooling rates, which in turn produce a finer cast grain structure, however this also limits the secondary processing that is often used to refine grain sizes.

Conventional continuous casting methods produce thick pieces of steel down to approximately 50mm thick, which means a large amount of secondary processing is needed to reach the final sheet metal products, which are typically 1- 2 orders of magnitude thinner. There are a variety of direct casting technologies that have been proposed, most of which are variations of the two main approaches, using either rollers or belts (or both) in varying configurations (single or double,

horizontal or vertical) - *Figure 6* shows a variety of considered options. The two that are most promising, and are therefore the most developed, will be discussed here.

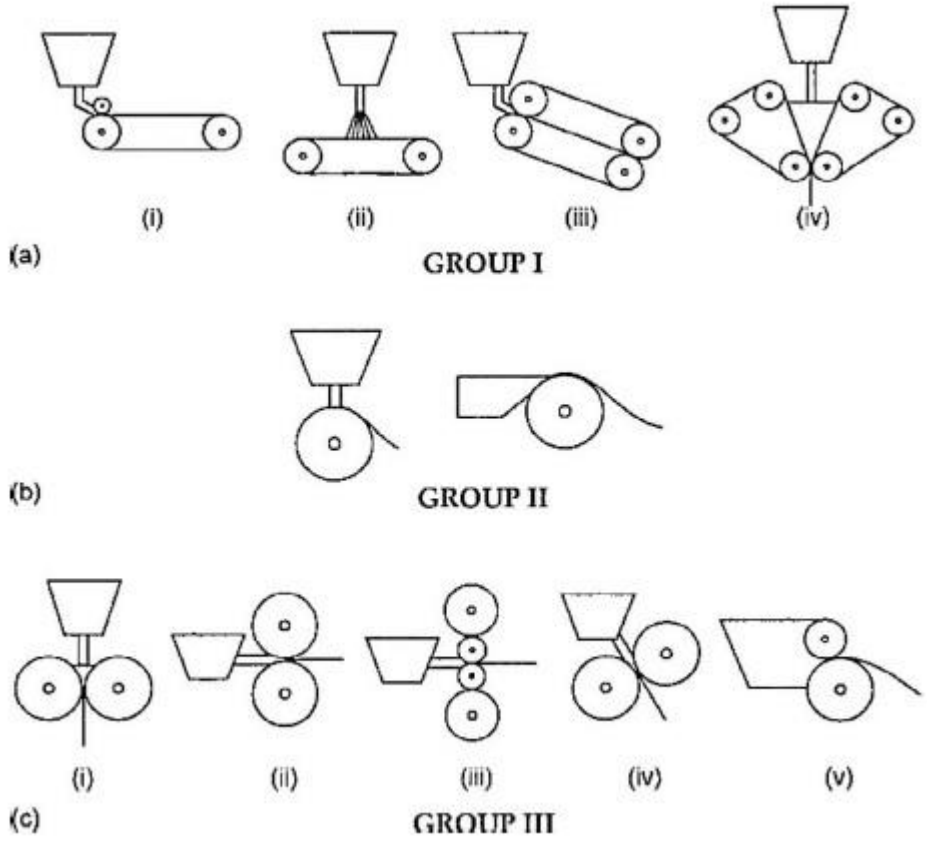

Figure 6 Schematics of various attempted direct casting techniques Group I is belt cast, II is single roller and III twin roller, a1 and c1 are the two currently receiving most attention (Ge et al. 2012)

While research is ongoing, another proposed advantage of these techniques is that direct cast steels can also have a higher tolerance of certain impurities, such as P and Cu (Maleki, Taherizadeh and Hosseini 2017). These elements typically have detrimental effects on mechanical properties even at very low concentrations, and especially when they segregate to grain boundaries or form inclusions (Liu et al. 2007). At least part of this improved tolerance is because the rapid cooling does not allow time for these elements to segregate over large distances or react and form precipitates, instead forcing them to remain in solution. For example, steels produced using the twin roll method can tolerate a greater proportion of P before becoming too brittle to work with, allowing the use of P to increase weathering resistance (Liu et al. 2010) (Zhou et al. 2009). By keeping these elements in the bulk solution there is less need to clean steel feedstock material before casting. This is of particular note for increasing steel recycling, as it simplifies the use of scrap for low demand products by

allowing a greater proportion of scrap to be used with less effort expended to remove the impurities. It is even possible that negating the potential issues with these elements allows exploitation of their beneficial properties, such as corrosion resistance (Liu et al. 2007) or grain refinement.

1.4 Twin Roll

One of the two significant direct casting methods currently being pursued commercially is twin roll casting and it is shown in *Figure 7*. In this process the liquid metal is poured between a pair of internally cooled rollers, where it solidifies on the surface, leaving the two inner surfaces as partially liquid as they are pressed together, before exiting from the bottom of the rollers as a single sheet (Liu, Liu and Wang 2009b). At this point the steel is further cooled and cut, then rolled to the required shapes. This method is not suited to all steel grades or end products, since it is limited to strips of no more than 10 mm thick (Shibuya and Ozawa 1991). Above this thickness solidification is too slow to form a single solid sheet by the time the sheet is leaving the rollers. This then means that production volume is restricted by the rollers. The roller surface must move rapidly in order to achieve high production rates, while any given point needs sufficient time to be cooled before rotating back into contact with the liquid metal. This means high quantity facilities would require prohibitively large rollers (diameter approx. 2.5m (Schwerdtfeger 2001)), meaning twin rolling is likely most suited to producing moderate quantities of specialised steel grades. This process has very high cooling rates, in the range of 10^3K/s, with commercial plants producing in the region of 500KT per year (Ge et al. 2012), and due to how thing the material is, there is no central equiaxed zone. Maintaining a constant strip thickness is a major challenge with this casting method, with a wide range of parameters causing variations in the thickness of the cast. These include obvious things like roller degradation and thermal expansion as well as less obvious influences like the depth of the melt pool, Miyake reported a 7% change in strip thickness from a 4mm change in pool height (Miyake et al. 1991).

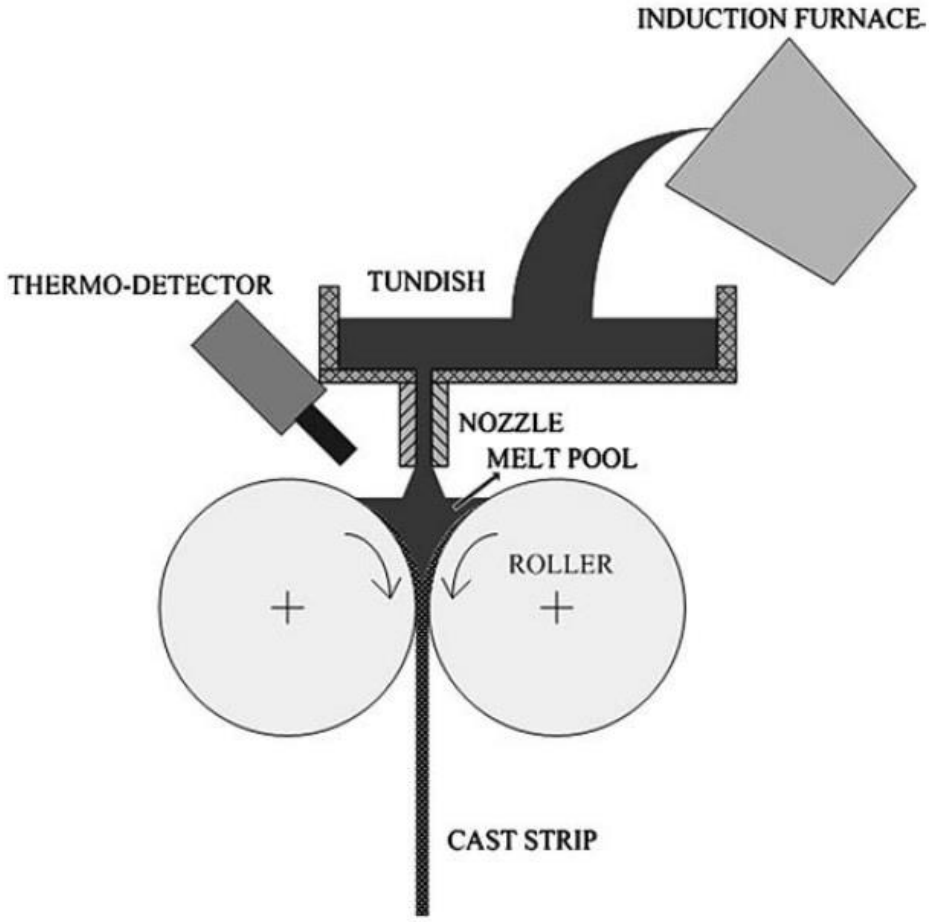

Figure 7 Schematic of twin roll casting (Liu et al. 2009a)

Some defects that are specific to the twin roll process include:

- Surface wrinkles are caused by too low a rolling speed. The proposed mechanism is vibrations in the meniscus propagating down to the solidification region, as higher casting speeds stabilise the meniscus and provide a uniform surface. The minimum necessary speed varies by alloy but values of approximately 0.5 m/s have been reported for several different alloys (Mizoguchi, Miyazawa and Ueshima 1996).
- Triangles, which form when the liquid solidifies on the side dam and is then bent as it passes through the rollers.
- Beads and bleeds, both caused by leakage.
- Edge defects are caused by insufficient sealing between the roller and the side dam.
- Surface cracks are also a significant concern but have many potential causes and often occur alongside other defects. (Yasunaka et al. 1995)

Another issue with twin roll casting is that the two solidification fronts need to meet at the narrowest point between the rollers (called the kissing point). If they meet too early, then liquid is squeezed out, causing negative segregation along the centre (Zhou et al. 2011). However, if they

meet too late, the problems of positive segregation and voids from more conventional casting methods reappear.

Experiments have been performed showing that adding less than 0.1 wt% Ti to low carbon steels can virtually eliminate all surface imperfections when twin rolling particular steel grades (Girgensohn, Buchner and Tacke 2000). So small Ti additions may be a reliable way to improve the quality of at least some twin rolled steels. Some grades such as high carbon steels, which are prone to porosity, tend to need rolling after casting to produce a product with acceptable properties (Schwerdtfeger et al. 2000), and there are also applications where thicker steels are needed. Another concern is deformation of the rolls caused by the extreme thermal and mechanical loads placed on them, which can have an impact on the strip thickness, and thickness uniformity due to the related expansion and contraction (Wechsler 2003).

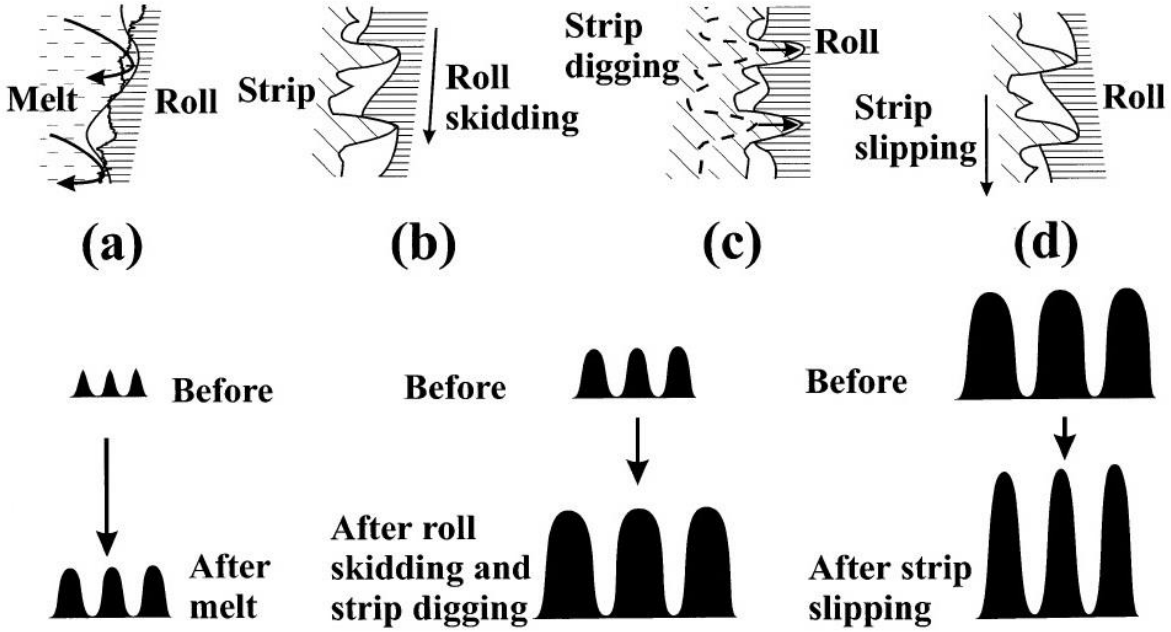

Figure 8 Wear mechanisms on twin roll rollers (Zapuskalov and Vereschagin 2000).

This ties into potential issues relating to the lifetime of the rollers, as conditions during solidification are extreme, leading to degradation of the roller surface through several different mechanisms, which are shown in *Figure 8*. Research suggests that melting of rollers upon initial contact with the melt is the primary mechanism for damage, with several other mechanical processes playing minor roles (Zapuskalov and Vereschagin 2000).

1.5 Single belt

The other method of significance is horizontal single belt casting, shown in *Figure 9*. Like with twin roll casting, this method has shown enough potential to have received a significant amount of research,

(Fischer and Schaperkotter 2010) but also needs further refinement, alongside experimentation, before wide scale adoption, in order to understand the limits of materials that can be produced with it. The first commercial line of this type is by the Salzgitter group in Peine, Germany. In single belt casting, the liquid steel is poured onto a cooled spinning belt. Since the solidifying material moves with the belt, there is no need for mould flux, and the improved thermal contact gives cooling rates in the region of 10^2K/s, and because solidification happens to a horizontal strip, no bending is needed (Wans et al. 2010).

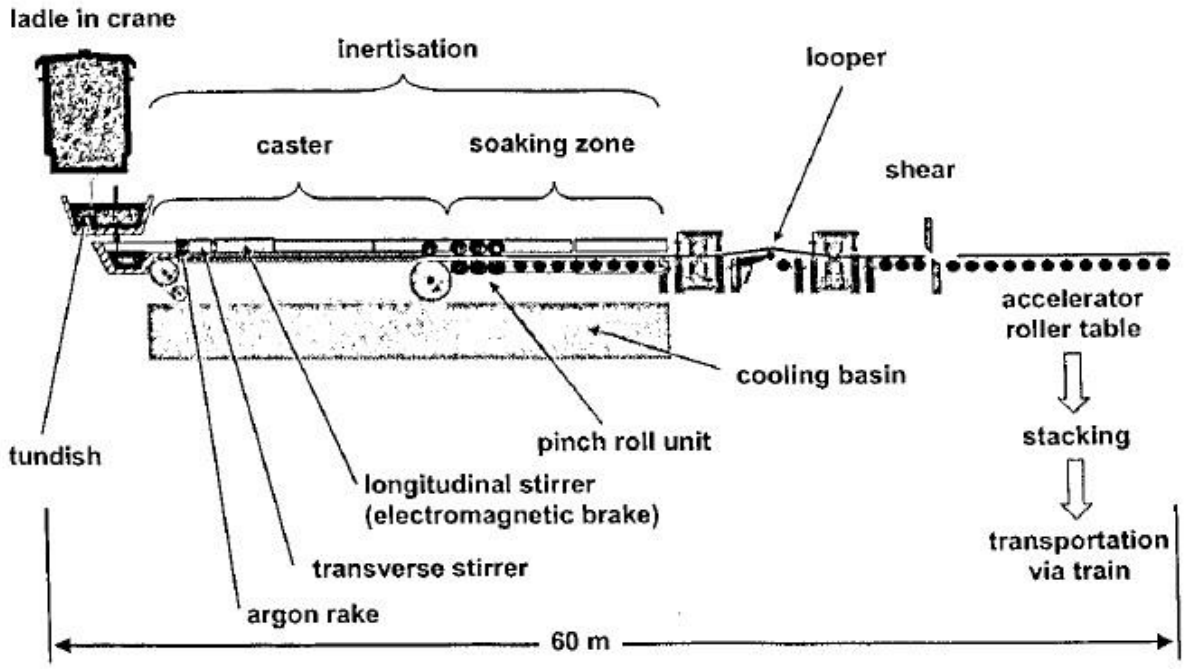

Figure 9 Diagram of single belt casting (Fischer and Schaperkotter 2010)

This lack of bending is a significant advantage for steel grades that are prone to hot cracking, such as high Al steels. Since the steel is already horizontal, there is no need to change its orientation before further processing - this is, again, already drastically reduced due to the cast material already being close to the typical desired thickness of strip products. Another advantage of this process over twin roll casting is that it can be used for relatively thick gauges of steel (reported thickness up to 20 mm). Some steels, particularly those with a high carbon content, require rolling down to about one-quarter of their cast thickness before they have suitable mechanical properties. This is because these grades are porous when they initially solidify, and significant compression is needed to eliminate these pores (Schwerdtfeger 2001). While edge defects are also possible with this technique, the differences in geometry mean they are quite different to the edge defects found in twin rolling systems. If side dams are used, then the solidifying steel may stick or leak down the side where as

methods that do not rely on side dams, such as the use of electromagnetic fields, can result in difficulty maintaining a consistent strip width. Inconsistent cooling, or not casting across the full width of the belt, can also cause the belt to buckle, which will give a highly inconsistent strip thickness.

Another technical issue is that careful control of liquid flowing onto the belt is necessary - not only does the flow volume have to match the intended output volume, but for a smooth end product the velocity of the liquid as it comes into contact should also match the belts velocity as closely as possible. Both a slow-moving thick stream and a fast-moving thin stream inhibit a consistent end product and, on top of this, movement across the belt should also be minimised so that the liquid steel feed should be the same width as the strip that will be produced (Carlsson et al. 1997). Since belt casting typically only actively applies cooling to one side of the product, the microstructure in the finished product will be asymmetrical with the chill zone on the belt face and the enriched final solidifying material at or near the top surface. This has the potential to cause a variation in material properties between the two surfaces (Jacobson, Hollinger and Fredriksson 1993). For example, having final solidification at or near or the top surface means that that face will be solute enriched, with greater potential for porosity and chemical inconsistency, and with larger grains and SDAS compared to the chill zone on the bottom surface. While some tests have shown no significant difference in properties between the top and bottom sections after hot rolling, (Schwerdtfeger 2001) the potential for variation should be kept in mind, particularly when casting new grades using this method. This effect can be reduced by including a small amount of oxygen in the atmosphere, since the oxide layer will radiate heat more readily than untarnished metal (Schwerdtfeger 2001), thereby increasing the top surface cooling rate and moving the position of final solidification closer to the centre. Alternatively, adding a small amount of carbon dioxide to the atmosphere will slightly decarburise the surface, raising its freezing point. In either case, solidification also improves the materials emissivity, reducing the bias in cooling between the top and bottom surfaces (Ge, Isac and Guthrie 2013) so once the top surface solidifies, cooling from the top will increase naturally. Once the surface layer is suitably thick there is also the option to actively cool the top surface using for example argon jets in order to improve symmetry in the cast sheet. Steels produced in this manner may have an equiaxed region, however the asymmetric cooling mean s it will not be central and will be closer to the top surface than the bottom surface.

Another potential consistency issue with belt casting is the development of surface dimples (Guthrie and Isac 2014). These indentations are caused by a local depression in the belt causing weaker local adhesion, the heat then causes the air to expand before the steel can solidify, exerting a force on the liquid and causing a small local indentation, this is shown in *Figure 10*.

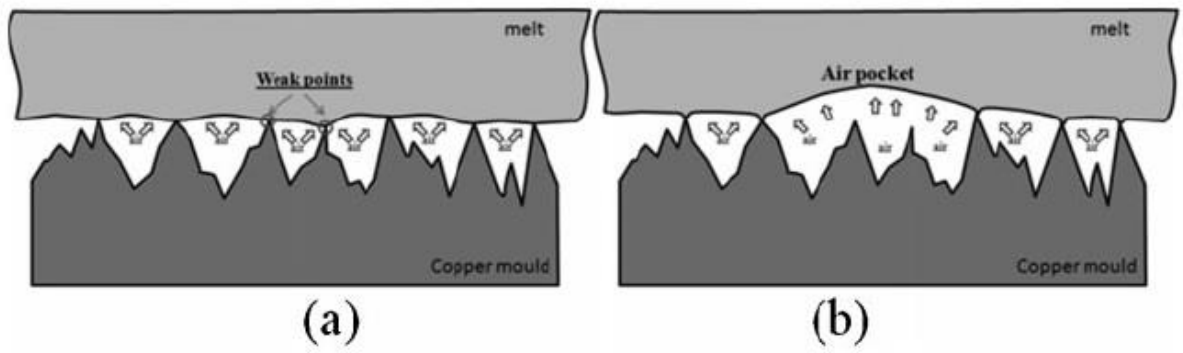

Figure 10 How poor surface contact can cause defects in single belt cast steel, depressed micropeaks adhere less to the surface which is then pushed out as the trapped air expands. (Guthrie and Isac 2014)

1.6 Laboratory Simulations

While full scale casting trials are ultimately an important step in developing materials and techniques, it is more practical to perform early stage work at a smaller laboratory scale. Dip testing involves momentarily dipping a piece of copper into liquid steel, leaving a thin layer of steel on the surface. This layer cools rapidly as the copper acts as a heat sink, and the thin steel layer cannot hold much heat (Strezov and Herbertson 1998) (Mukunthan et al. 2013). This process can be used to provide conditions representative of twin roll casting with high cooling rates observed in the range of 10^3K/s, however variations in cooling rate can be achieved by heating the copper prior to immersion, but control of exact cooling rates is difficult. The CLSM is also a piece of equipment that is valuable for solidification studies and has been used by a small number of groups. Work at Wollongong University using a concentric solidification technique has been developed (Niknafs and Dippenaar 2014). The centre of a disk is melted and then allowed to resolidify from the remaining solid ring, this is possible because the equipment (a confocal laser scanning microscope and radiative heating chamber) allows for very fine control of temperature, the most notable limitations of this equipment are the relatively low maximum cooling rate ≈30K/s and the small sample size ≈5mm. The capacities are discussed further in the methodology section.

1.7 Comparisons

With an understanding of conventional techniques and both of the most promising direct casting techniques, as well as their technical demands, it is now possible to discuss the similarities and relative strengths and weaknesses of the various approaches.

Since all direct casting methods have many similarities, there are a variety of product defects shared by many or all of them. However, some defects are specific to particular techniques. Since near net shape processes produce much thinner casts and do not require the use of a mould flux, they open

the possibility of producing steel grades that are impractical to produce in bulk with conventional techniques, whether due to cracking during processing or reactions with the mould flux. An example is high Al steels, as these tend to have a large grain size, which will be minimised by the rapid cooling, and are very prone to cracking, which is mitigated by approaches that reduce deformation stresses - the high Al content also reacts with many mould fluxes.

Both single belt and twin roll techniques require much less secondary processing than conventional techniques (Sosinsky et al. 2008) (Daamen et al. 2014), which is the main source of the improved energy efficiencies seen in these production methods. With twin roll producing the thinnest cast material it is likely that the efficiency gains seen from it (such as those for the Castrip process seen in *Table 1*), are greater than those from single belt casting, but both promise vast improvements in energy usage. The reduced size of the casting equipment and limited secondary processing also open up the possibility of rolling to the final thickness in-line in one operation, further improving efficiency gains (Ge et al. 2013).

Table 1 Energy saving in the CASTRIP twin roll process compared to conventional continuous casting methods (Mahapatra et al. 2008)

	Energy consumed GJ/t	GGE* t CO_2 equiv/t
Thick slab caster + hot strip mill	1.8	0.2
Thin slab caster + hot strip mill	1.08	0.14
Castrip process	0.2	0.04
Savings – Castrip vs. thick slab	89 %	80 %
Savings – Castrip vs. thin slab	81 %	71 %

* Greenhouse Gas Equivalent or t of CO_2 equivalent per t of steel produced

However, there are trade-offs - improving efficiency by casting thinner material requires faster casting speeds in order to maintain economically viable production rates. Single belt has an advantage over twin roll in this regard, since the casting is several times thicker the cast sheet (and casting surface) can move slower for the same volume of output - this is true even after accounting for twin roll having two heat extraction surfaces.

Another issue related to the thinness of the cast material is the much larger surface area to volume ratio. If the atmosphere around the cast was the same as the general atmosphere, then this would lead to losing an unacceptably large proportion of material to oxidation and a large amount of nitrogen uptake, as well as the associated development of nitrides, both of which can compromise

the materials properties. This makes it necessary to perform casting in an inert atmosphere. Typically, a positive pressure argon atmosphere is used since argon is the most readily available gas that remains sufficiently inert even in the region of 1850K, and the higher pressure inside the controlled area means argon will leak out rather than atmospheric gasses leaking in.

In many direct casting methods there is no need for mould lubrication, so the liquid is in direct contact with the mould (belt or rollers). Combined with the material traveling with the mould, this greatly improves contact between the mould and cooling steel. The reduction of thermal mass compared with conventional casting, due to the thickness of steel, means that the cooling of the bulk material in direct casting occurs several orders of magnitude faster than in conventional continuous casting (Sosinsky et al. 2008) (Campbell et al. 2004) (Daamen et al. 2014) (Gao et al. 2009). While this means a much finer (so theoretical superior) initial grain structure, conventionally cast steels gain a lot of their structural properties during secondary processing which is absent or drastically reduced. Some steels, such as high carbon steels, even require a degree of hot rolling to develop a suitable microstructure - for these grades it is to remove porosity, and as such the steels must be cast several times thicker than the end product to allow for the minimum necessary secondary processing (Daamen et al. 2014) (Schwerdtfeger 2001).

Other grades that are difficult to conventionally continuous cast and therefore of particular interest for near net shape casting are peritectic grades, as these grades are especially prone to uneven solidification behaviours and cracking when cast using conventional casting techniques, requiring a slowdown in production rate in order to produce an acceptable product (Emi and Fredriksson 2005). The issues with peritectic grades are primarily a matter of local inhomogeneities - due to the nature of the peritectic point, the slight variations in segregation/back diffusion/cooling rate, and other factors, can change the solidification path for adjacent regions. This can lead to differences in local behaviour, such as differing contraction rates, which can for example reduce mould contact, inhibiting heat extraction and creating local hotspots that, whether remelted or merely a higher temperature solid, will be weaker and more prone to cracking or void development. This is especially important due to the high stresses created by bending seen in conventional continuous casting (Moon 2015). This variable contraction also poses an issue for soft reduction, since the degree of rolling needed becomes variable. Therefore, the production of these grades also stands to benefit from the use of direct casting techniques, since they eliminate or mitigate many of the issues specific to these grades.

1.8 Casting Summary

A wide variety of thin strip casting methods have been proposed, many of which are slight variations on one of the systems already discussed in detail, and have seen interest diminish as companies focus on the more promising variants, namely twin roll and single belt (Nystrom, Reichelt and Dubke 2000). Both horizontal single belt and twin roll casting offer a variety of economic benefits in reduced start-up costs, needing less space, and a dramatic reduction in the energy required to produce the end products. They also theoretically offer the potential to produce various steel grades that are difficult or impossible to commercialise when using more conventional casting techniques. The higher cooling rates will refine both grain and dendrite sizes, while the geometry will reduce or eliminate the stresses responsible for hot cracking, and the elimination of mould fluxes prevents issues with the steel reacting with fluxes. The high cooling rates may permit greater tolerance of certain tramp elements that are all but universally detrimental using conventional casting techniques.

These advantages make them tempting processes for thin gauge steel products despite the technical challenges they pose, such as the increased need for precision and maintaining an inert atmosphere. While twin roll has been successfully used for thicknesses of up to 10mm, the economically viable upper limit seems closer to 2.5mm (Wechsler 2003). Although strips a fraction of a mm thick have been produced, the rolling speed necessary for an economically viable production rate are currently prohibiting producing such thin material. For finished products below about 1.3mm some degree of rolling after casting is still the most viable production method (Wechsler 2003). In comparison, belt casting is suitable for casting thicknesses in the range of 5-15mm (Carlsson et al. 1997). Researchers focusing on each twin roll and single belt casting, unsurprisingly, consider their chosen technique to be the most promising, and it seems likely that each will have their place. Twin rolling with its extreme cooling rate and very thin cast material but somewhat restricted output volume in producing particularly thin gauge steels, which are likely to be somewhat more specialised and needed in smaller quantities. While single belt produces bulk grades, as well as grades with similar requirements to carbon steels, which suffer from porosity and need to be cast thicker in order to produce the necessary microstructure in secondary processing.

Of the research groups and commercial facilities around the world who are making use of, and refining, direct casting techniques. Some of the most prominent include the Nucor CASTRIP plant in the USA, which uses the twin rolling process to produce low carbon steel that is 1.5-2mm thick and up to 2m wide with an output in the order of 0.5Mt/year (Sosinsky et al. 2008). The MEFOS facility in Sweden, working on single belt casting, with an industrial scale machine in use (Wans et al. 2010). There is another belt casting facility in Salzgitter run by the Salzgitter group, allowing them to

provide a variety of grades, primarily to the automotive sector. There is also a research focused belt caster at McGill university in Canada that studies many metals including steels. For clarity, *Table 2* summarises many of the significant differences between various casting techniques.

Table 2 Summary of differences between casting techniques

	Conventional Thick Slab	Conventional Thin Slab	Single Belt Casting	Twin Roll Casting
Thickness (mm)	200+	50+	15-30	1-3
Approx. Cooling Rate (K/s)	1	5	100	1000
Approx. Energy per tonne (GJ) (scrap feed)	2	2	0.5	0.2
Bending Stress	Yes	Yes	No	No
Mould Flux	Yes	Yes	No	No
Significant material loss in standard atmosphere	No	No	Yes	Yes
Length to a finished product (m)	300-800	200-400	60-100	60-100

This work comes out of these advances in casting techniques because they allow for the production of steels containing a large amount of aluminium cheaply enough for them to be commercially viable, and casting at near net shape increases the reliance on cast structure, especially in these steels which are single phase. This greater dependence on the cast structure pushes the need to understand it in even greater detail, and to better make predictions of new grades before going through the expense of analysing physical samples.

An obvious concern relevant to all direct casting techniques is the relatively limited study of steels at such high cooling rates, leading to uncertainty about the structures that will develop, and the properties of the material. This means each grade needs to be carefully and extensively tested under these new manufacturing conditions before being commercialised, or at least in a sufficiently wide variety of alloys so that the others can be modelled reliably. Direct casting may therefore not be an appropriate solution for all steel grades if the high cooling rates lead to detrimental effects.

Section 2 – The Solidification Process

Section 2 will cover the fundamental science influencing the solidification structures found in steel products. This will start with a discussion of how solidification occurs and the structures that develop, before moving on to how changes in solidification parameters influence the size scale and development of these structures, as well as briefly looking at how solid state phase transformations can further modify the structure. Particular attention will be paid to steel compositions that are relevant to the research carried out, i.e. high Al steels.

2.1 Phases in Steels

At its most basic level, solidification is when the free moving atoms and/or molecules in a liquid lose enough kinetic energy that the various attractive forces between them can overcome the kinetic energy, meaning the particles become locked in place. For most pure materials, as well as many mixtures, including metallic alloys, this means the atoms settle into regular arrays called crystals. Steels show a variety of crystal structures, which depend on both the materials composition and the processing techniques involved, in particular the cooling rate used. The addition of other elements has a wide variety of effects on the mechanical and chemical properties of the steel. While many steel grades need a significant proportion of the relevant alloying element to be effective, such as Cr and Ni in stainless grades, some steels show the necessary change in properties even at very low alloy concentrations, allowing the production of micro-alloyed steels.

Phase diagrams, like those shown in *Figure 11* and *Figure 12*, serve as a graphical representation of the solidification behaviour of a material. Typically, the Y axis is temperature and the X axis shows the variation in the proportion of a single constituent element (added to the matrix), with lines then showing the boundaries between different phases. While some regions of the graph contain a single phase, many show multiple phases existing simultaneously. The difference between *Figure 11*, the standard Fe-C phase diagram, and *Figure 12*, an Fe-C phase diagram when the material also contains 7% aluminium, demonstrates how additional alloying elements change the phase diagram. By changing the thermodynamics of the system, the boundaries between phases change location, with the possibility of also creating additional phases and/or removing other phases entirely. While these models do tend to produce representative results for grades with relatively standard compositions, their accuracy tends to be lower for more novel compositions, due to a lack of empirical data correcting the calculations based on theory alone (Presoly, Pierer and Bernhard 2012).

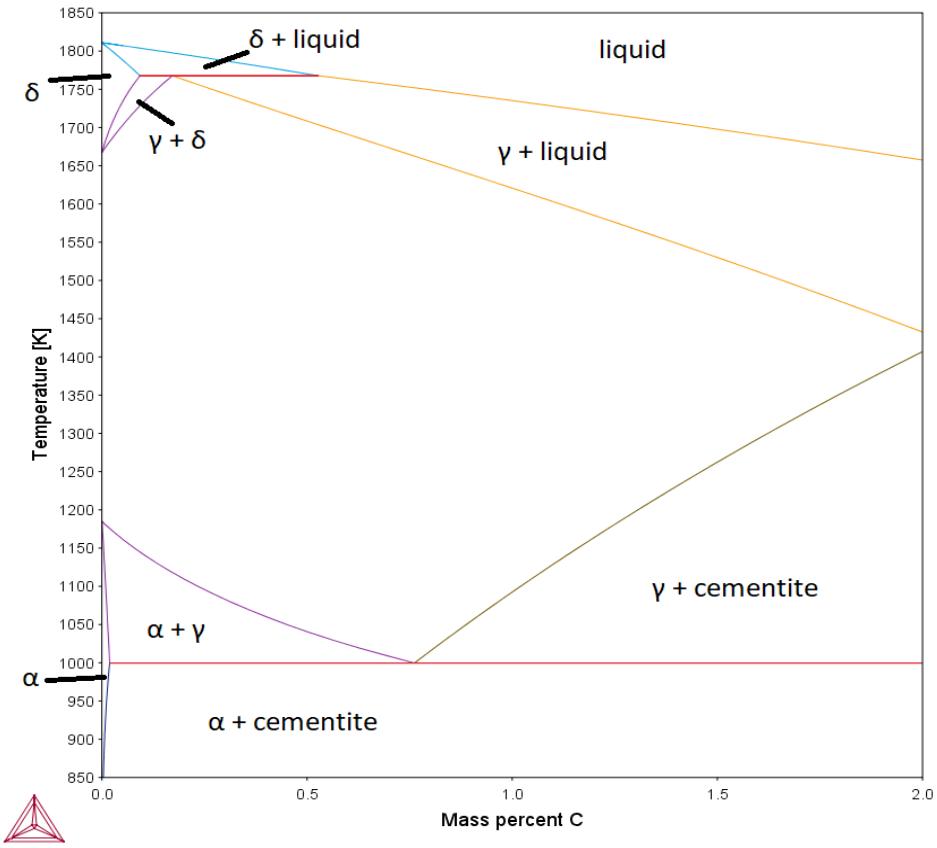

Figure 11 The Fe-C phase diagram, with phases labelled.

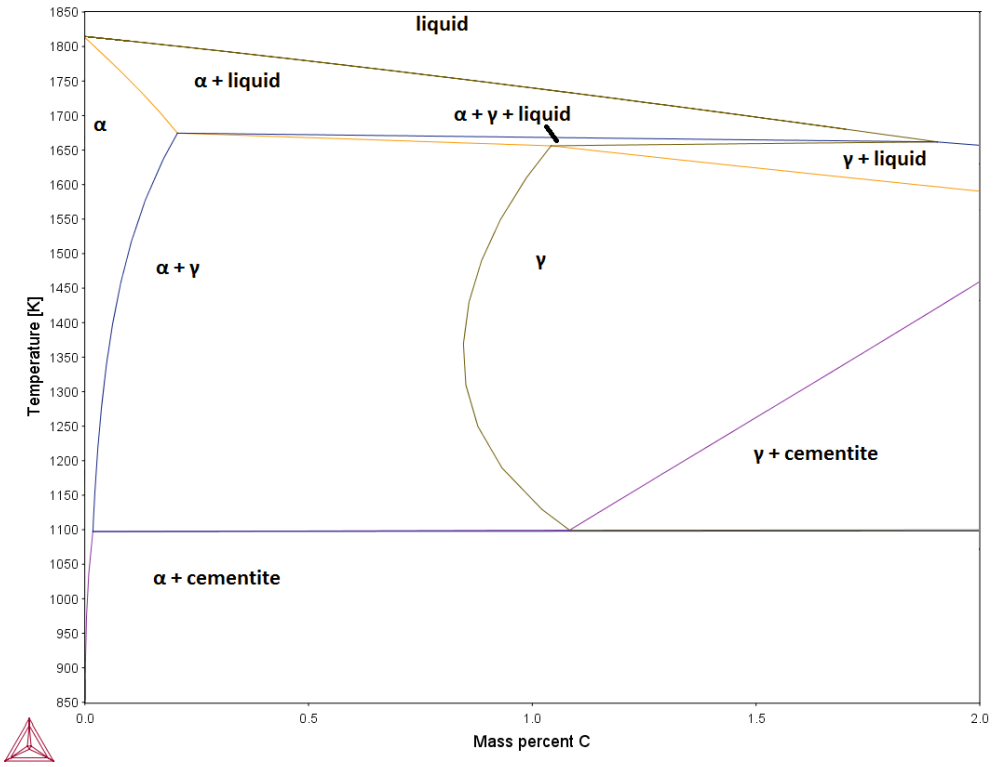

Figure 12 The Fe-C diagram for steel containing 7% Al, showing similar trends but clear differences from the Fe-C diagram above.

Most alloying elements in steels are known to be either austenite or ferrite stabilisers, depending on which region of the phase diagram they enlarge. The relative effectiveness (per wt%) of many common steel alloying elements as either ferrite or austenite stabilisers is shown in Figure 13. Each element also typically segregates into the stabilised phase if multiple solid phases are present. For example, if a steel grade is held at a high enough temperature to permit diffusion and contains both ferrite and austenite, then Ti and Al will diffuse into the ferritic regions and Mn and Ni will diffuse into the austenitic regions, potentially leading to large composition differences in dual phase steels that spend a prolonged time at elevated temperatures (Honeycombe and Bhadeshia 1995).

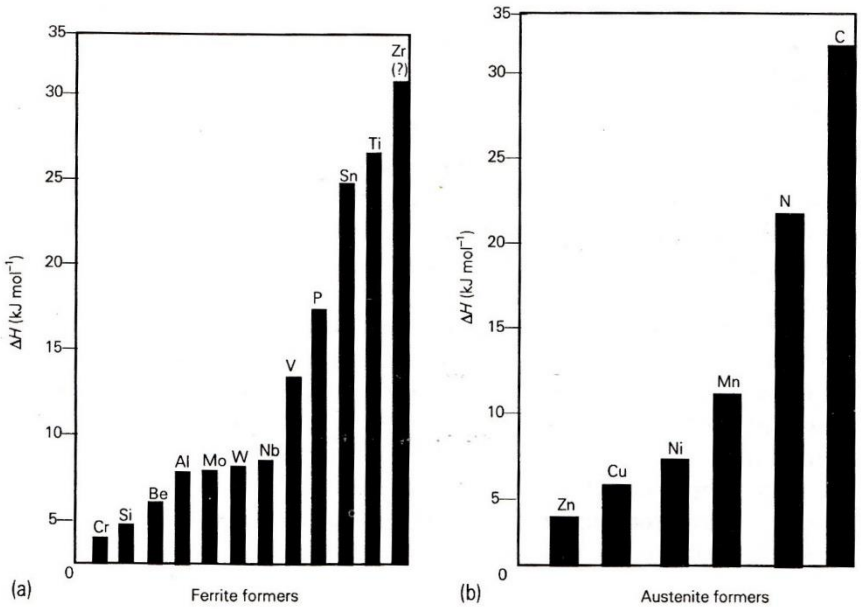

Figure 13 Relative effectiveness of a fixed weight percentage of common steel alloying elements as ferrite or austenite stabilisers (Honeycombe and Bhadeshia 1995)

Unsurprisingly, the fraction of each phase changes smoothly through these mixed regions - for example, just below the liquidus line, the material is almost entirely liquid and just above the solidus line, almost completely solid.

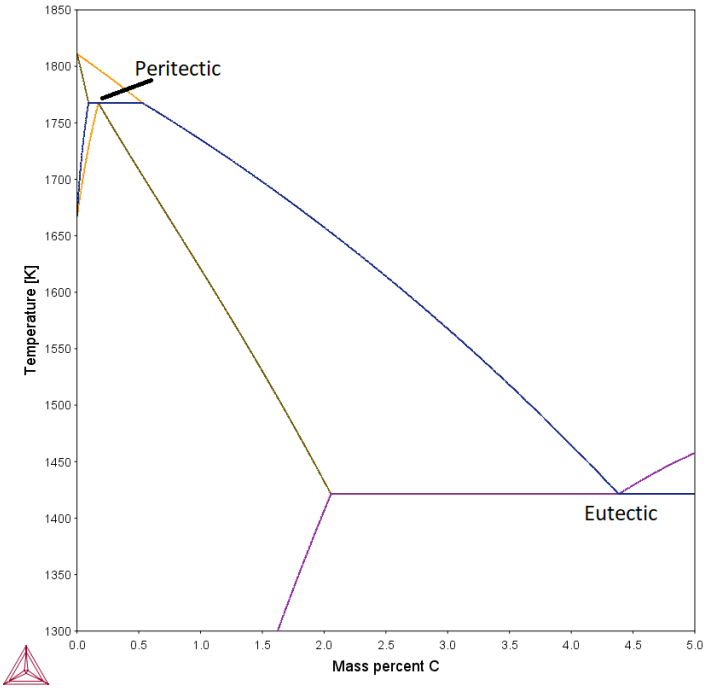

Figure 14 The peritectic and eutectic points on the Fe-C phase diagram.

In general, this smooth change of phase fractions causes solidification sequences to show a simple pattern of one phase gradually transitioning to the next. However, at several points where multiple phases meet, there are more complex events, examples of which are noted in *Figure 14*. There is the eutectic point, a composition where there is a local minimum in the liquidus temperature and solidification will occur completely at that minima. Immediately below this point two solid phases exist, but just above the solution will be entirely liquid. From this point immediately above the eutectic, a slight change either way in the percentage of alloying element (C in the Fe-C diagram) leads to one or the other solid phases coexisting with the liquid. In contrast to the normal alloy behaviour of solidifying over a range of temperatures with the composition of the liquid changing throughout the process, eutectic solidification occurs by definition at a fixed composition and also at a fixed temperature (Guy and Hren 1974).

There are also peritectic points, where a liquid and one solid phase react as they cool to produce a single, different, solid phase. In theory, the remaining liquid will diffuse through and react with the first solid phase, giving a material that is uniformly composed of the second solid phase, but this process is extremely slow and tends not to be complete in practical settings, leading to structures with grains of the initial solid phase embedded in the second solid phase (Fultz 2014).

2.2 Nucleation

While the experimental sections of this work focus on columnar growth (i.e. the stages subsequent to nucleation), nucleation is still an important place to start in an overall understanding of

solidification. There are two main categories of nucleation, heterogeneous and homogeneous. A sample of extremely clean material that is not being agitated can undergo homogeneous nucleation, while in the majority of real world situations some degree of inhomogeneity acts as nucleation sites to trigger heterogeneous nucleation at specific points, with much less undercooling than is needed for homogeneous nucleation. Undercooling is the extent to which the temperature of the liquid is below the melting/liquidus temperature for that material, thus it is how far the liquid has been cooled below where the solid phase would be (more) stable if it was present (Zettlemoyer 1969). The reason for these two different types of solidification lies in the thermodynamics of phase changes - the phase change itself is driven by the newly developing phase having a lower energy than the previously existing phase under current conditions, but the existence of a boundary between the two phases imposes an energy cost. The random motion of atoms (or molecules) in a liquid constantly produces countless small clumps of particles, which are only stable if 1) local conditions make the solid phase energetically favourable and 2) the energy released by the new crystal exceeds the energy cost of the new boundary. The energy reduction of the new phase is proportional to the volume (proportional to r^3), but the energy cost of the boundary is proportional to the surface area (proportional to r^2). This means that very small crystals that form as statistical noise will have a greater energy cost imposed by the surface than is released by the volume, and will tend to melt back into the liquid, but over a critical size these random crystals will be stable and grow, acting as nucleation sites. The equation governing this process is

$$\Delta G = \frac{4}{3}\pi r^3 \Delta G_V + 4\pi r^2 \sigma \qquad \textit{Eqn 1}$$

Where $\frac{4}{3}\pi r^3$ and $4\pi r^2$ are the volume and surface area of a sphere with r being the radius, ΔG_V the change in Gibbs energy per unit volume and σ the surface energy per unit area of interface. This equation assumes a spherical nucleus, but since a sphere maximises volume for a given surface area, spherical nuclei are stable smaller than any other shape making this a reasonable assumption (Fultz 2014). Above the melting point of the material ΔG_V is positive and the line plotted will blow up indefinitely, but below this temperature the term is negative so the line will initially have a positive gradient while the r^2 term dominates, followed by a peak then have a negative gradient once the r^3 term dominates, beyond this peak an increase in size makes the nucleus more stable and it will tend to grow, as shown in *Figure 15*.

The size of this critical radius is

$$r^* = \frac{2\sigma V_m}{-\Delta G^{Ls}} \qquad \textit{Eqn 2}$$

Where V_m is the molar volume and ΔG^{Ls} is the driving force for solidification (the difference in Gibbs energy between the solid and liquid phases)(Fredriksson 2012)

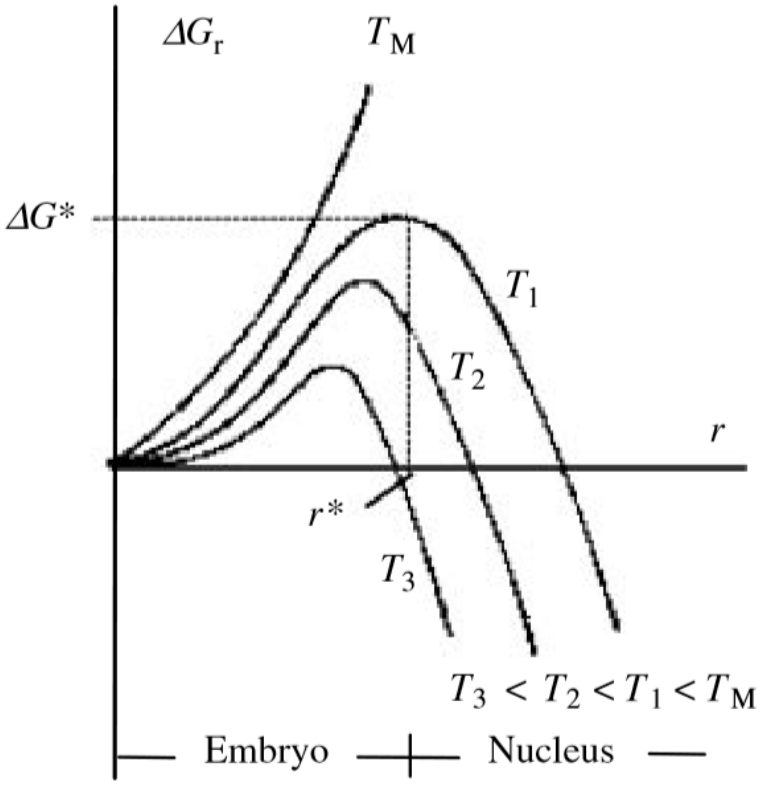

Figure 15 Change in energy for a nucleus varying with both nucleus size and temperature of the system, taken from (Fredriksson 2012)

The difference in energy of the different phases is temperature dependant. The energy gap between solid and liquid is much more pronounced far from the freezing/melting point, this means that very high undercooling produces a large difference in energies between the two phases, and only a relatively small collection of atoms is needed to save enough energy to overpower the boundary formation cost. The reduced kinetic energy also extends the lifetime of the small clusters that develop by reducing the speed of individual particles, increasing the chance of a cluster of a given size developing. With enough undercooling, nucleation will occur simultaneously at a vast number of points throughout the entirety of the material, and the grains grow with an equiaxed dendritic morphology (growth morphologies are discussed in following sections), this is known as homogeneous nucleation (Wasserman 2012).

Since lower undercooling gives a less pronounced energy difference between states, the random movement of atoms in the bulk liquid has a statistically insignificant chance of producing a large enough cluster to become stable. With an arbitrarily long period of time nucleation would still occur, but for practical purposes this inhibits nucleation in real world environments, requiring other factors to come into play to assist in triggering nucleation. This is often contact with the container or an inoculant particle. Atomic scale interactions between a liquid and a solid determine the wettability

of the solid by the liquid, this can be easily understood in terms of its effect on the contact angle formed by a small droplet of the material on a surface. If the pair have low wettability then there is a high contact angle and the droplet forms a near complete sphere, with a high wettability the same volume of liquid forms a much shallower and wider spherical cap (Butt, Graf and Kappl 2006). When nucleating on the surface, only the portion of the sphere produced by the wetting is required to produce a stable grain, thus a highly wettable surface makes it much easier for this smaller number of atoms to randomly group and become stable, as shown in *Figure 16*.

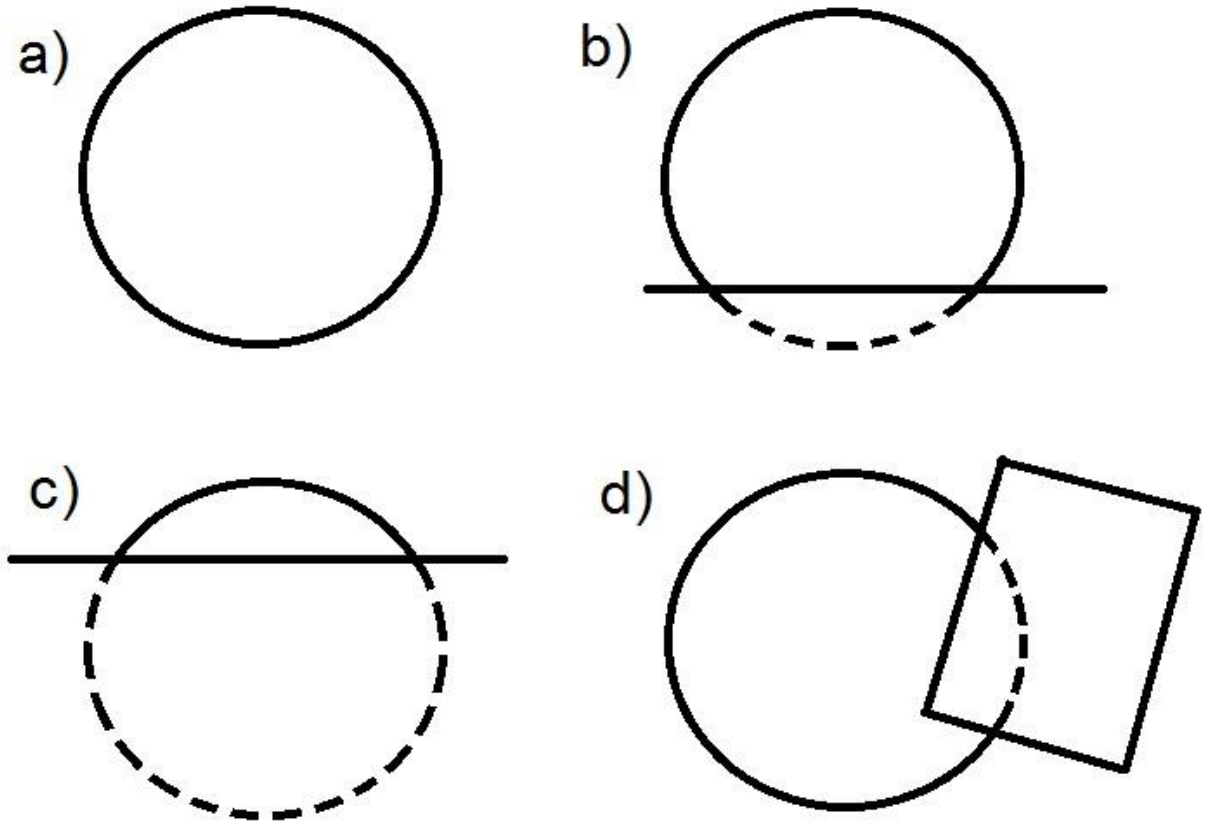

Figure 16 Schematic of the minimum stable grain size a), and how it varies with both low wettability b) and high wettability c) surfaces as well as a small inoculant particle d) (the situation for a large particle is virtually identical to a surface).

Inoculation is a method of refining grain size by inducing the same phenomena throughout a material, which also reduces the required undercooling (Wannasin et al. 2013), but does have limitations, especially when applied to steels. Obviously the particles must be well mixed in order to produce a uniform structure, but at the temperatures of liquid steel, few materials will remain as small particles for long, and also only between 1% (Greer et al. 2003) and 4% (StJohn et al. 2011) of particles typically trigger nucleation events, making it fundamentally inefficient. Generally speaking, finer particles are preferred, as they are less harmful to the material's mechanical properties (Kurz and Fisher 2005). This dependence on wettability and microscopic scale topology highlights the potential for changes in surface material, roughness, and coating to influence the nucleation

behaviour of a material. Section 2.10, focusing on the effect of changing parameters expands further on some of the ideas in this section.

2.3 Chill zone

As mentioned in Chapter 1, the dominant solidification morphology changes with depth from the surface of a casting. The surface is dominated by nucleation and shows a thin layer of small grains with random orientations. Work by (Mapelli and Baragiola 2008) showed the chill zone of a 160*160 continuous cast resulphised billet containing 0.075%C and 1.24%Mn, with small amounts of other elements to extend in the range of 4-11mm from the surface. However detailed chill zone analysis is generally quite sparse in the literature due to a number of factors that make it challenging. Examples of this are the curving of sample edges that develop during polishing, oxidation during casting, oscillation marks and other surface defects or simply phase transitions obscuring the cast structure throughout the material. Since the scale of structure in the chill zone is determined by the amount of nucleation that occurs, factors such as cooling rate and composition that influence nucleation behaviour will affect the extent of the chill zone and the size of the grains it contains (Boultbee and Schofield 1981).

2.4 Dendritic Growth

Due to the composition and thermal gradients involved, steels, along with many metallic systems predominantly solidify as dendrites, and while these finer structures are not too important for understanding equiaxed grain growth, they are important for understanding the growth in the columnar zone, in particular direction growth and columnar grain competition.

When the temperature is only slightly below the solidification temperature (low undercooling), then the solidification front will be smooth, but as undercooling is increased (the liquid is cooled further below its solidification temperature) the interface becomes unstable. It is useful to initially consider a pure material again, with low undercooling there will only be a small thermal gradient from the solid-liquid interface into the liquid. This means that any random fluctuations growing into the liquid ahead of the bulk of the interface will be surrounded by liquid at or above the melting point. With less neighbouring atoms to stabilise the structure, growth of the protrusions will stall, or even remelt back to the rest of the surface, thus allowing the interface to remain planar. When the undercooling is large enough to trigger homogeneous nucleation, grains nucleate out in the bulk of the liquid, away from any interface. The liquid can initially be considered thermally and chemically homogeneous, so in this situation the latent heat of fusion heats the surface of the grains, making a negative thermal gradient where the liquid is cooler than the grain. Since the liquid surrounding

protrusions has less recently solidified material near it, liquid near the tips is heated less by the release of energy than liquid mostly surrounded by solid, this allows any instability that develops to continue to grow, creating an equiaxed grain with a dendritic structure (Porter, Easterling and Sherif 2009).

In an alloy there are compositional gradients as well as thermal gradients, resulting in two additional growth geometries, each of which is essentially a modified planar front with a larger surface area - a qualitative comparison of when these different geometries occur is shown in *Figure 17*. As undercooling is pushed higher from the planar growth condition, the variation in both temperature and composition means that the instabilities in the planar front effectively experience a negative gradient much like in the equiaxed grains discussed previously. But at an undercooling insufficient to cause homogeneous nucleation, this means that solidification must progress from nucleation sites such as inoculants or (more typically) the container surface. This leads to a cellular structure, with the front progressing as a series of domes. As undercooling is increased further these domes become narrower and more elongated, and eventually liquid is present down a significant length of the solidified material, and instabilities in the side can follow the same process of growing through a negative gradient, producing a branching dendritic structure. Since both temperature and composition gradients are involved in the change from planar to cellular and dendritic morphologies, both of these factors also impact the scale of dendritic structures that do form (Stefanescu 2002).

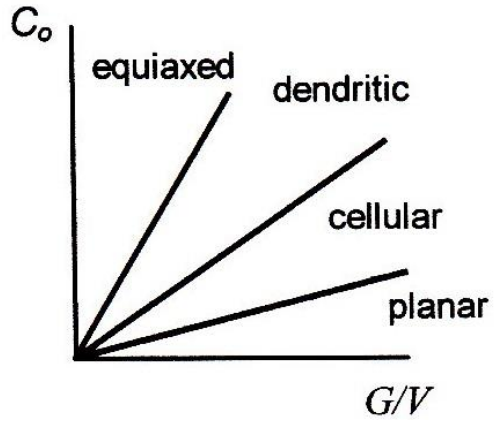

Figure 17 Dependence of solidification front geometry on the Gibbs free energy (G) and solidification velocity (V) varying with composition (C_0) (Stefanescu 2002)

The primary dendrites are the main trunks that grow in roughly the direction of the temperature gradient and the secondary dendrites branch off these structures. This leads to three commonly used quantities in characterising dendritic structures, the primary dendrite spacing and secondary

dendrite arm spacing are the distance between primary and secondary arms respectively, and the tip radius is the radius of the primary dendrite tip, these are shown in Figure 18. These dendrites branch at specific preferred orientations, determined by the crystal structure of the solidifying material (e.g. right angles for materials such as steels, which have a cubic structure). The spacing between both the primary dendrites themselves and the secondary or higher order arms is determined by what is most energetically favourable, and this depends on the composition (Spinelli et al. 2004) (Volkova, Heller and Janke 2003), cooling rate and thermal gradient. Initially (near the tip), dendrite arms grow very closely together (low spacing) but then as the tip moves on and the arms are in a liquid, where the proportion of alloying elements is gradually rising, the thermodynamics of the system change, and the largest arms continue to grow while the smallest melt back into the liquid. This re-melting is caused by a conflict between different driving forces. The thermal and compositional gradients encourage growth of the extremities while impeding growth near the bulk of the solid, initially leading to a dendritic structure. But then the energy of the interface is minimised by minimising the surface area, so re-melting begins with the smallest protrusions vanishing until with enough time a planar interface would be restored, so a solid dendrite in a liquid is an inherently unstable structure. The primary dendrite spacing tends to be most responsive to conditions early in solidification, and then only slowly responds to changes in conditions by the trunks bending to increase/decrease average spacing. Either with some trunks being eliminated, or tertiary branches filling larger gaps, while secondary dendrites form later in solidification and are small enough for specific branches to fully re-melt, making them more representative of conditions later in solidification (Fredriksson and Stjerndahl 1982).

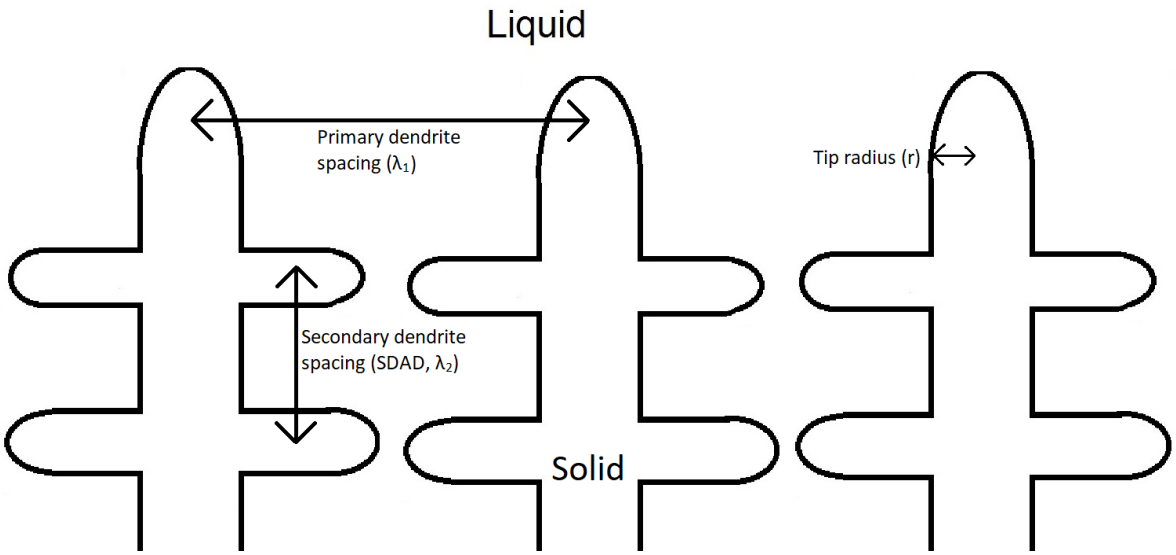

Figure 18 Common characteristic properties of dendrites

At low growth rates the stability of the dendritic structure is determined by

$$\sigma = \frac{2Dd_0}{R^2V} \qquad \textit{Eqn 3}$$

Where D is the diffusivity, d_0 is the capillary length, both of which can be either thermally or chemically controlled, R is the tip radius and V the growth velocity however this breaks down at higher cooling rates where kinetic effects become more important (Asta et al. 2009).
Several coarsening mechanisms have been proposed and are shown schematically in *Figure 19*. First, arms that are narrower along their entire length melt in a uniform manner along their entire length. Second, dendrites with a narrower base melt at the base first leaving a free floating crystal that can either fully re-melt or be carried off and act as a nucleation site elsewhere (Wang et al. 2010). And third, a more pointed dendrite can melt from the tip back down to the root.

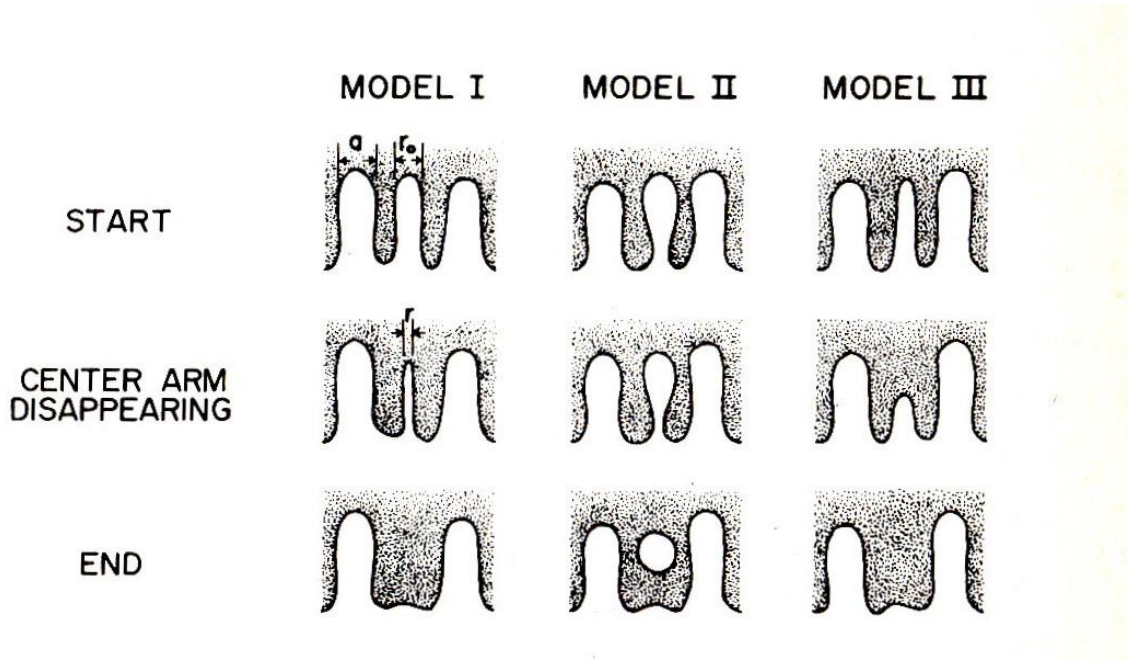

Figure 19 Mechenisms of dendrite coursening (Flemings 1974)

As solidification progresses the changing conditions can cause the most stable dendrite spacing to decrease, if this occurs then the dendrites will start to grow together and where larger gaps open up tertiary arms (with the same orientation as the primary dendrites) will rapidly grow and catch up to the solidification front, filling the gap. Likewise, if the new conditions favour a wider spacing, then dendrites that are already tightly packed will be crowded out, slow down, and be overgrown and the

remaining dendrites rearrange until the spacing between them is approximately equal (Wang et al. 2012b) (Tourret and Karma 2015).

Ideally a dendrite will grow completely perpendicular to the thermal gradient, however grain nucleation is essentially random, so grains nucleate at other orientations and there is competition between growth in the preferred crystallographic direction and growth directly along the thermal gradient (Wang, Wang and Li 2012a).

The general idea is that when there is a large deviation between the grain orientation and the thermal gradient, then a significant component of the dendrites growth velocity is perpendicular to the thermal gradient, the rate of growth parallel to the thermal gradient with be the growth based on the driving force multiplied by the cosine of the misorientation angle. As the misaligned grain lags behind the solidification front the increasing undercooling accelerates the dendrite until the component of its growth velocity that is parallel to the thermal gradient matches the growth rate of the more well aligned grains. This means that while poorly aligned grains initially lag behind better aligned grains, their growth rate accelerates as they fall further behind the solidification front and eventually reach a steady state where they grow at the same rate as the solidification front. Mathematically that is

$$\Delta G_1 \theta_1 = \Delta G_2 \theta_2 \qquad \text{Eqn 4}$$

Where the subscripts denote the different grains.

Dendrites with a low deviation will grow more readily at lower undercoolings, potentially to the extent that their secondary arms expand out and cut off the less well aligned grains, out-competing them and extending deep into the material, while the poorly aligned grains are eliminated. At lower growth velocities the energetically favourable crystal orientation dominates growth direction, but at higher velocities the thermal gradient dominates, suggesting that grains are eliminated over shorter distances with lower cooling rates. At low thermal gradients the atoms will attach exactly along the thermal gradient, but as the thermal gradient increases, the direction of growth shifts towards that dendrite's crystallographic orientation (Wang, Li and Wang 2011). This happens because the crystal structure more readily accepts atoms along a specific axis, and at low undercooling growth is slow enough that even orientations far from the thermal gradient can grow and keep pace with the shifting solidification front. But at higher thermal gradients, unfavourable crystallographic orientations cannot acquire atoms fast enough to keep pace with crystallographic growth directions, so growth is primarily along these crystallographically favourable axes (Tilley 2007). This also explains why grains that are crystallographically aligned with the thermal gradient can grow ahead of misaligned grains and ultimately outcompete them. In cubic structures, the preferred orientations are the <1,0,0> family. Each parallel group of dendrites is a single grain and so the varying growth

directions and velocities explain the competition between differently orientated grains seen in columnar growth regions (Suwas and Ray 2014).

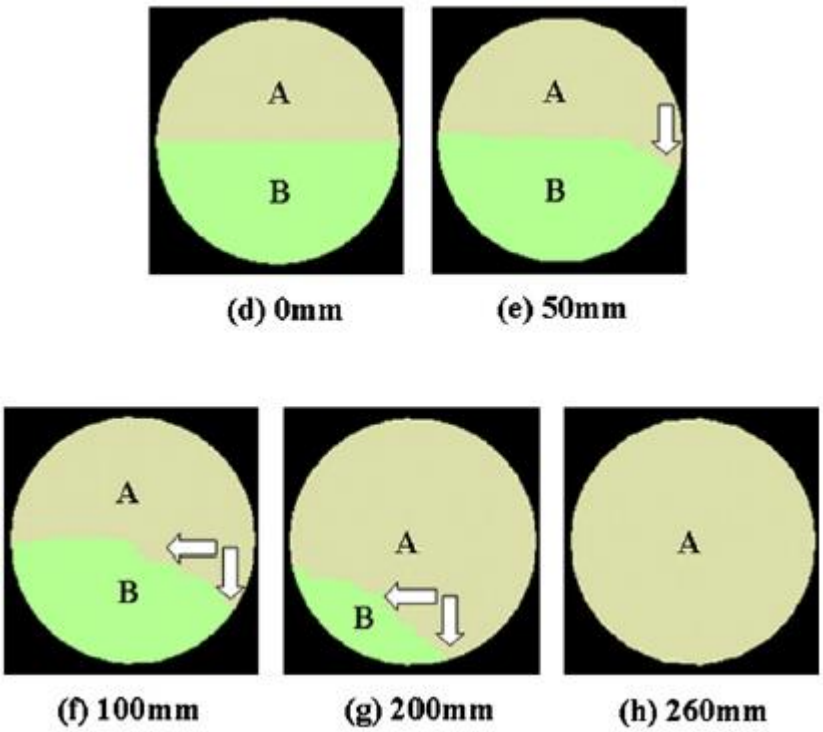

Figure 20 Bicrystal competition, grain A is growing perpendicular to the page while grain B is tilted to the left (Meng et al. 2012).

Moreover, work on nickel superalloy bi-crystals suggests more complex competition interactions also require consideration (Meng et al. 2012). In this work when the misaligned dendrite is growing towards the aligned dendrite, the approaching tips have the potential to slow the growth of the aligned dendrite enough for another primary trunk from the misaligned grain to grow ahead and impede it. When the misaligned dendrite grows away from the aligned dendrite, the aligned one dominates as expected, and when the angle is along the boundary, then the aligned dendrite grows around the side of the misaligned one and eliminates it more slowly, as shown in *Figure 20*. However, in real world situations, even when the misaligned grain grows into and impinges an aligned grain, it will typically only affect part of the grain and be later overgrown by the preferentially oriented grain encroaching from the side.

Another often overlooked complicating factor is the orientation of the secondary arms on the interacting grains. (Liu et al. 2013) have shown that when grains are converging, the rotation of the secondary arms around the primary trunks is also significant. They conclude that "the favourably oriented grain should be redefined as that with the secondary dendrite perpendicular to the grain boundary …, rather than the primary dendrite parallel to the heat gradient, as generally accepted". This is because there were differences in competition between the theoretically well aligned grain having secondary dendrites growing towards the misaligned grain (allowing for 2d consideration of

the system) vs those whose secondary dendrites were rotated, forcing a full 3d assessment. This distinction makes sense, since in the former case the secondary dendrites will more effectively impinge on the misaligned grains tip and prevent it growing into the aligned dendrites main trunk. These two conditions are shown in *Figure 21*. However, it also seems likely that rotating grain B by 45°would also influence competition.

The secondary dendrite arm spacing is a common measurement used in understanding the microstructure of a metal alloy - this is simply the average space between the arms branching off the primary dendrites and a standard equation for its value is

$$\lambda_2 = a\dot{T}^{-b} \qquad \textit{Eqn 5}$$

where $\dot{T}$ is the cooling rate in that region and a and b are fitting parameters related to the material composition. While the impacts of various alloying elements are generally known, at least in a broad sense, models to accurately predict the exact effects, especially for combinations of elements, are not available, so the values of a and b are determined experimentally. Factors that refine primary spacing will also tend to refine secondary spacing, however primary spacing is determined by dendrite formation early in solidification and will only change slowly after this, whereas secondary spacing is determined by coarsening in the later stages of solidification, making them more susceptible to changes in conditions throughout solidification. This coarsening also means that the SDAS near the tip of a dendrite is unrepresentative, and that for consistent results measurements should be taken far from the tip (Fredriksson 2012).

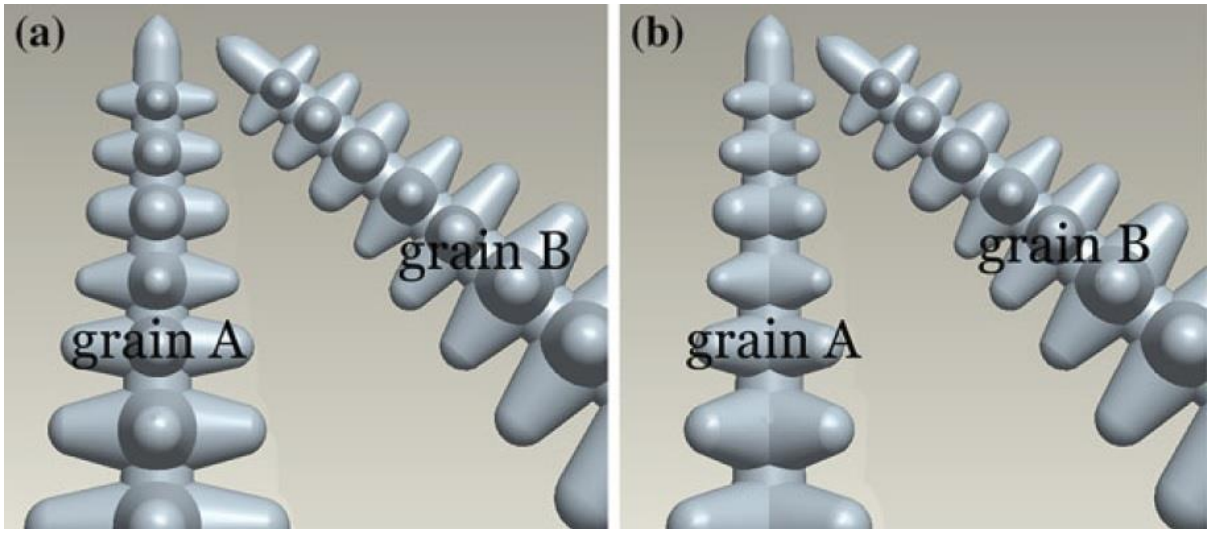

Figure 21 The different geometries of grain competition discussed, in a), grain As secondary dendrites impede B's approach and A dominates as expected, in b) grain B slows A's tip and overtakes. (Liu et al. 2013)

Additionally, there is a 'seaweed structure' when two axes of a single dendrite both have a similar misorientation there may not be a clear primary dendrite, and, if conditions permit, then secondary

branches can also become primary trunks. Depending on other nearby grains, these may either rapidly grow to one side with many secondary fronds growing back the other way from the top side or have a tight, almost vertical core as the primary orientation rapidly switches back and forth, with secondary arms on both sides at a steep angle, promptly blocked by neighbouring grains. Since these structures only develop when no axis is well aligned, they tend to be short lived and not reach any significant depth, except under experimental conditions are specifically designed to promote them, such as in single crystal solidification.

(Ziv and Weinberg 1989) showed that for one particular alloy (Al-3%Cu), the columnar to equiaxed transition (CET) occurs when the thermal gradient drops below a critical value, which in this case is 0.6K/s. This was shown by adding layers or insulation throughout the tests and observing that as the heat extraction dropped, so did the thermal gradient, and this led to the CET occurring earlier in solidification. (Shibata et al. 2006) used steels in their work looking at modelling the equiaxed fraction, which is strongly related to the depth of the columnar to equiaxed transition for a given thickness of material.

2.5 Dendrite Coarsening

The rate of dendrite coarsening in a system is described by the coarsening constant, several models have been proposed to calculate this value, they are shown in *Table 3* along with their main assumptions.

An obvious limitation of the Kattamis-Flemming model is that since it is isothermal, it assumes a constant temperature, which is a poor representation of conditions during casting.

Since the coarsening constants calculated from the Mortensen models are only expected to be accurate within about a factor of 2, due to the sensitivity of the SDAS to the history of conditions throughout solidification, the Voorhes-Glicksman model offers better precision, but is more mathematically involved, meaning simulations are required and can become processor intensive. Ultimately, both experimental error and the specific geometry of a system provide significant variation in experimental results so there are limits to the consistency of experimental data that can be used to confirm the accuracy of models (Mortensen 1991).

Table 3 Several common coarsening constant models and the relevant assumptions (Stefanescu 2002)

Model	Coarsening constant	Basic assumptions
Kattamis-Flemings, 1965	$\mu_o = \frac{20 D_L \Gamma \ln(C_E/C_o)}{m_L C_L (k-1)(C_E - C_o)}$	isothermal coarsening, of spheres; see inset for derivation
Ardell, 1972	$\mu_o = \frac{v_m^2 \gamma_{SL} C_o D_L}{RT}(1-C_o)\frac{1-f}{f}$	dynamic coarsening of spheres, diffusion of solute depends on a characteristic distance defined by the main free path
Voorhes-Glicksman, 1984	$\mu_o = \frac{8}{9}\frac{v_m^2 \gamma_{SL} C_o D_L}{RT}\frac{\alpha^3}{1-f^{1/3}}$ α: fct. of f_S given in tabulated form	solution of dynamic multiparticle diffusion problem; random pattern of precipitates generated by Monte Carlo simulation
Mortensen, 1991	$\mu_o = \frac{27 D_L \Gamma}{2 m_L C_L (k-1) f_S^{2/3}(1-f_S^{1/3})}$	dynamic coarsening of spheres
	$\mu_o = \frac{27 D_L \Gamma}{4 m_L C_L (k-1) f_S (1-f_S^{1/2})}$	dynamic coarsening of cylinders

There are several equations available to predict the stable spacing between the primary dendrites - the most relevant to this work are Eqn 6 and Eqn 7.

$$\lambda_1 = 4.3\left(\frac{D\Gamma\Delta T_0}{k}\right)^{\frac{1}{4}} V^{-\frac{1}{4}} G^{-\frac{1}{2}} \qquad \textit{Eqn 6}$$

$$\lambda_1 = 6(\Delta T_0 k D\Gamma)^{\frac{1}{4}} V^{-\frac{1}{4}} G^{-\frac{1}{2}}\left[1 - \left(\frac{DG}{V}\Delta T_0 k\right)\right]^{\frac{1}{2}} \qquad \textit{Eqn 7}$$

Where ΔT_0 is the solidus to liquidus temperature range of the initial composition, D is the diffusion coefficient, Γ the Gibbs Thompson coefficient, k the equilibrium partition coefficient, V the interface velocity and G the interface temperature gradient. However, it is acknowledged that these equations do not provide exact results and tend to only be suited to providing a general idea of expected behaviours rather than quantitative values (Kurz and Fisher 2005).

A likely factor in this discrepancy is that in a given environmental condition there are a range of stable (or at least metastable) dendrite spacings, and the exact spacing from the range of stable possibilities is determined by the system's history (Ding et al. 1996, Lin et al. 1999). Dendrites will begin to grow at the optimum spacing for the current conditions, but will then need time to adjust if the conditions change, and even then the change must produce a suitably large driving force. Interestingly, while the dendrite spacing changes slowly, the dendrite tip radius is much more responsive to changing conditions (Makkonen 2000). The practical upshot of this is further emphasis that in experiments on solidification microstructure the important parameters, namely, temperature gradient and interface velocity need to be carefully controlled from the liquidus to the solidus. This implies that for the same final cooling rate, initially rapid solidification slowing down will produce a finer primary dendrite spacing than an initially slow cooling rate that is accelerated (Ma 2004). While grain size and primary dendrite spacing both tend to respond similarly to changes in solidification conditions - for example, although both are refined by large increases in cooling rate, they are not

directly related and grain refinement by inoculation tends to have no effect at all on the dendrite spacing of a material (Glenn, Russo and Paterson 2003). While the difference between the minimum and maximum spacing for a given condition is often reported as being a factor of 2, although some authors have reported differences of four times (Wang et al. 2012b).

2.6 Columnar Zone

Deeper into the material, local undercooling does not have the chance to reach a level that permits nucleation before grains that formed nearer the surface grow to that depth, so grain growth takes over and the columnar region is dominated by elongated grains oriented near the thermal gradient. Due to the random nature of nucleation events in the chill zone, a large range of crystal orientations exists in the chill zone grains and columnar grains near the surface. However, as growth progresses deeper into the material the poorly aligned grains are eliminated and only the grains with alignments close to the thermal gradient survive (Boultbee and Schofield 1981).

The maximum depth of the columnar zone before its transition to the central equiaxed zone varies with both composition and thermal path. (Zhang, Kim and Hong 2005) showed columnar zones extending 4-13mm into Al-5%Cu alloys with starting melt temperatures ranging from 930-1000K. (Doherty et al. 1977) also looked at a range of Al alloys, under various solidification conditions, and found columnar zones could be adjusted, from virtually absent, to extending a full 20mm to the centre of the small ingots produced. (Mahapatra and Weinberg 1987) obtained columnar to equiaxed transitions at heights of 30-80mm up directionally cooled Sn-Pb alloys by varying the composition and superheat, with a note that some conditions did not produce the transition at all. Other work has produced steel ingots and, by manipulating composition, were able to vary the columnar zone from entirely absent to the full 40mm half thickness of the material (Kimura et al. 2013).

Figure 22 shows the extent of columnar growth observed in steels by various researchers, from literature, with the lines representing the maximum possible depth in the experiment. (Sasaki et al. 2009) and (Kimura et al. 2013) achieved such extreme variation in morphology by adding elements that encourage inclusion formation in the liquid (TiB, and TiN respectively) to stimuate equiaxed formation. While (Villafuerte, Pardo and Kerr 1990) demonstrates the development of a central equiaxed zone after only a short distance in welds, this ties back into other work that has been discussed that consiedered the columnar to equiaxed ratio, indicating that the depth of transition is a function of the thickness of the material. (Hurtuk and Tzavaras 1982) did work on 8620 grade steels and found that increasing superheat led to an increase in the extent of the columnar zone and

found a complex relationship with C content. Increasing C content would reduce the columnar length up to 0.1 wt% C, after which it would begin increasing the maximum extent of the columnar zone. Then at around 0.6 wt% C the columnar zone would begin shrinking again - this behaviour was also found in a simple Fe-C binary and a similar behaviour in Fe-Ni binary This behaviour was attributed to the peritectic reaction, and the deformation caused by the changes in density between δ and γ structures. The paper by Hurtuk fails to specify the size of ingots used (represented by the fading line), putting some limitations on the conclusions that can be drawn from that paper.

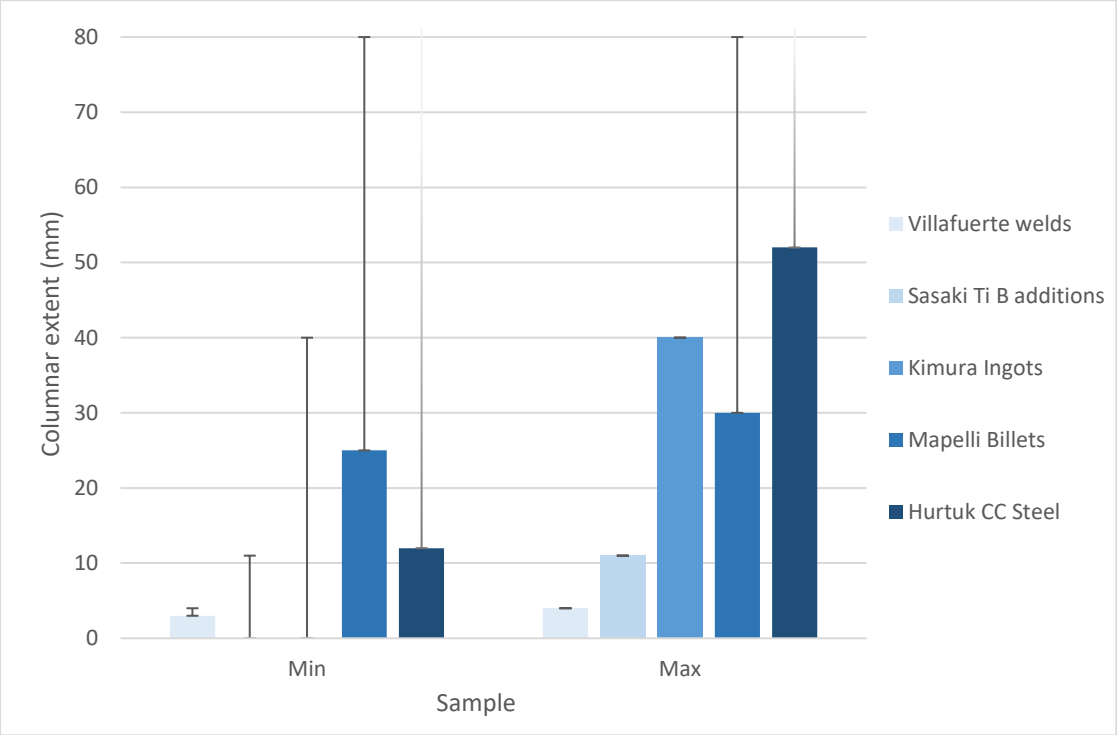

Figure 22 The extent of the columnar zone for various steels in various conditions, the bar is the extent of the columnar zone and the line the centre of the material (maximum possible depth) fading out where none was reported

According to a recent paper modelling columnar competition (Takaki et al. 2018) Kolmogorov has previously presented a relationship between the starting grains and surviving grains at a specific depth

$$N(z,\rho) = \frac{c}{\sqrt{\rho z^n}} \qquad \textit{Eqn 8}$$

Where N is the number of grains, z the distance from the precipitating surface, ρ the initial grain density, c is a constant and n is an exponent (either 0.5 in 2D or 1 in 3D). The constant c is essentially a fitting parameter that can rescale the rate of decay in the range of orientations present.

2.7 Equiaxed zone

As growth progresses deeper into the material, there is a greater thickness of material that the heat must pass through to be extracted, so cooling slows. Eventually this allows small fragments of solid material to be carried into the bulk liquid ahead of the solidification front, leading to a central region

of large randomly oriented grains called the equiaxed zone. It is the dependence on seeding of new grains from the liquid that is the cause of the random orientation and broadly isotropic grain sizes, while the reduced cooling rate compared to the surface supresses nucleation and allows the grains to become larger (Flemings 1974).

2.8 Segregation

Due to a combination of an alloy solidifying over a range of temperatures and the alloying elements having different stabilities in different phases (typically being highly soluble in the disordered liquid phase but much less soluble in the various solid phases), segregation is a common occurrence in steels. While most solute elements will segregate into the remaining liquid, there are some exceptions. For example, aluminium is only soluble in liquid iron up to about 11% wt, meaning that at concentrations above this the aluminium will preferentially segregate out into a solid phase, rather than remaining in the liquid.

Segregation occurs on both micro and macro scales -for simplicity, this discussion will assume segregation into the liquid, as segregation into the solid is essentially the opposite behaviour.

In macrosegregation, only some of the alloy element is incorporated into the lattice as the surface solidifies, and the solidification front pushes the rest deeper into the material. As the solidification front continues to advance this causes a gradually increasing amount of the alloying elements to be pushed ahead of the front, eventually causing a highly enriched core with a very different composition from the surface layers. This leads to the initial solidifying material being depleted and the final solidifying material is highly enriched. If the build-up reaches a point where the solidifying material is at the composition of the starting liquid, then a steady state will develop where the concentration in the solidifying material becomes stable. This steady state persists until the small pocket of final solidifying material where there is no longer additional liquid to hold the rejected material, so the concentration increases sharply at this point (Flemings 1974).

In microsegregation, the alloying elements are pushed out around the dendrites as they grow, and the enriched liquid regions are surrounded as the dendrites connect, leading to pockets of enriched material which are typically micrometres across. Microsegregation can be reduced or removed by holding the solid material at an elevated temperature for a period of time to encourage diffusion. This process typically takes many hours to remove substitutional solution element micro-segregation, which can be over distances of 100+ µm for slow cooled continuous cast slab (but is quicker if smaller, more mobile atoms, are concerned) and can be impractical in a high-volume industrial environment. However, rolling, which is common in sheet steel production, reduces the spacing between the solute rich and solute poor regions, which is far more favourable to rapidly

equalising composition gradients on heat treatment if required. In addition elemental partitioning during solid state diffusional phase transformation can also change the levels of micro-segregation in the final product (Elorez and Antonio 2017).

Macrosegregation however, is completely impractical to remove without completely re-melting the steel and the regions of different chemical compositions will tend to have significant differences in properties, particularly the large seam of highly enriched material that can form in the centre of continuously cast steels. While a suitably high cooling rate will reduce macrosegregation by restricting long range atomic mobility, a very slow solidification would also theoretically work, since the prolonged time at an elevated temperature allows for diffusion through the material to restore an equilibrium, but this approach is impractically slow for manufacturing environments. Agitation will tend to break off dendrites and move them to other regions where they can act as nucleation sites, as well as maintaining a homogeneous liquid phase. This tends to prevent macrosegregation, but not necessarily microsegregation (Fredriksson 2012).

Table 4 shows partition coefficients for a variety of alloying elements commonly used in steel, however many variables can impact the specifics of element segregation, such as concentration, other elements in the alloy, and temperature, so these should only be considered as approximations based on how strongly the elements partition relative to each other at low concentrations. For example, work has shown antagonistic segregation patterns of manganese and aluminium in steel. Grades with a significant fraction of each and multiphase solidification paths may end up with aluminium enriched ferrite regions and manganese enriched austenite regions (Ennis et al. 2016). This table shows that Al, the main alloying element in the steels used in this work only segregates weakly, so while an understanding of segregation is useful for broadly understanding solidification, it plays a relatively minor role in the grades studied.

Table 4 Equilibrium partition ratios for low concentrations of many alloying elements commonly found in steel, comparing concentrations in both ferrite and austenite to the liquid phase (Ghosh 2001)

	K_e	
Element	δ-Iron	γ-Iron
Al	0·92	–
C	0·13	0·36
Cr	0·95	0·85
H	0·32	0·45
Mn	0·84	0·95
Mo	0·80	0·60
Ni	0·80	0·95
N	0·28	0·54
O	0·02	0·02
P	0·13	0·06
Si	0·66	0·5
S	0·02	0·02
Ti	0·14	0·07
V	0·90	–

Theoretical approaches to obtaining values for the partition coefficient, such as those shown in *Table 4*, typically assume equilibrium conditions, which in practice is rarely the case. However, they still serve as good approximations, and it may be possible to take samples of the material in question and obtain results directly. The partition coefficient can be calculated as

$$K = C_s/C_l \qquad \textit{Eqn 9}$$

where C_s and C_l are the concentrations of solute in the solid and the liquid phases. This can be generalised to any 2 phases in contact with each other, where the partition ratio between them is simply the ratio of solute concentrations in phases 1 and 2

$$K = C_1/C_2 \qquad \textit{Eqn 10}$$

However, atom transfer between two solid phases will be very slow, especially at ambient temperatures, so in a practical setting whatever segregation patterns are established during solidification are, for the most part, set. The partition ratios shown in *Table 4* cover many steel alloying elements for both ferrite and austenite compared to the liquid phase. A number greater than 1 will preferentially segregate out of the liquid into the solid phase, while numbers between 0 and 1 build-up in the liquid phase with segregation behaviour becoming more severe as the number is further from 1. The same logic applies when solidification has resulted in two solid phases, as elements will preferentially segregate into the material with the larger partition coefficient for that

alloying element. However, since the numbers in the table above have not been normalised for that situation, the degree of segregation is harder to work out. In either case, these values are only approximate for real situations, as the cooling rate will influence back diffusion, and the various alloying elements will also interact with each other, causing deviation from the results in binary compositions (Ocansey and Pourier 1996). While Eqn 10, which compares concentrations of elements between phases, is a good approximation, at least at low concentrations, it is technically more accurate to compare the activity of the element between phases as shown in Eqn 11 (Ghosh 2001)

$$K_e = a_{s/}a_l \qquad \textit{Eqn 11}$$

It is worth noting that while solidification cannot occur either at equilibrium or instantaneously, the simplest models typically assume one of these extremes (Ermakova, Sheshukov and Marshuk 2010). Despite this, each of the most common approaches offers reasonable agreement within a range of suitably comparable conditions.

Since the relative activities of a solute in two phases can be impacted by both other solutes and the temperature of the system, as well as the concentration of the solute itself, models can quickly become prohibitively complex, but even with many simplifying assumptions it is still easy to reach a reasonable approximation of expected segregation behaviour. Equilibrium conditions assume complete mixing in both phases, which ultimately leads to the Lever rule,

$$C_s = \frac{kC_0}{(1-f_s)+kf_s} \qquad \textit{Eqn 12}$$

where $f_s$is the fraction of solid at the time being considered. This approach is generally a good model for cooling rates below 1K/s. Another approach, which approximates instantaneous cooling and is mostly suitable at cooling rates over 100K/s, is to assume complete mixing in the liquid but no diffusion in the solid, which leads to the Scheil equation,

$$r = (1 - f_s)^{K_e - 1} = C_l/C_0 \qquad \textit{Eqn 13}$$

Where r is a measure of enrichment within the remaining liquid and C_0 is the concentration of solute across all material being considered. Or alternatively

$$c_s = kc_0(1 - f_s)^{(k-1)} \qquad \textit{Eqn 14}$$

In an iron based system under normal casting conditions metallic additions typically move slowly enough that the Scheil equation is suitably accurate, but in larger, slower solidifying casts carbon is often best considered using the Lever rule (Pfeiler 2007).

Table 5 Various solidification models (Stefanescu 2002)

Model	Geometry	Solid diffusion	Liquid diffusion	Partition coefficient	Growth	Coars-ening
Lever rule	no restriction	complete	complete	variable	no restriction	No
Scheil (1942)	no restriction	No	complete	constant	no restriction	No
Brody-Flemings (1966)	no restriction	Incomplete	complete	constant	no restriction	No
Clyne-Kurz (1981)	no restriction	spline fit	complete	constant	no restriction	No
Ohnaka (1986)	linear, columnar	quadratic equation	complete	constant	linear parabolic	No
Sarreal-Abbaschian (1986)	no restriction	limited	complete	constant	no restriction	No
Kobayashi (1988)	columnar	limited	complete	constant	linear	No
Nastac-Stefanescu (1993)	plate, columnar, equiaxed	limited	limited	variable	no restriction	Yes

Table 6 Assumptions used in various solidification models (Stefanescu 2002)

Model	Equation	Eq. no
Lever rule	$C_S = k\,C_o / \left[(1-f_S) + k\,f_S\right]$	(7.12)
Scheil (1942)	$C_S = k\,C_o (1-f_S)^{k-1}$	(7.13)
Brody-Flemings (1966)	$C_S = k\,C_o\left[1-(1-2\alpha k) f_S\right]^{(k-1)/(1-2\alpha k)}$ with $\alpha = 4D_S t_f / \lambda^2$	(7.14)
Clyne-Kurz (1981)	$C_S = k\,C_o\left[1-(1-2\Omega k) f_S\right]^{(k-1)/(1-2\Omega k)}$	(7.15)
	with $\Omega = \alpha\left[1-\exp(-1/\alpha)\right] - 0.5\exp(-1/2\alpha)$	
Ohnaka (1986)	$C_S = k\,C_o\left[1-(1-2\beta k) f_S\right]^{(k-1)/(1-2\beta k)}$	(7.16)
	with $\beta = 2\gamma/(1+2\gamma)$ $\gamma = 8D_S t_f / \lambda_1^2$	
Kobayashi (1988)	$C_S = k\,C_o\,\xi^{(k-1)/(1-\beta k)}\left\{1+\Gamma\left[0.5\left(\xi^{-2}-1\right) - 2\left(\xi^{-1}-1\right) - \ln\xi\right]\right\}$	(7.17)
	with $\xi = 1-(1-\beta k) f_S$ $\Gamma = \beta^3 k(k-1)\left[(1+\beta)k-2\right](4\gamma)^{-1}(1-\beta k)^{-3}$	
Nastac-Stefanescu (1993)	$C_S^* = kC_o\left[1-\dfrac{(1-k) f_S}{1-(m+1)\left(k I_S^{(m+1)} + I_L^{(m+1)}\right)}\right]^{-1}$ $f_S = \left(r^*/r_f\right)^{m+1}$	(7.18)
	see text for I_S and I_L	

There are a variety of other models used for understanding the segregation behaviour of materials. and *Table 6* show many of the most well-known, along with the assumptions made by each respectively. These varying assumptions mean they are best suited to different situations. For example, the Lever rule assumes complete diffusion in both the solid and liquid phases, so it is most accurate at equilibrium conditions where the solidification rate is so slow that it allows time for diffusion through the solid phase, which is impractical in most real-world scenarios, and certainly in a manufacturing environment, however the results can still be close enough to reality to offer at least some insight. The Scheil equation assumes no diffusion in the solid phase, but full diffusion throughout the liquid phase, so it is best suited to rapid solidification when there are convection

currents or turbulence to continuously mix the liquid phase. The other models assume partial diffusion through the solid and complete or partial mixing of the liquid, which makes them valuable in intermediate conditions, where neither the Lever or Scheil approach is particularly accurate. However, they are also significantly more complex and thus computationally intensive, but by using both Lever and Scheil it is relatively straight forward to at least estimate upper- and lower- bounds, in order to predict approximate behaviour.

2.9 Grade specifics

As previously indicated there has been a long term interest in low density steels, but it is only recently that significant work has been done on them due to the growing prevalence of more suitable manufacturing techniques introducing the possibility of profitably producing these grades. For compositions where the addition of Al does not induce a phase change in the material, each 1% addition of Al gives approximately a 1.5% density reduction due to a combination of the Al atoms being lighter than Fe atoms and Al distorting the crystal lattice (Sohn et al. 2013). Most work on low density steels focuses on the Fe-Al-Mn-C system, some grades of this system are seeing use in niche applications, but they also hint at suitability for more widespread use if new casting techniques offer a viable manufacturing route (Kim, Suh and Kim 2013) (Chen et al. 2017).

As previously discussed, the most prominent difficulty with these grades is the increased susceptibility to cracking during the extreme deformation of conventional continuous casting techniques. Work by Shon et al (Sohn et al. 2013) varied the composition of automotive steels from 4%-6% and showed that the 6%Al grade had increased cracking, caused by more and larger κ carbides, which due to their hardness will not deform with the surrounding metallic phases, creating voids and initiating crack growth. This work also suggested that κ carbide growth occurs mostly between the rolling and coiling temperatures, so rapid cooling would minimise their development, supporting the idea that near net shape casting techniques, with their increased cooling rates could be well suited to producing these high Al grades. However other work suggests that with sufficiently high C and Al concentrations κ carbides will form even when the cast is quenched (Kim et al. 2013).

Fe-Al-Mn-C grades can be broadly split into three categories depending on their phases at ambient temperatures, ferritic grades are produced by having a large amount of Al and very little Mn or C, large amounts of Mn and/or C produce austenitic grades, while intermediate values produce multiphase steels, typically duplex or triplex. Since the ferritic grades have no solid state phase transitions through cooling they pose difficulties in efficiently producing microstructures that are suitably fine for industrial uses, and some work has concluded they are simply not viable. Austenitic grades however behave like many conventional austenitic grades in that they solidify as δ ferrite

before changing to austenite during cooling, allowing for recrystallization, making them the more likely candidate for industrial use (Chen et al. 2017) The third group is multi-phase steels, these are typically TWIP and TRIP steels, with the fine balance of multiple phases allowing for strain induced phase transformations that give a high level of work hardening.

High aluminium steels, (<11%wt Al) - below this threshold the structure remains as a solid solution of Al in Fe, but the high Al content can still cause some development of an FeAl intermetallic phase, making these materials prone to hot cracking. They also tend to have a narrow mushy zone causing grains to grow very large, as discussed below, and since the high fraction of Al generally makes them be fully ferritic, there is no grain refinement from solid state phase changes, limiting the physical properties. However, they are significantly lighter than conventional steels and refining the microstructure should allow good mechanical properties to be maintained, the low-density steels in the experimental part of this work are of this type.

TWIP (twinning induced plasticity) steels both begin to deform plastically at relatively low stress, but have high ultimate tensile strengths. Not only do they have a large deformation range but they also show a high rate of strain hardening, (Yi 2014) (Grässel et al. 2000), this makes them excellent at absorbing energy during accidents, so they have significant value for use in safety components. TWIP steels gain their properties from twinning, where multiple crystals grow into each other and line up in some orientations, different to standard grain boundaries where the crystals do not line up. This twinning leads to the high work hardening rate. This high rate of work hardening prevents necking, allowing plastic deformation to continue in a linear fashion longer than in most materials before failure occurs (Kang et al. 2011).

The high work hardening rate means that as a region is deformed it becomes stronger, even to the point where under a tensile load the thinning section of material becomes stronger faster than it becomes thinner, and exceeds the strength of the undeformed regions. This restricts strain to the least deformed regions -therefore, these materials effectively distribute strain and failure only occurs once much of the material is approaching its work hardening limit. The high alloy concentration, particularly Mn, makes both micro and macro segregation especially severe, so the increased cooling rates found in near net casting methods should improve the commercial viability of this class of steels by reducing cooling time to such a degree that macro segregation is still low. However, if the cooling rate is only moderately increased, it is possible that there is enough time for segregation to occur but then back diffusion is restricted, providing a window of mid-tier cooling rates where material properties are worse than at either low or high cooling rates(Kang et al. 2011).

While work has been done on a variety of difficult to manufacture steel grades, particularly TRIP, TWIP, and high Si grades that are already in use, little has been focused on high Al steels like those

studied in this work. Those grades that are already in uses have relatively low volume niche uses, or add significant value over more conventional grades, which has previously allowed more labour-intensive production techniques to be viable. In contrast to the high Al steels studied here, which are expected to be required in bulk with more moderate improvements in properties and as such need developments in continuous casting techniques before becoming commercially interesting.
Grades containing Al along with a higher proportion of Mn and C produce austenitic low density steels which benefit from recrystallisation.

2.10 Factor influencing solidification growth behaviours

Once nucleation has occurred, solidification begins. Pure elements (and mixtures at their eutectic composition) at a fixed pressure tend to have a single temperature where the solid-liquid transition takes place, however mixtures such as (non-eutectic) alloys freeze and melt over a range of temperatures, making the solidification process more difficult to understand. Under equilibrium conditions solidification starts at the liquidus temperature and then continues until the last of the material solidifies at the solidus. The gap between these two temperatures results in most compositions of solidifying steel having a 'mushy zone', a range of temperatures where both solid and liquid phases are stable in varying proportions. While the proportion of each phase is set for a fixed temperature, the structure itself is not, as the high temperature allows for atomic movements to reduce the surface area between the phases over time. In practical conditions this mushy zone means dendrites or grains develop while still surrounded by liquid, gradually growing larger as the temperature drops. While any material approaching an infinitely low cooling rate will experience a single (or at least very small number of) nucleation event(s), solidification in the real world happens on much more practical timescales. Because of this, the width of this mushy zone is a major factor in determining the grain size in the solidified material, with a wider mushy zone producing finer grains, and a narrower mushy zone coarser grains (Xu et al. 2006).

2.10.1 Composition Effects

The reasons for this are thermodynamic, it is very well understood that first order phase changes come with the release or absorption of latent heat, during solidification, the latent heat of fusion is released - the amount of heat released is dependent on the enthalpy change between the two states (Lee 2011). This then influences the undercooling of the material. As the previously discussed, significant undercooling is required to allow new grains to nucleate, but established grains will continue to grow with even the most minor undercooling. Thus, as a material with a narrow mushy zone will release its latent heat rapidly, this restricts undercooling and inhibits nucleation while still

allowing grain growth to occur (Glicksman 2011). However, the relationship is not linear, so there are still some ranges of conditions where even materials with narrow mushy zones can have their nucleation rate influenced by cooling rate. However there are other regions where the grain size will be relatively stable, showing only minor changes with changes in conditions.
It has already been alluded to that the composition of a liquid can have a significant impact on the solidification properties. At a basic level, adding a large amount of a ferrite or austenite stabilising element will force that phase at the expense of the other.

2.10.2 Cooling rate

As a rule, heat transfer from the bulk of the material is too slow to have a significant effect on initial surface nucleation, as the hot liquid first contacts the cold mould surface, meaning that for similar grades and mould materials, different cast thicknesses will have similar surface features, even if later solidification progresses differently. There are several effects of cooling rate on the bulk features, first, a lower cooling rate leads to larger dendritic structures, *Figure 23* shows both the primary and secondary dendrite spacings in a high carbon billet increasing with a consistent 2:1 ratio as the cooling rate reduces towards the centre of the billet (Ganguly and Choudhary 2009). (Imagumbai 1994) also looked at several C-Mn steels with varying cooling rates and found a trend towards a 2:1 ratio of primary and secondary dendrites. Second, a higher cooling rate increases the driving force from the thermal gradient, which in turn reduces the growth rate differential between well aligned and poorly aligned grains, meaning that columnar competition is less pronounced and poorly aligned grains are eliminated more slowly. This also implies that after identical nucleation conditions, a higher cooling rate will have smaller grains in the columnar region than a lower cooling rate, since less have been eliminated, so a higher cooling rate leads to finer grain sizes and a more diffuse texture. Third, the cooling rate plays an important factor in determining the morphology of the solidification front. If it is suitably low, then dendrites will fail to form and a planar front will be seen, whereas at the other extreme, exceptionally high cooling rates can cause homogeneous nucleation, or produce an amorphous glassy structure.
A higher cooling rate also leads to greater undercooling in the central equiaxed region, causing more nucleation and reducing grain size. This interplay of factors mean that materials can have chaotic ranges of cooling rates, where a small change in cooling strongly influences the final grain size, and more stable regions, where a large change in cooling rate only has a minor effect on the solidification structure (Woodruff 1973). Additionally, in the central equiaxed zone, a lower cooling rate will mean less undercooling, which strongly inhibits additional nucleation while only having a

moderate influence on grain growth. Therefore, lower cooling rates will lead to larger grains in the central equiaxed region as well.

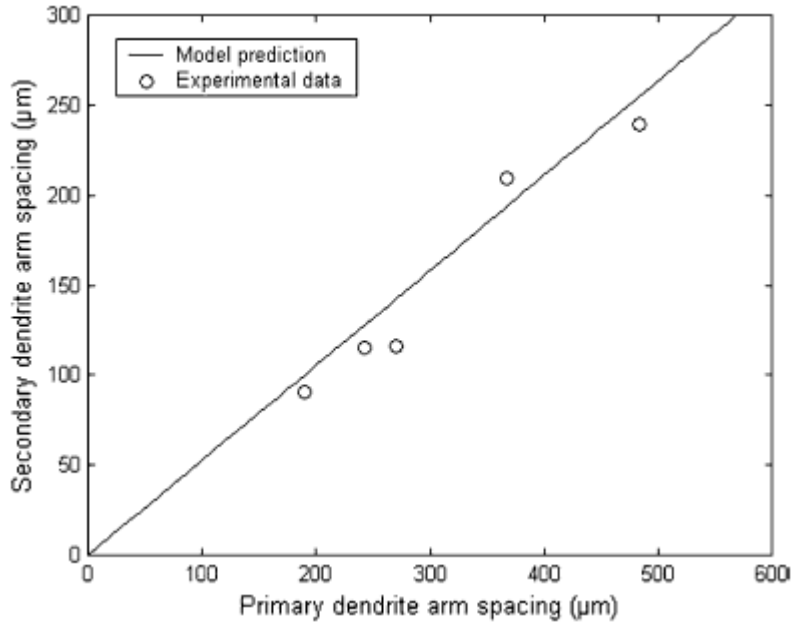

Figure 23 Variation of SDAS and PDAS through the thickness of a high carbon billet (Ganguly and Choudhary 2009)

2.10.3 Undercooling

It has previously been stated that undercooling affects the growth rate and nucleation rate differently, the effect of undercooling on growth rate is given by

$$V = \frac{\lambda}{\sigma T_M} \frac{(T_M - T_0)^2}{4} \qquad \textit{Eqn 15}$$

Where T_M is the temperature of the melting point for a planar interface, T_0 is the temperature of the melt far from the interface, λ is the thermal conductivity and σ is the surface tension thus T_M-T_0 is the undercooling and all other parameters are constant for the material causing the growth rate to be dependent on the square of the undercooling. In alloys this equation is replaced by

$$V = \mu(T_L - T)^n \qquad \textit{Eqn 16}$$

Where T is the temperature at the tip, T_L the liquidus temperature, meaning that T_L-T is now the undercooling, μ is the constant which now includes additional factors such as mass transport across the interface and n is another constant.

In contrast to this, the size distribution of potential nucleation points follows the Boltzmann distribution, and since in practice some sort of inhomogeneity is required to trigger heterogeneous nucleation the number of critical nuclei is given by

$$n^* = ne^{\frac{\Delta G^*}{k_B T}} \qquad \textit{Eqn 17}$$

Where n is the number of atoms in contact with the nucleation promoting heterogeneity, K_B is the Boltzmann constant and ΔG^* is the Gibbs energy of formation after accounting for the reduction due to nucleation promoting inoculants or surfaces (Fredriksson 2012). Ultimately material solidifying onto an already existing structure produces less additional surface area than that same material solidifying as a new nucleus, allowing grain growth to occur at any level of undercooling while a larger undercooling is required to nucleate new grains. Meaning that small undercoolings favour grain growth while large undercoolings encourage more nucleation, at least until solidification is rapid enough for the latent heat released to reduce undercooling.

2.11 Modelling and Simulation

Modern approaches to developing theoretical understandings of materials rely heavily on simulations and computer modelling. Thermo-Calc is a widely used software for the thermodynamics of a system and uses theoretical models of behaviours supported by results from experimentation. This thermodynamic data can then be fed into other software such as DICTRA or MICRESS, which develop a physical structure that evolves based on Thermo-Calcs thermodynamic data. (Borgenstam et al. 2000) (Engstrom, Hoglund and Agren 1994) (Bottger et al. 2008). While the outputs of this class of software tends to be robust for well studied materials and processes, where a large amount of experimental data corrects limitations of the models used, results for more unusual materials or processes tend to be less accurate, but still tend to give an indication of the structures and behaviours to expect. The software used in this work is discussed more in later sections.

2.11.1Thermo-Calc

The software Thermo-Calc has been used throughout this work, when the final versions of the phase diagrams were produced version 2017b and the TCFE7 database were used. Thermo-Calc has a wide range of applications, including predicting equilibrium phase changes and precipitate formation and is widely used to predict the solidification temperatures. In addition it can be used to predict the partition coefficients relevant for segregation behaviour. Non-equilibrium behaviour can also be considered by suppressing equilibrium reactions. Thermo-Calc uses the CALPHAD approach: CALPHAD stands for CALculation of PHAse Diagrams and is a methodology that combines thermodynamic properties of a material obtained through experiment and calculation, with experimental data mapping when phase transitions occur. The approach allows prediction of phases that exist under different conditions that may be challenging or time consuming experimentally, for example either under differing conditions or for novel compositions that have not been studied experimentally (Shin and Saal 2018).

Early work on phase diagrams involved calculating the minimum Gibbs energy by hand and drawing phase boundaries by hand (Spencer 2008), this was obviously time consuming and imprecise, meaning that the development of phase diagrams has been reliant on increases in computational power.
While the models for each phase may be wildly different from each other, for consistent and useful results they must generate the same values along boundaries (Lukas 2007).

Practical experimentation to determine the thermodynamic properties that are required for software such as Thermo-Calc can be broadly split onto three groups, calorimetric techniques most readily provide information relating to enthalpy or heat capacities, but has difficulties obtaining partial Gibbs energies. Mixing calorimetry combines two well defined samples that are different from each other, in its simplest version both initial samples will be at the same temperature since upon mixing the change in temperature will be exclusively a factor of the enthalpy of mixing. Drop and scanning calorimetry are two variants of the same process where a sample in equilibrium has its temperature changed, drop calorimetry uses a large ΔT making it suitable for finding the thermal capacity while the scanning variant uses a smaller ΔT more suited to testing the latent heat of phase transformations. While the other two classes of gas phase equilibria and electromotive force (EMF) based methods, are able to produce values for other properties such as the partial Gibbs energy. Galvanic cells can transfer atoms of one element between electrodes using an electric current, the partial Gibbs energy can be calculated from the amount of electric energy required. For mixtures with very different volatilities, the vapour phase will be a pure element, so comparing its partial pressure to the vapour pressure over the pure element, allowing calculation of the chemical potential (Lukas 2007).
For fixed conditions, each phase will have its own Gibbs energy, and the lowest energy phase will be most stable and therefore be the phase that is expected to exist. There are three standard components of a mixtures Gibbs energy

$$G_{mix}^{ideal} = RT(x_a lnx_a + x_b lnx_b) \qquad \textit{Eqn 18}$$

Is the ideal Gibbs energy for a binary system, where T is the temperature, R is the entropy of mixing for an ideal system and x_n is the phase fraction of each component. This assumes no interaction between particles, which is almost universally unrealistic and as such needs modifying with additional terms.

$$G_{mix}^{xs} = x_a x_b \Omega \qquad \textit{Eqn 19}$$

Ω is the solution interaction energy parameter, negative indicates an attractive force between components while positive represents a repulsive force. This gives the excess Gibbs energy (G_{mix}^{xs})

associated with interactions between the different constituents. A large positive Ω suggests a strong repulsive force and will cause two minima in the Gibbs energy, meaning that there are two stable phases. Combining these gives the equation below, and the effects of a strong positive or negative Ω are shown in *Figure 24*.

$$G = RT(x_a ln x_a + x_b ln x_b) + x_a x_b \Omega \qquad \textit{Eqn 20}$$

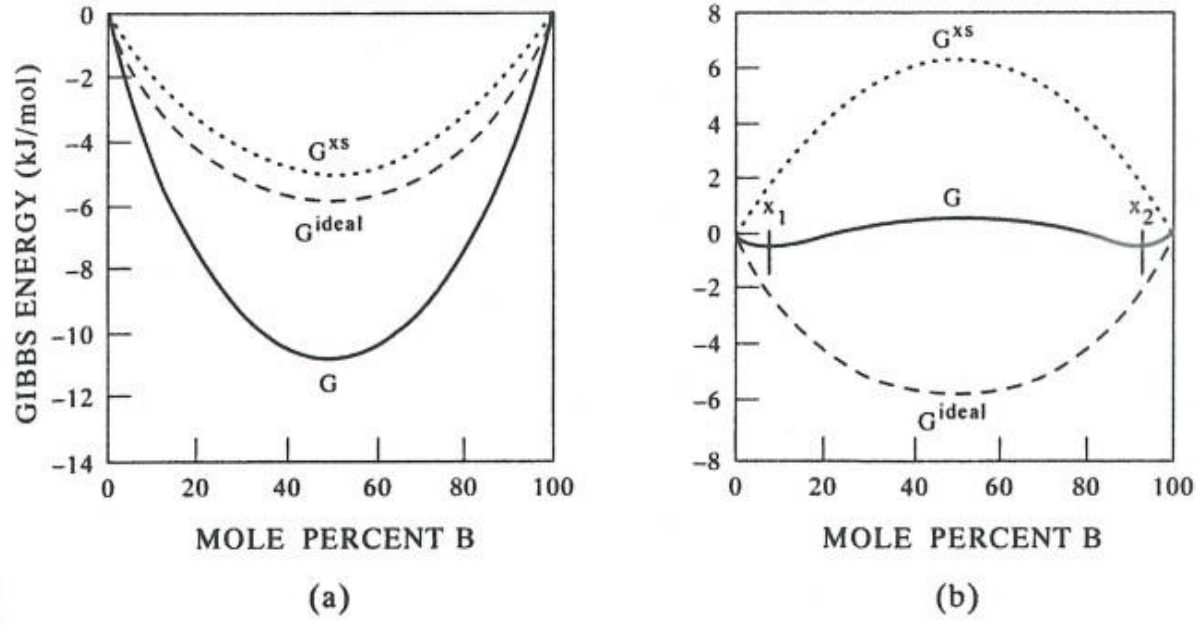

Figure 24 Influence of negative Ω (a) and a large positive Ω (b) on the excess and total Gibbs energy of a binary system (Saunders and Miodownik 1998).

The third component is the partial Gibbs energy of mixing, given by

$$G_{mix} = x_a \bar{G}_a + x_b \bar{G}_b \qquad \textit{Eqn 21}$$

With $\bar{G}_n$ being the partial Gibbs energy of each component in solution compared to a pure substance, this further offsets the previous assessments of the systems Gibbs energy, shown in *Figure 25*. Once multiple phases are considered in multiple component systems, a graph of mole fraction against Gibbs energy then shows different phases have their minimum at different mole fractions and regions along the tangent to two curves that is between those curves indicates both phases will exist, as shown in *Figure 26*. Beyond this there are numerous models that account for additional corrections that are specific to a given system, or at least class of systems, since this work focuses on steels the most obvious of these is an additional term for magnetic interactions. These magnetic effects are the cause of the unusual property in Fe based phase diagrams where the same crystal structure appears in two different temperature ranges, with both α and δ ferrite being bcc structures separated by γ austenite with a fcc structure. This magnetic contribution to the Gibbs energy of a pure element is given by

$$G^{mag} = -0.9RT_c \ln(\beta_0 + 1)\left(\frac{\beta^T}{\beta_0}\right) - RTln(\beta_0 - \beta^T + 1) \quad \text{Eqn } 22$$

Where the first term is the magnetic enthalpy and the second the magnetic entropy with β_0 being the saturation magnetisation at 0K and β^T the magnetisation at the current temperature, this then needs adjusting to account for the effect of other elements in the alloy (Saunders and Miodownik 1998).

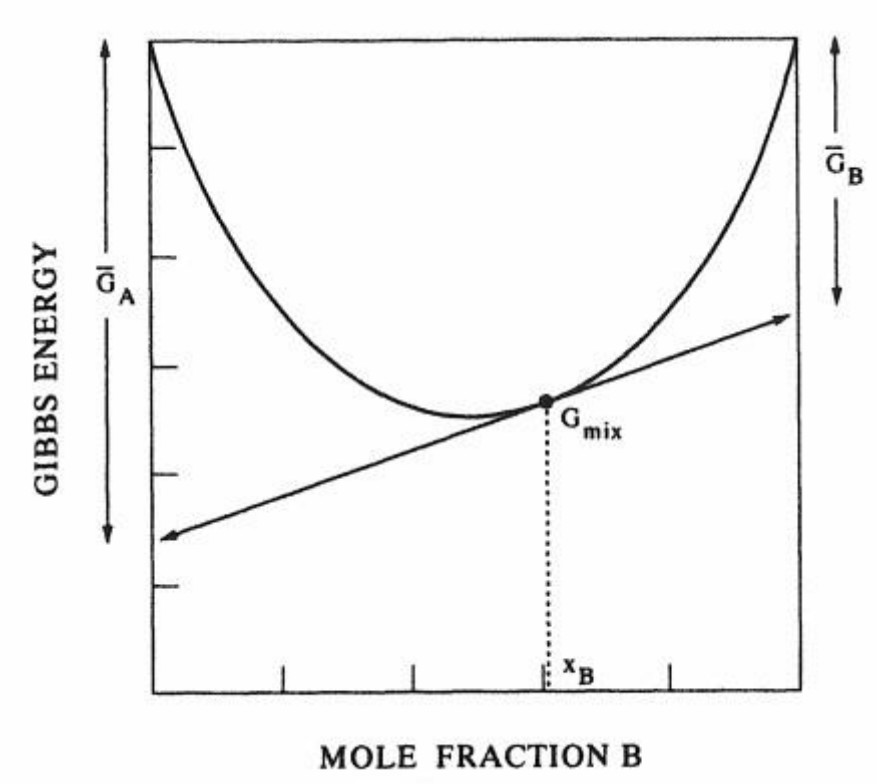

Figure 25 Influence of partial Gibbs energies (Saunders and Miodownik 1998).

The CALPHAD process uses these thermodynamic values to produce models for each phase, these models may be different but must produce the same results where two phases meet. While it is impractical to fully map a phase diagram experimentally, experimental results do establish specific conditions where phase changes occur, restricting the values of fitting parameters and helping ensure solutions are not only mathematically consistent but also match physical results. This mixed approach is shown effectively in a paper by Du et al (Du et al. 2008) where the Fe-Al-Si system is modelled, but several experiments are also used to confirm behaviour in key regions of the phase diagram.

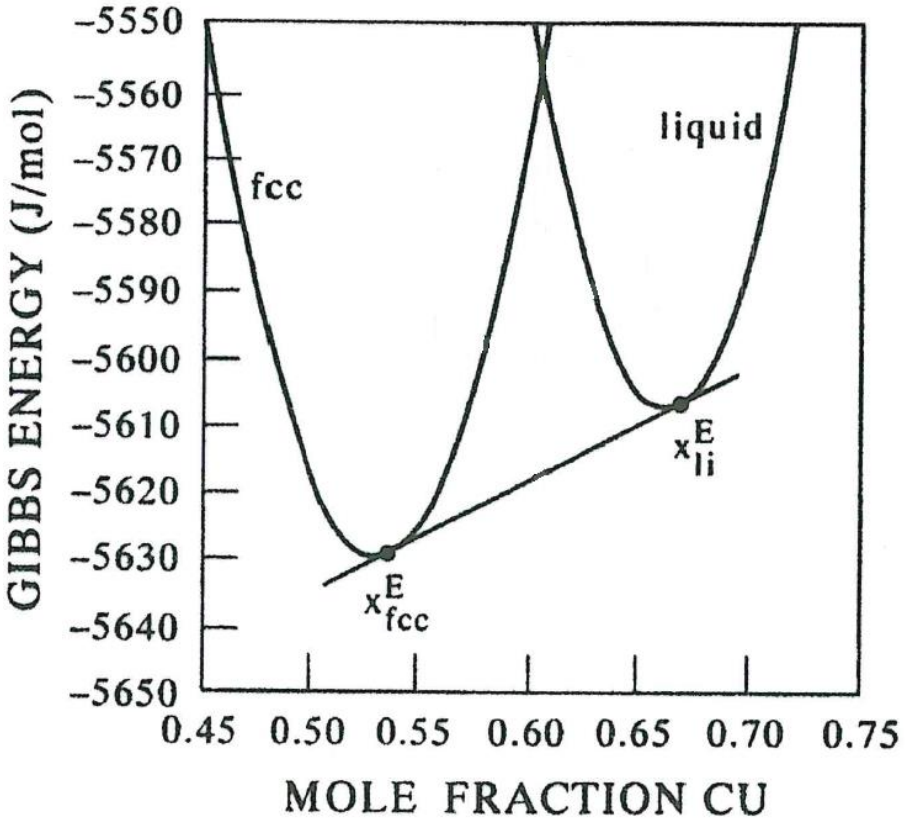

Figure 26 Gibbs energies varying with mole fraction in the Cu-Ni system, the line section betweenx^E_{fcc} and x^E_{li}indicates the region where a mix of phases has a lower Gibbs energy than either phase alone, so both phases exist simultaneously (Saunders and Miodownik 1998).

Calculating the Gibbs energies of different phases and therefore the stable phase for a wide range of points on the phase diagram then allows filling in the rest of the phase diagram, to a chosen level of accuracy. It is obviously possible to calculate a phase transition to an arbitrarily small fraction of a degree but this goes beyond practical necessity, and beyond the scale of error in the initial measurements this additional accuracy can not be reliable meaning that a sensible threshold is important for both efficiently allocating resources and ensuring accurate results. Optimisation algorithms minimise the number of points calculated far from phase transitions, allowing more computing time to go to providing a more detailed picture near boundaries. In theory as better models become available they will be rapidly adopted into databases, however since models of multi-phase regions are highly and unpredictably dependant on results for the pure phases, even small changes often require so many adjustments that a new database is required, making these improvements slow and difficult (Andersson et al. 2002). If done well this fixing of parameters and model generation will allow reliable extrapolation to novel compositions, however many databases start to generate unreliable results far from previously studied compositions so in these conditions

are often a general guide at best (Sundman, Jansson and Andersson 1985) (Chang et al. 2004), and an example relevant to this work is looked at when discussing Thermo-Calc specifically.
While this method focuses on equilibrium conditions and as such shows phases that are indefinitely stable for a specified range of conditions, some of these phases take a long time to form, so can be explicitly excluded in a pseudo-equilibrium approach. A more robust approach to non equilibrium conditions is to include kinetics in CALPHAD calculations in order to account for metastable states that can develop, (Baricco et al. 2004) an example in steels is the balance between carbon in solution and carbide formation, this is the idea behind software such as DICTRA.
DICTRA is an optional module within Thermo-Calc that focuses on computational kinetics, which is the simulation of diffusion controlled processes such as dendrite coarsening, carburisation and homogenisation(Andersson et al. 2002). This requires development and use of kinetic databases relating to atomic mobility in various phases, as well as the standard thermodynamic database used by Thermo-Calc (Software 2019). Dictra is currently only able to handle geometries that can be reduced to a single spatial variable, such as planar, cylindrical and spherical systems and relies on a similar approach of building databases(this time based on kinetics) to develop the models, but also including experimental data to ensure results are not merely internally consistent but also confirm to observations of physical systems (Borgenstam et al. 2000). This focus on diffusion controlled processes puts DICTRA beyond the practical parts of this work, but it is still a valuable tool in metals processing more broadly. The use of DICTRA for dendritic microsegregation is shown in (Zhang and Strangwood 2019)

2.11.2 COMSOL

A small part of this work also made use of the software COMSOL, COMSOL is an expansive software package that offers CAD to produce the geometry of interest as well as property databases for a wide range of materials which can be modified to better suit the simulation being run, and a wide range of physics simulations that allow it to simulate a wide range of processes using the finite element method. While not exploited in this work, the key feature is that multiple physics models can be used within the same simulation, hence the marketing as ‘multiphysics’. In the finite element method, first the geometry of the model is split into numerous elements, typically by applying a mesh to produce simple polygons in 2D or polyhedra in 3D. Then the equations for the unknown property are approximated by low order polynomials and solved over each of these elements, these results are then combined to cover the whole of the model (Pepper and Heinrich 2017). Due to the variety of physical phenomena that can be modelled discussing the specifics of each physics model is not suitable here. Similar work modelling the thermal gradients and cooling rates of a system has

been done in COMSOL such as Walinjkar et al (Walinjkar and Rao 2015). Summing over all elements can be formally written as

$$T(x) = \sum_{i=1}^{n+1} a_i \Phi_i(x)$$

Eqn 23

Where T(x) is the desired approximation to the temperature field, which must be consistent with the systems boundary conditions, a_i is an unknown parameter for an individual element and Φ_i is the shape function of each element. There are two common methods of formalising the next step, the Rayleigh-Ritz approach offers a more complete description, but is not possible in some complex problems while the Galerkin formulation can always be applied. After applying the approximation to the exact formulation of the system, there will be some error called the residual function and the weighted residuals method multiplies the residual of each element by a range of weighting function to eliminate the integrals of the residual function. Then a set of linear equations are generated and solved for a_i.

2.11.3 MICRESS

MICRESS is a commercial software package used widely to model solidification behaviour. MICRESS uses thermodynamic data from databases such as those in Thermo-Calc as well requiring input of specific data relevant to the situation being modelled. This includes tangible properties such as the size of the simulation and starting temperature, as well as the composition and a Thermo-Calc file detailing the thermodynamics of the relevant elements then also building on the thermodynamic data by including coefficients for diffusion and kinetics. It then uses multiphase-field theory to predict microstructure development by using the finite difference method allowing approximate solutions to be achieved through matrix algebra (Access-e.V. 2018a, Access-e.V. 2018b). The combination of the phase field approach with thermodynamic data from CALPHAD offers a lot of utility (Steinbach et al. 2007).

Phase field models consider the phases as fields and are a valuable approach due to readily available computation power to solve partial differential equations numerically. Sharp interface approaches, such as those put forward by Stefan, treat phase boundaries as 2d surfaces, with an area but no depth, meaning that there is a sharp and discontinuous change in properties from one phase to the other. In contrast phase field theory treats interfaces as diffuse, with properties intermittent between the two phases and a continuous change in properties (Bulent Biner 2017). There are broadly speaking two groups of parameters that need to be considered, conserved quantities such as composition where a change in one region must be matched by an equivalent and opposite

change elsewhere, and non-conserved quantities like magnetic spin alignment, these two categories require handling through different equations. The general forms are

$$\frac{\partial c}{\partial t} = \vec{\nabla} \cdot \left[M_c \boldsymbol{grad} \left(\frac{\partial F_T}{\partial c} \right) \right] \qquad \textit{Eqn 24}$$

For conserved parameters and

$$\frac{\partial \Phi}{\partial t} = -M_\Phi \frac{\partial F_T}{\partial \Phi} \qquad \textit{Eqn 25}$$

For parameters that are not conserved where t is time, T is temperature, c the conserved parameter, Φ the non conserved parameter, M is mobility and F is the Helmholtz free energy (Fultz 2014).

The multiphase field approach is then conceptually simple in that it adds additional fields, in order to allow for more complex simulations such as many components or including heat transfer, however simultaneously solving these equations is impractical analytically, requiring computer simulation to find numerical solutions. One issue with this approach is that it will produce planar interfaces, even when an interface should become unstable, this is easily resolved by adding a noise term to generate the small perturbations that grow into dendrites (2018).

The software MICRESS has specifically been used for a range of problems within metallic systems including a range of examples in a paper by Böttger et al which demonstrates the use of MICRESS for a range of applications such as solidification, solid state phase transformations and diffusion. Notably however, this paper does not compare these results to physical experiments, leaving open the possibility that while the structural changes seen from adjusting the models are qualitatively the changes that would be expected, the exact values obtained may not be as accurate (Bottger et al. 2008). Other work by Pariser looked at the γ-α transition in several steel grades, with mixed results, some models matched well with experimental results, while others showed a consistent type of behaviour between experiment and model but with notable discrepancies in absolute values (Pariser et al. 2001).

2.12 Solidification Summary

The solidification of metallic alloys has a large variety of nuanced details that can have significant impacts on the structure developed. The solidification range of the material is based on its composition - a narrow range will tend to produce large grains, while a wide range produces smaller grains. Faster cooling rates also tend to reduce the grain size of the material, as well as the spacing of dendritic structures, if any are present. At extremes, cooling rate can change the solidification

morphology entirely - a very low rate will lead to a stable planar interface. Rates generally found in industrial settings produce a dendritic interface, and if cooling can be made extreme enough, then equiaxed nucleation can be triggered throughout the whole material. Nucleation can be further encouraged by adding inoculation particles to the molten metal, with smaller particles less likely to influence the materials properties, although the extreme temperatures involved make this more difficult for steel than for other materials. During solidification, any dendritic structures that are still surrounded by the liquid phase will have a gradually coarsening structure to minimise surface area between the phases, and arms may break off, flow to other regions, and then act as nucleation sites for new grains. The cooling rate also influences the level of segregation seen between different regions of the material, and these patterns of segregation not only influence properties in their own right, but also influence the density of precipitates that form from one region to another. However, even after solidification, prolonged times at elevated temperatures tend to lead to further changes in the material - grain size, segregation, and precipitation can all be affected. The development of modern computing has led to the development of a range of software that use techniques too cumbersome to perform by hand in order to simulate various aspects of phase transformations. Thermo-Calc makes use of thermodynamic data to and the CALPHAD methodology to map phase diagrams and MICRESS build on this to simulate microstructure development using phase field theory.

2.13 Gaps in current knowledge

Due to the previous difficulty in casting high Al steels, research on these grades has been very limited, until recently with the development of new casting techniques that may allow for the mass production of these grades. Thus while these grades offer benefits such as a lower density which is of value in producing more fuel efficient vehicles much work needs to be done to develop these grades for industrial use.

This work also identified a gap in the literature concerning how grains grow and compete through the columnar zone, an improved understanding of solidification behaviours is important for two reasons. First the grades that are looked at are fully ferritic, meaning the solidification structure will persist down to room temperature. Second, these new casting techniques greatly reduce the need for secondary processing, while also producing sheets that are mostly, or in some cases entirely made up of the chill and columnar zones, making the properties of the final product especially dependant on the cast microstructure.

3 Aims and objectives

3.1 Aims

This work aims to study the solidification structure of high Al steels at both the dendritic and intergranular levels in order to better understand the solidification process. As well as providing information that will lead to a viable production route for these grades. Particular attention will be paid to grain development through the columnar zone, since this has been identified as a region that is both understudied and of increasing importance based on current and expected near future developments in the continuous casting of steels.

3.2 Objectives

Developing a CLSM based methodology to characterise solidification structures under conditions similar to that during continuous casting.

Use the experimental casting at a range of cooling rate to assess the grain competition in these grades. EBSD will be used to allow assessment in terms of the number/size of the cast grains, as well as the rate at which they outcompete each other.

These experimental results will then help to develop a MICRESS model that can then be more broadly applied to other grades.

4 Method

4.1 Material compositions

As the focus of this research is on the development of the as cast microstructure and the influence of cooling rate and composition the majority of the work has been done using steels that do not have a bulk solid state transformation allowing the as-cast structure to be observed. The LDS grades used and their compositions are shown in *Table 7*.

4.1.1 High Al

The three high Al steels used all have similar compositions, as shown in *Table 7* one bake hardenable grade(BH) and two nano precipitate hardened grades (Nano 1/N1 and Nano 2/N2) , and the high amount of aluminium relative to all other alloying elements means that they are ferrite throughout solidification and cooling, with no solid state phase changes. This lack of phase changes is one major factor that makes these steels difficult to work with as no grain size refinement from transformation occurs. The high Al steels were supplied in the form of130mm long sections from as-cast ingots (ingot size 95 X 75) and samples were taken from both the surface at the centre of the longest face and mid-point in order to characterise the as cast structure, characterisation methods are summarised later.

Thermo-Calc modelling of the high Al steels showed there was very little difference in behaviour for the Nano grades, summarised in *Table 11*. However there was a more pronounced difference in solidification behaviour between the BH and the Nano grades, namely that it solidifies over a much narrower temperature range (5K opposed to 40K using the Lever simulations (equation 7) and 18K against 52K in Scheil simulations (equation 8)). In the Nano grades both the solidification profile and the segregation profiles for the various elements were virtually identical, with the single most notable variation being Mo (which is 10 times more abundant in N2 than N1 and segregated from 0.15-0.6 and 0.015-0.055 respectively).

Table 7 Composition of high Al samples (wt %)

Sample	C	Si	Mn	P	S	Cr	Mo	Al	N	Nb	Ti
BH	0.0048	0.06	0.54	0.002	0.0005	0.58	0.01	6.98	0.0011	0.017	0.01
N1	0.059	0.07	0.57	0.003	0.0007	0.52	0.02	7.12	0.0011	0.003	0.10
N2	0.059	0.07	0.56	0.002	0.0006	0.51	0.21	7.03	0.0012	0.002	0.10

4.1.2 TWIP steels

These grades were used to test the predictions made by the MICRESS model, these grades are fully austenitic throughout the entire temperature range and have solidification ranges of 74K and 132K respectively. The compositions of the material used is given in *Table 8*.

Table 8 Composition of the TWIP grades

Sample	C	Si	Al	Mn	Solidification range (K)
TWIP14	0.6	2.5	1.5	14	74
TWIP21	0.3	3	9	21	132

4.2 Sample Preparation

Samples for optical / SEM analysis were cut from ingots, and the size of the ingots determined the cooling rate, the larger ingots as received from IJmuiden cooled at around 0.6K/s, the 15mm thick in house casts at 10K/s and the 5mm thick in house casts at around 150K/s. They were then cut to size using an abrasive blade precision circular saw, then mounted in Bakelite (sample name was engraved on the back of the mount), followed by grinding on SiC paper then polishing with 9µm and 3µm diamond suspensions before a final polish of 0.5µm alumina. An additional step using colloidal silica was used for samples undergoing EBSD (with rinsing/cleaning between each stage). The approach was based on the procedure recommended for most steels in the Buehler materials preparation guide (2011). Once polished, the samples undergoing optical analysis were etched. Due to the high Al and low C content of the high Al steels, many etchants typically used on ferritic steels were ineffective. So a variety of etchants were tested, both those recommended for steels and those recommended for aluminium alloys, a summary of the effects of each is shown in *Table 9*. Initially optical analysis of samples was done using standard light field techniques with additional optical microscopy with polarised light being used to give improved grain boundary visibility. Samples for SEM use were re-polished after optical analysis before being attached to an SEM stub with silver paint. SEM characterisation was carried out in a Sigma FEG and most EBSD was performed on the same machine, with the last few upgrading to a JSM-7800F which provided faster scans over larger areas

Sample naming typically follows the convention of (material)_(cooling rate)_(test number), for example N2_50_4 would be the 4th test using the nano 2 material and cooled at 50K/s.

Table 9 Effects of various etchants on the high aluminium steels being studied.

Etchant	Intended use	Effect on high Al samples	Suitable
Nital, various concentrations	Fe	No effect after several minutes.	No
Picric acid + surfactant	Fe	No effect after 10 minutes at 323K.	No
Barker's regent (Diluted fluoroboric acid, electrolytic)	Al	Corrosion of surface, dendrites visible in places but no differential colouring between grains, large regions of excessive corrosion. Etching time ≈10s. Results are too patchy to be of use.	No
Kallings II (ethanol, HCl, $CuCl_2$)	Fe	Grain boundaries or dendritic structure revealed dependant on sample. Some shading of grains, difficult to obtain uniform results. Etching time <10s.	Yes
Keller's (water, HCl, HNO_3, HF)	Al	Grain boundaries or dendritic structure revealed dependant on sample. Prone to significant pitting, minor shading between grains. Etching time <10s.	Maybe
Graff's and Sargent (water, HNO_3, CrO_3, HF)	Al	Grain boundaries or dendritic structure revealed dependant on sample. Most samples show a speckled effect through grains, sometimes preferentially following the dendritic structure. Etching time <10s.	Yes

4.3 CLSM

Solidification trials were also carried out using a confocal scanning laser microscope (CLSM). The setup consisted of a highly reflective gold coated ellipsoidal chamber with a bulb at one focal point and the sample at the other focal point, the sample is then heated by radiation from the bulb, as shown in *Figure 27*. The system makes use of a 405nm laser, having the photo detection equipment only sensitive to a single, short, wavelength minimises issues of black body radiation overwhelming the laser and maintains visibility to above the melting point of steel. The confocal aspect refers to another part of the optical system, after bouncing off the sample the light passes through a pinhole before reaching the detector, ensuring that light outside the focal plane is almost completely excluded and allowing a relatively narrow field of focus.

The sample (typical size of 5X5X5mm) is placed in a crucible, which is then placed on the stand and the chamber is sealed. The chamber is evacuated then refilled with high purity argon 3 times, then a steady stream of argon is applied to maintain a positive argon pressure in the chamber, with an additional oxygen/moisture scrubber being used for the final fill and constant stream. The gas enters through a hole level with the crucible and leaves through a hole near the bulb. The pre-programed heating and cooling cycle is started.

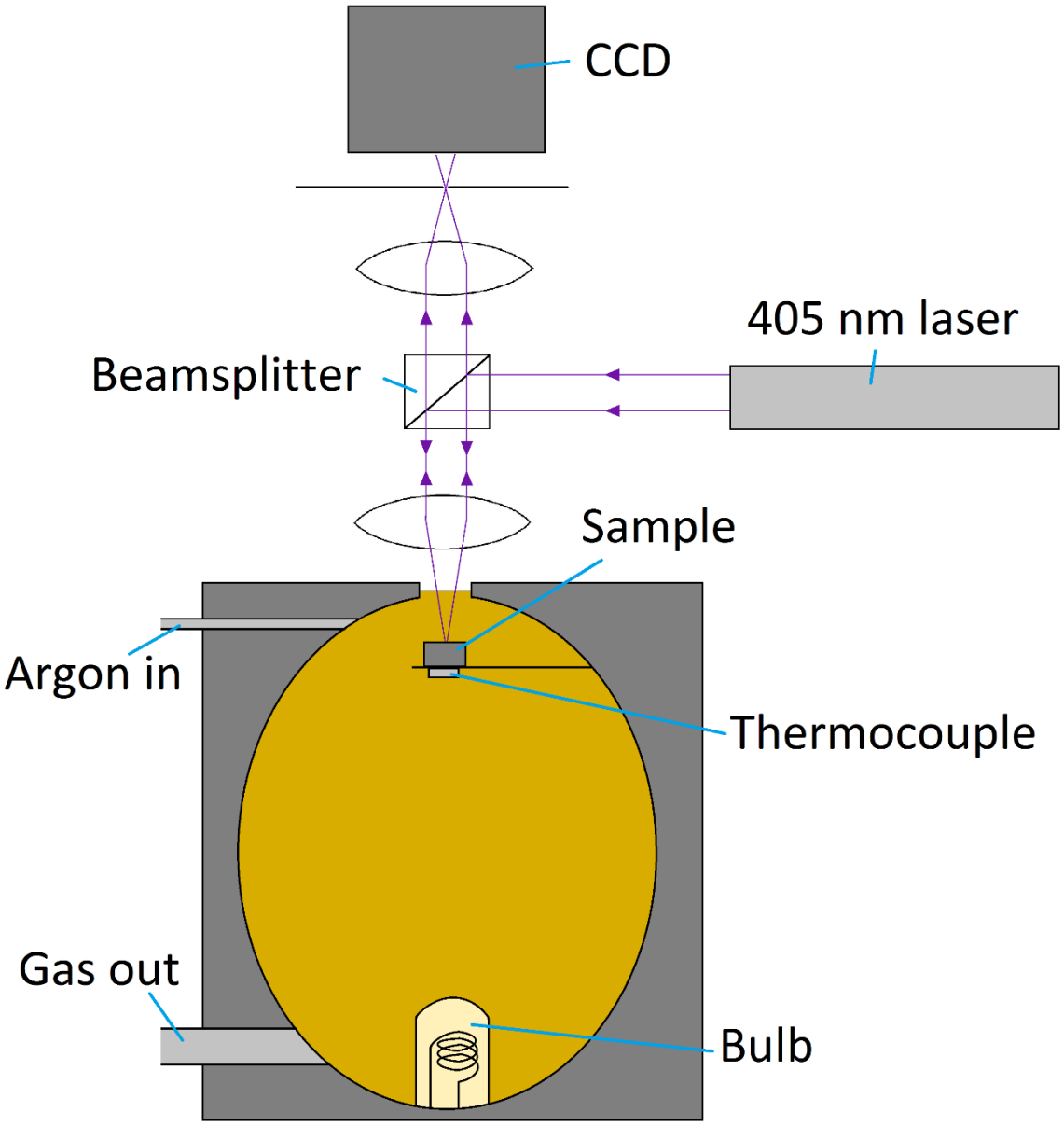

Figure 27 Diagram of the confocal experimental setup.

The sample is observed through the microscope until it melts, a diagram of how dendrites typically present is shown in Figure 28, occasionally a primary dendrite would be visible growing along the surface providing a complete cross section, but usually only a set of secondary arms reaching the surface are visible. If the temperature plateaus without the sample fully melting then the temperature can be manually adjusted to find the melting point. However upon resuming the preprogrammed heating and cooling cycle the temperature will rapidly snap back to the programmed temperature, this limits control of initial cooling so it is only of use in finding the liquidus point in order to fine tune the program for repeats of the same material. In theory Thermo-Calc models can predict when melting will occur and be used to set the heating and cooling cycle, however both the inaccuracies in Thermo-Calc predictions for novel steel grades and the condition

of the equipment on a given day can cause some variation in the accuracy of temperatures recorded by the thermocouple. Even under ideal conditions these materials tend to melt when the thermocouple reading is around 3% over the expected liquidus point based on Thermo-Calc predictions, further variation was minimised by ensuring proper equipment maintenance. But the first sample of each day of testing was also used for fine scale calibration to ensure the peak temperature was just above the liquidus, potentially resulting in adjusting the target temperature by several degrees for further tests and resulting in discarding the results from the first sample. Since the parameter under investigation is cooling rate and not absolute temperature, ensuring the sample was just above its liquidus and then the cooling rate was controlled was sufficient and detailed assessment of the peak temperature was not required.

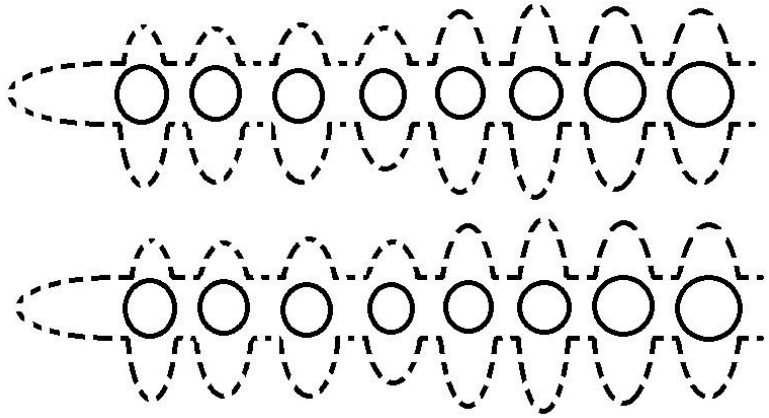

Figure 28 Diagram of dendrites visible in the CLSM, typically the main body is obscured under the liquid (dotted lines), while the secondary arms are visible where they reach the surface.

Once a stable liquid droplet is formed the heating is switched off (or power reduced) to allow controlled cooling; the maximum cooling rate is achieved for zero heating and was found to be approximately 40 K/s. The surface of the droplet is recorded giving direct observation of solidification.

The program used for the high Al steels (*Figure 29*) is shown in *Table 10,* heating and cooling rates at lower temperatures are intended to prolong bulb life and complete experiments in a relatively short timeframe as well as preventing excessive discrepancies between measured and target temperatures. While heating and cooling are both strictly controlled, the small visual area and narrow field of focus can lead to variations in the time taken to focus on the top of the droplet once it has melted. Step 6 is the experimental step and so is the only stage that differs between experiments. At higher cooling rates the cooling rate is maintained far below the solidus line in order to maintain the high cooling rate which can otherwise be difficult due to the slight feedback delay inherent in this equipment.

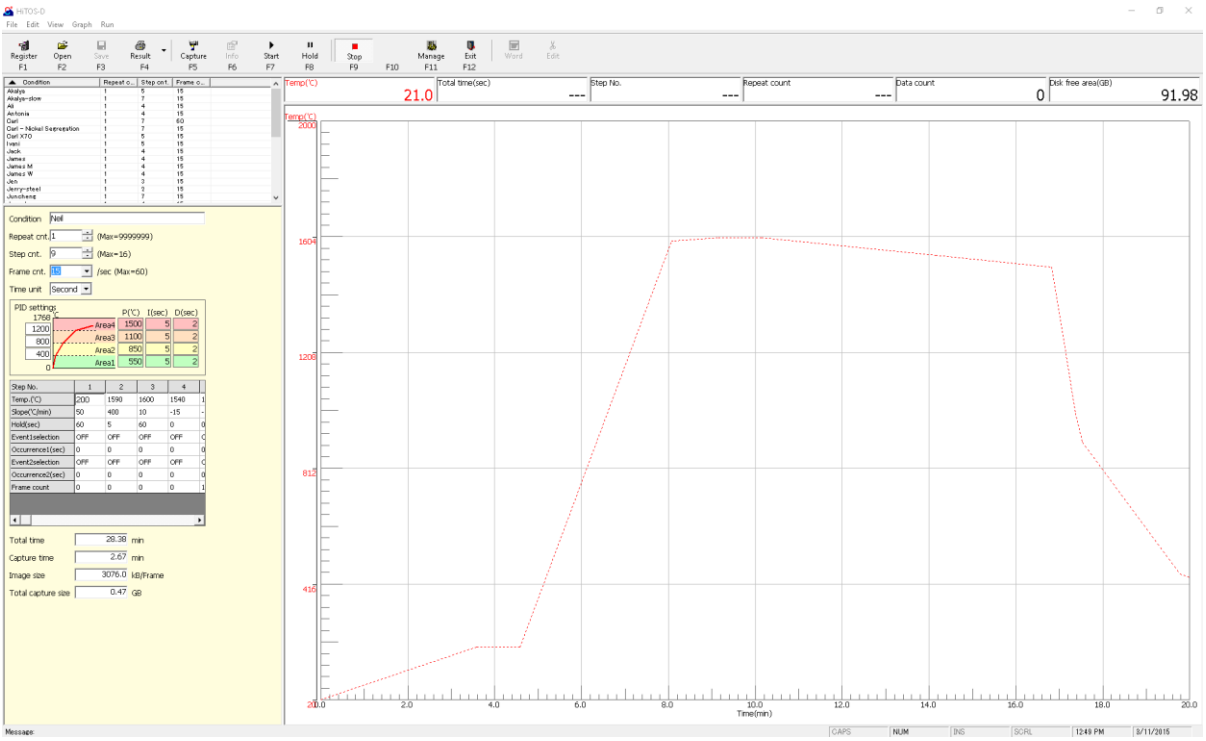

Figure 29 Interface for controlling and monitoring heating and cooling in the CLSM

Table 10 CLSM heating and cooling cycle.

Step	T Gradient (K/s)	Target T (K)		Step	T Gradient (K/s)	Target T (K)
1	$+\frac{5}{6}$/s	473		6a	-0.1/s	1803
2	$+6\frac{2}{3}$/s	1863		6b	-10/s	1373
3	Hold for 20 seconds			7	$-1\frac{2}{3}$/s	723
4	$+\frac{1}{6}$/s	1873		8	$-\frac{5}{6}$/s	293
5	Hold until focused on the top of the droplet					

Heat up to 200°C at 50°C/min, gentle heating at low temperatures extends the lifetime of the halogen bulb.

Heat to 1590°C at 400°C/min, then hold for 20 seconds to allow the conditions across the sample to become uniform.

Continue heating to 1600°C at 10°C/min then hold again, gently increasing the temperature high enough to fully melt the sample, holding at this stage both allows the system to become more homogeneous and allows the user to focus the microscope on the surface, which moves as the sample melts and changes shape.

Cool down past complete solidification at the required cooling rate, for 0.1K/s the target temperature was to around 1530°C, for 50K/s 1100°C was used.
Cool to 450°C at 100°C/min (faster cooling rate to minimise back diffusion) then to room temperature at 50°C/min, reducing cooling rate as the temperature lowers to prevent a large mismatch between measured and predicted temperatures, which can force a shutdown of the bulb and tends to reduce component lifetime.
The combination of small sample sizes and large grains in the solidified microstructure of the high Al steels (particularly as low cooling rate) made this approach unsuitable for work on comparing grain sizes, however it allowed clear observation of dendritic structures. It has been found that the absolute temperature measurement in the CLSM is inaccurate, the exact discrepancy depends on various factors such as the cleanliness of the chamber, but the reported temperatures tend to be in the range of 50-60K over the actual temperature close to the melting point of steel; this can make it difficult to predict when a steel should melt. However the error is systematic and therefore compensations can be made by simply increasing the target temperature and the knock-on effect of this is that the cooling rates achieved are around 3% higher than the target cooling rate, based on the observation that the room temperature measurement is accurate and the assumption that the deviation develops approximately linearly.

Some early work was done on a Gleeble thermomechanical tester, while these results were ultimately not suitable for this work, they did help develop other experimental methodology. The Gleeble relies on conductive heating so uses a soft conductive material between the sample and electrode, ordinarily graphite is used, but is too soluble in steel to be usable at such high temperatures so Ta foil was used in place of the graphite. It was noticed that initial CLSM samples only showed the grain structure when etched, but the Gleeble samples showed a dendritic structure, it was confirmed that Ta diffusing into the sample was responsible and then small amounts of Ta were added to CLSM samples in order to make bulk measurements. This doping was achieved by cutting a small piece out of one of these disks (weighed on a high precision scale to control final composition) and placing it in the crucible under the steel, ensuring that upon melting of the steel it was in contact with the Ta to allow for dissolution. These tests also held at the peak temperature longer in order to allow for dissolution and equal distribution of the Ta.

4.4 Induction furnace

To achieve larger samples for assessment of the effect of cooling rate on grain size during solidification a top-cast furnace that melts up to 1 kg material was used. Melting was carried out

under an argon atmosphere to reduce oxidation and the liquid steel was cast into small commercially available moulds. Two moulds were used, a small one (50x45x3.5mm) and a larger one (135x70x5.5mm). In addition spacers could be used between the two halves of the mould to increase the thickness, this was done for the 15mm thick sample. These spacers were simple steel strips placed down each side to give thicker sections.

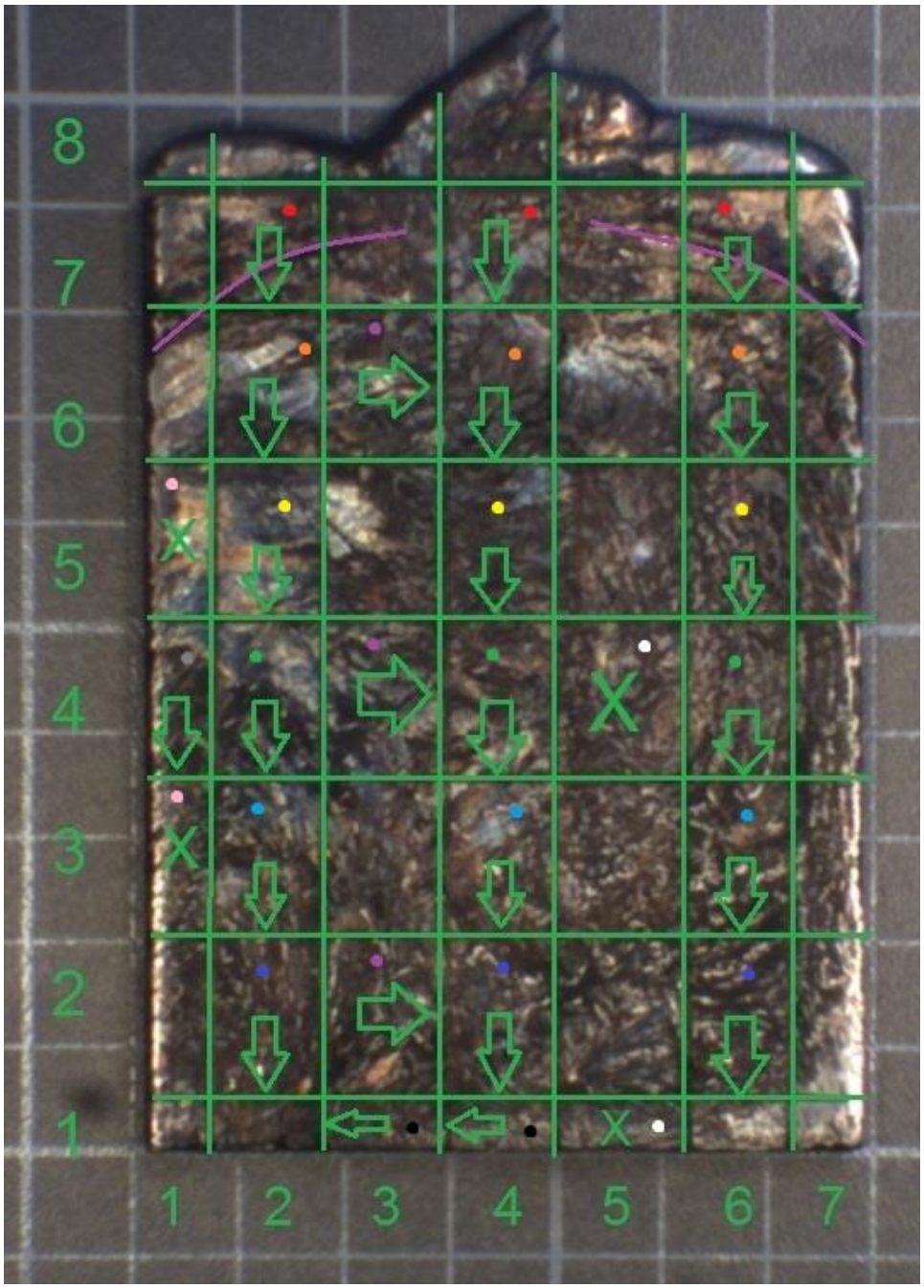

Figure 30 Details of a cast from the 135x70x5.5mm mould, background markings are 1cm apart. Green lines represent where the sample was sectioned, *the symbols indicate which parts of the material were mounted with the arrow pointing towards the surface observed and a cross indicating the plane of study was the plane of the image, each colour dot indicates a set of samples that were mounted together*.

The two moulds were able to hold approximately 50g and 300g as received, using a 1cm spacer triples the width of the larger mould and thus would triple the maximum capacity. Feedstock for

melting was cut into long cuboid pieces >300g (approx. dimensions 2x2x9cm) and melted in an induction furnace.

Figure 30 shows an example cast from the larger mould, complete with details of how it was sectioned and mounted. Symbols are in the parts that were mounted, arrows point towards the exposed surface and a cross indicating the plane of study was the plane of the image. Dots of the same colour indicate samples mounted together and the curved lines near the top highlight where surface wrinkles showed that the material was partially solidified during pouring. For the samples prepared in the plane of the image, grinding to remove 2mm was carried out to remove the chill zone and allow the columnar grain structure to be observed without reaching the centre line impingement. Results from an infra-red thermal imaging camera positioned above the mould during casting indicate a cooling rate of about 140K/s was achieved through solidification for standard air cooling. In the majority of tests the moulds were coated with a boron nitride spray to act as a lubricant and ensure easy removal of samples; a separate trial was also done with an uncoated steel mould surface to determine if there was an effect of different surfaces on solidification nucleation and subsequent grain growth.

4.5 Wedge Mould

A wedge mould was used so that the effect of varying cooling rate in a single cast could be examined. *Figure 31* shows the wedge mould design that was used. The wedge mould was produced by modifying one of the thin cast moulds to produce a sealed wedge shape, with an angle of about 11°. Other than the shape of the mould these casts were produced in the same way as the 5mm and 15mm thick casts produced in house. Care was required in analysis as when sectioning parallel to the top of the mould as only one half of the material will have a thermal gradient in line with the sectioned plane. It was found that turbulence when pouring affected the lower part of the solidified cast, which was observed in a non-uniform solidification structure, these areas were not considered in the final analysis.

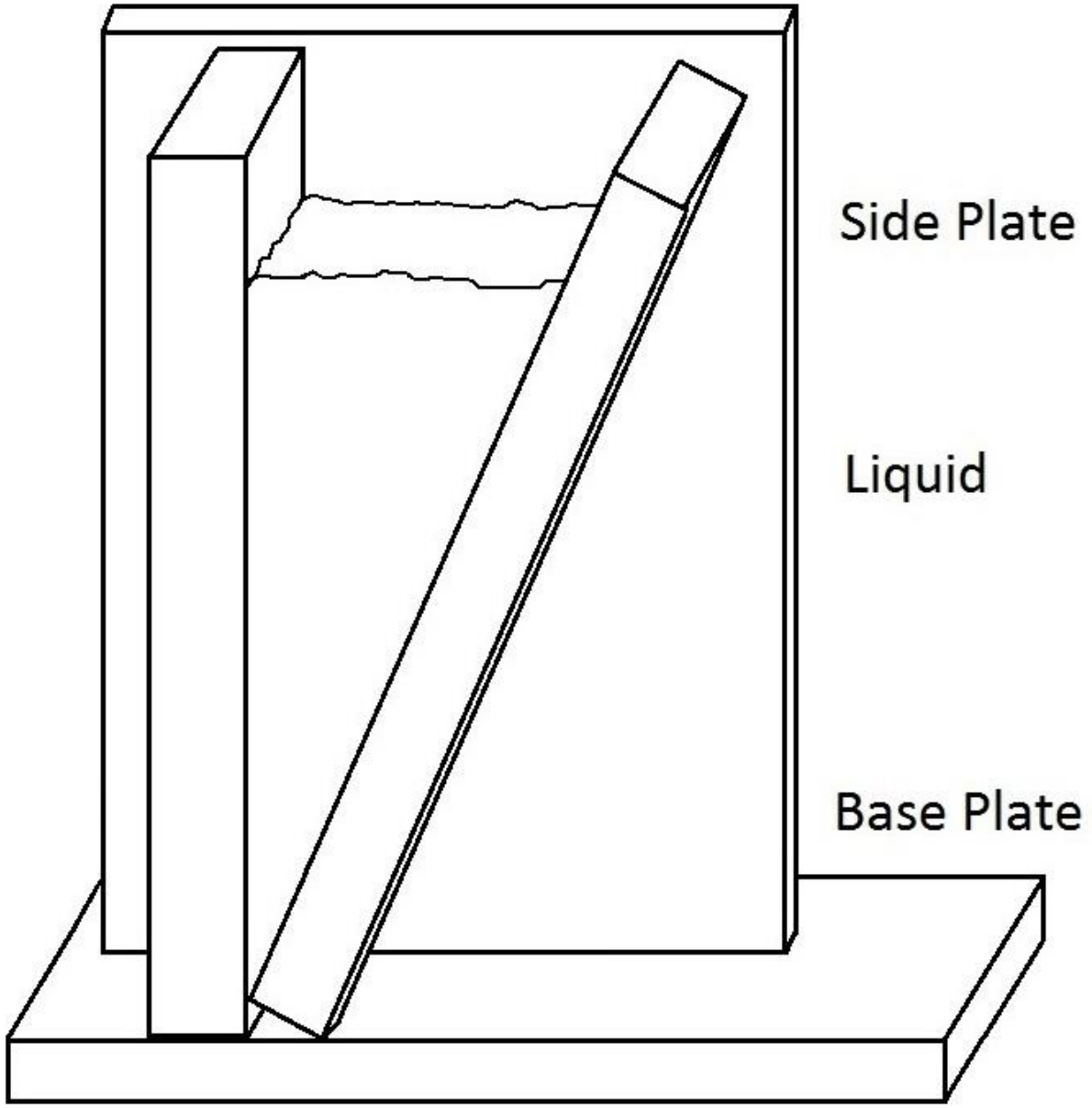

Figure 31 Final design of the wedge mould.

A simple model of the wedge system was developed in Comsol in order to assess the expected behaviour of the system. The model consisted of the liquid steel in the mould at around 1800K surrounded by the mould material, also steel but starting at around 290K. Since behaviour far from the side dams can be approximated to a 2D thermal transfer problem, that is how the model was set up. After constructing the geometry a material was chosen, a generic 304 steel was used since the thermal properties of differing grades change only slightly. Then the physics were set up, this was simply heat transfer, the mesh size was set and initial conditions set, room temperature for the mould and near the liquidus for the liquid. Figure 32 shows the geometry with the mesh overlay and the temperature distribution 2 seconds into cooling, clearly indicating the rapid initial cooling at the

tip and slower cooling towards the wider part of the wedge. The thermal gradient and cooling rate were both assessed where the wedge was 5 and 15mm wide, to match with the thicknesses of the smaller conventionally shaped casts. For cooling rate, the temperature was measured in each time step 2mm from the surface until it dropped more than 200K below the liquidus, then averaging the change in temperature over the time taken gives an average cooling rate. These were found to be approximately 150K/s at 5mm wide and 10K/s at 15mm wide, consistent with the cooling rates in the conventionally shaped casts. The thermal gradient was measured simply by dividing the difference in temperature between the centreline and surface by the distance between them, however this was done at different times for different heights. Since material near the bottom tip will solidify rapidly while the bulk material near the top will not have changed temperature at all, and by the time the top has a well developed gradient the bottom will be far past fully solidified. Thus there was some estimation of the best time to measure different heights to accurately represent cooling through solidification.

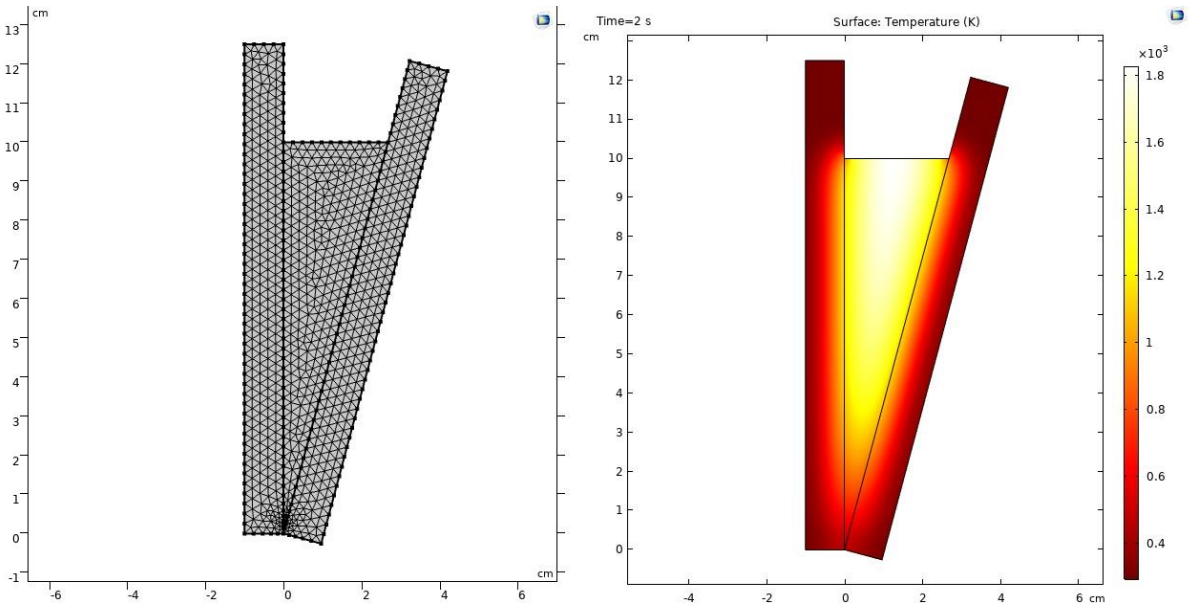

Figure 32 Mesh (left) and thermal profile after 2 seconds (right) of the COMSOL wedge model

4.6 EBDS and texture representation

EBSD was used to determine the grain size and texture of the solidified microstructures. The left of *Figure 33* shows a typical microstructure from the nano-1 steel, where the black lines represent grain boundaries over certain specified misorientation (5° thin and 15° thick). The colours represent the orientations of each region relative to a specified [100] orientation (throughout this work the growth direction is of interest so this is always parallel to the thermal gradient). With red being close to growth along the [100] thermal gradient, green is one of the <110> directions and blue is the <111> directions, other colours represent intermediate orientations. In the centre is a pole figure (PF),

which has a complete description of the orientations through the sample using spatial variation in orientation space. That is, changing position on the moving around the map indicates a change in orientation. This maps the grains according to their orientations and grain colours from the EBSD map can be preserved to improve readability. In this case red regions will be around <100> nodes, then green and blue will be around <110> and <111> families respectively. While a pole figure can be constructed around a 001, 101, or 111 axis, the 001 orientation is the most convenient reference frame, so the corresponding 001 visualisation is most coherent.

Figure 34 demonstrates constructing a pole figure, the projection is constructed from point N, which in this case is the orientation along the thermal gradient, then each pixel in the EBSD map is considered in turn, P is each point where the local structures <100> orientation passes through the lower hemisphere of the construction then the orientation is mapped to point P' in the pole figure, which exists in the x,y plane. Since the cubic system has 6 <100> directions, it is apparent that each pixel from the EBSD map must appear in the pole figure multiple times, regardless of orientation at least 3 of the pixels <100> directions will intersect with any given hemisphere. This means that while the pole figure offers a complete description of the orientations within a sample providing a more complete understanding than the EBSD map, there is an inherent level of redundancy which can clutter important information.

On the right is an inverse pole figure (IPF), this presents exactly the same orientation information as the EBSD map on the left and is functionally a condensed version of the pole figure, with all symmetrically equivalent orientations displayed as the same point. An important consideration is that since the EBSD map and IPF are relative to a specific orientation, rotation around that axis is not captured. So rotation around that axis will still appear red and near the <100> corner of the IPF but will spread out as a line through one of the <110> orientations and its corresponding $<1\bar{1}0>$ orientation. Since there is also some scatter from the ideal [100] growth direction, this appears as a band on the PF. These textures with a rotational symmetry are called fibre textures (Suwas and Ray 2014). It is additionally possible to present both pole figure and IPF data as contour plots, with the same shape but in this case the colouring shows the relative frequencies of grains at different orientations. A contour magnitude of 1 indicates that the proportion of grains at that orientation matches what would be expected from a random distribution, less than one, less grains than random and more than 1, more common than in a random distribution. Later in this work blue means under represented orientations and red orientations that are more common than expected, but the scale varied by plot since using a uniform scale would obscure detail in most contour plots. These are valuable because particularly when a single orientation becomes dominant the standard (I)PF is poorly equipped to show the relative abundance of different orientations since grains with the same

orientation will appear on top of each other and be indistinguishable, but the contour plot clearly accounts for the orientation at all points.

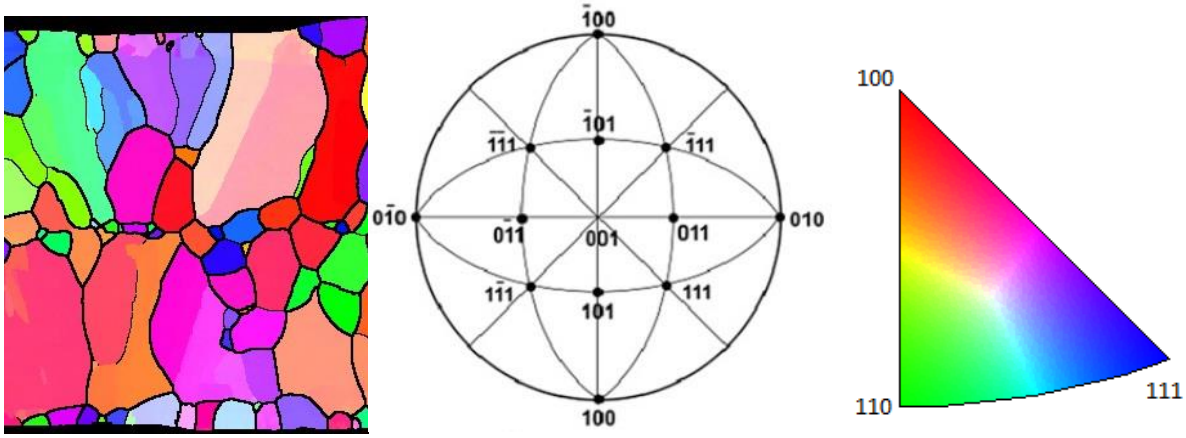

Figure 33 An EBSD map and a blank pole figure and inverse pole figure, the different methods used to present orientation data in this work

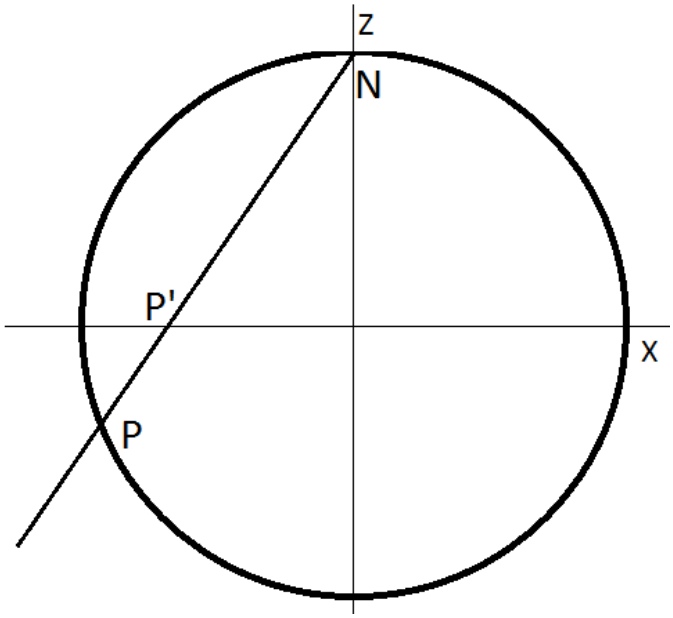

Figure 34 Construction of a Pole Figure, for each point in the EBDS map the grains 100 orientations in the lower hemisphere P are mapped to P', a pixel in the Pole figure.

4.7 Grain size measurement

Measurement of grain sizes was done using a line intercept method adapted for directional growth and orientation dependant structures. Drawing lines across samples perpendicular to the growth direction at the specified depths, for a single depth 3 lines close together are analysed and averaged to smooth sensitivity to grains being eliminated. The grains at either edge of the sample are excluded and the total distance is taken to be the distance between the furthest pair of grain

boundaries on the line, the number of grains is simply the number of distinct regions passed through. Where a more detailed assessment of each individual grain was used each grain was again measured 3 times around the target depth to smooth the effect of any discontinuous behaviour. For example in *Figure 35* the thick white line is the depth of interest, but the thin white lines are also analysed and the results averaged, and only the region within the blue lines is considered.

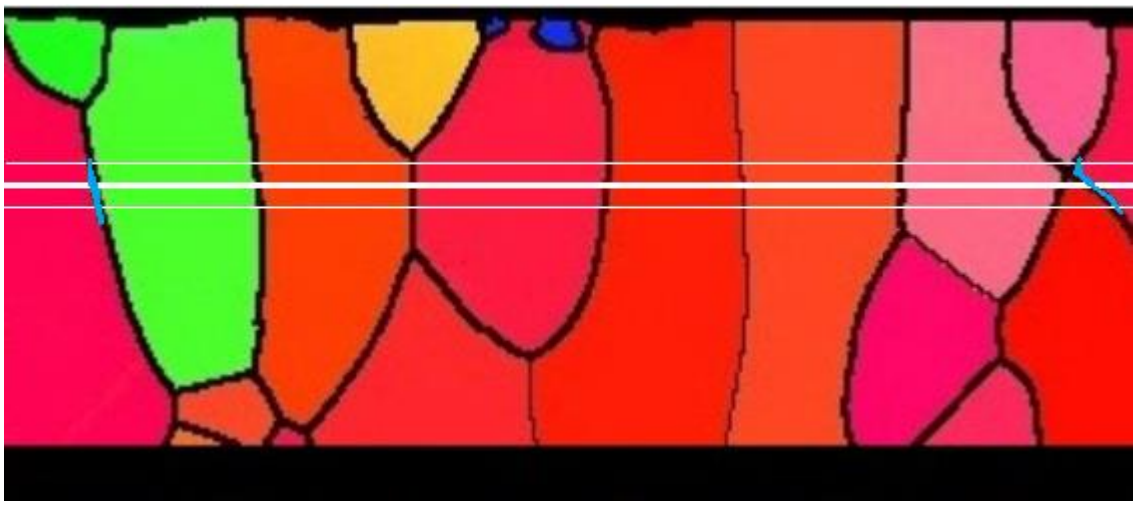

Figure 35 Grain measuring example

Figure 36 The distinction between grain width and low angle grain spacing.

Parts of this work rely on a distinction between grain width and low angle grain spacing, Figure 36 demonstrates this difference. This EBSD map shows the grains within the selected orientation range as greyscale, and grains outside the orientation range obscured with a green mask. Measuring along the purple line the total length is taken as the distance between the two red markers (x), all 6 numbered grains are completely within this region so the average width is x/6. But only grains 1, 2, 3, and 4 are within the low misorientation range sow the average low misorientation spacing is x/4.

Unless otherwise stated the errors in grain width/dendrite spacing and low angle grain spacing are the standard deviation from measuring each individual grain/dendrite space compared to the average for those conditions, while errors in misorientation are estimates accounting for the sample not being perfectly aligned as it is placed in the SEM and for tilt of the sectioning plane compared to the growth axis. Errors in depth are again estimated based on the precision of a ruler but also considering other factors such as surface loss to oxidation or not being visible due to curving of the edges that develops during polishing.

4.8 Dendrite measurement

Dendritic measurements were made by identifying multiple lengths where a large number of either primary or secondary dendrites were visible next to each other, measuring along this length and counting the spaces along that length. For a single condition a weighted average of these results was then taken. Obviously this means that many more secondary dendrites were measured than primary dendrites, so the data sets for SDAS will be more statistically significant.

Results

5.1 Thermo-Calc Modelling

Thermo-Calc was used to model the solidification behaviour assuming either the Lever rule or Scheil equation, both discussed in more detail in Section 2. The Lever rule assumes complete diffusion throughout both liquid and solid and as such assumes equilibrium cooling at an essentially infinitely slow cooling rate. While Scheil goes to the other extreme and assumes no diffusion at all in the solid phase, which requires essentially instantaneous solidification, however due to the mobility of C at high temperatures it is common to treat carbon as a fast diffuser even when using the Scheil equation for other elements, this practice was also applied in this work. Typically the Lever rule is considered reasonably accurate up to cooling rates of about 1K/s while the Scheil equation is considered reliable at cooling rates down to about 100K/s but the experimental part of this work includes the range between these two extremes, where neither model is particularly reliable. For most materials the discrepancy between Lever and Scheil is most noticeable when comparing solidification ranges. While both models predict solidification starting at the same temperature, Scheil consistently predicts solidification occurring over a larger temperature range than that predicted by the Lever rule. The Thermo-Calc predictions of solidus, liquidus and solidification ranges for various steels used in this work are shown in *Table 11*, for reasons discussed later, some samples were doped with a small amount of Ta, which had a small influence on the solidification range, the method of doping is discussed at the end of the CLSM section below. Although it is known that the models can deviate significantly from experimental results for highly novel steel grades, so these values may not be completely accurate (Presoly et al. 2012). *Figure 37* provides a graphical depiction of the difference between Lever and Scheil approaches in the Bake Hardenable steel, clearly showing that they start solidifying at the same temperature, but also that the difference in segregation causes a narrower mushy zone in the Lever simulation.

Table 11 Solidification ranges of steels based on Lever and Scheil models.

Steel Grade	Nano 1	Nano 1 Ta* estimated composition	Nano 2	Bake Hardenable	304
Lever solidification range (K)	1802-1762 40	1799-1769 30	1801-1761 40	1807-1802 5	1718-1663 55
Scheil Solidification range (K)	1802-1751 51	1799-1763 37	1801-1748 53	1807-1788 18	1718-1558 165

The 304 steel noticeably showed an even more substantial difference between simulations, with the Lever simulation predicting a large number of phases developing during cooling, resulting in a multi-phase predominantly ferrite structure at room temperature.

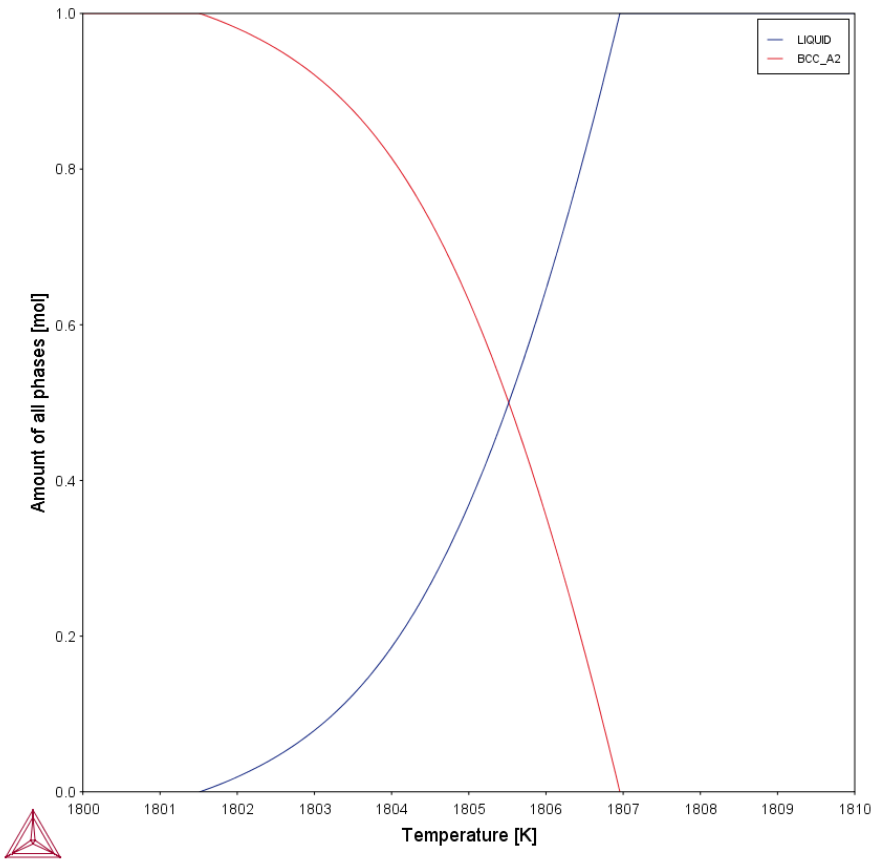

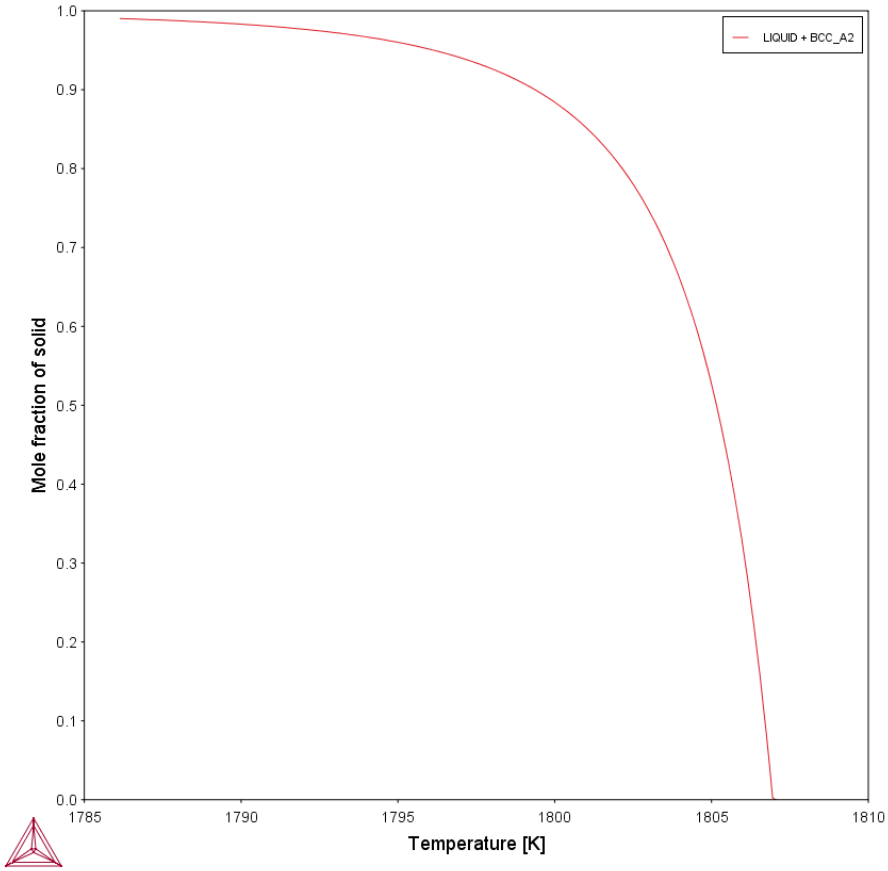

Figure 37 Solidification modelling of the BH steel using the Lever (top) and Scheil (bottom) equations.

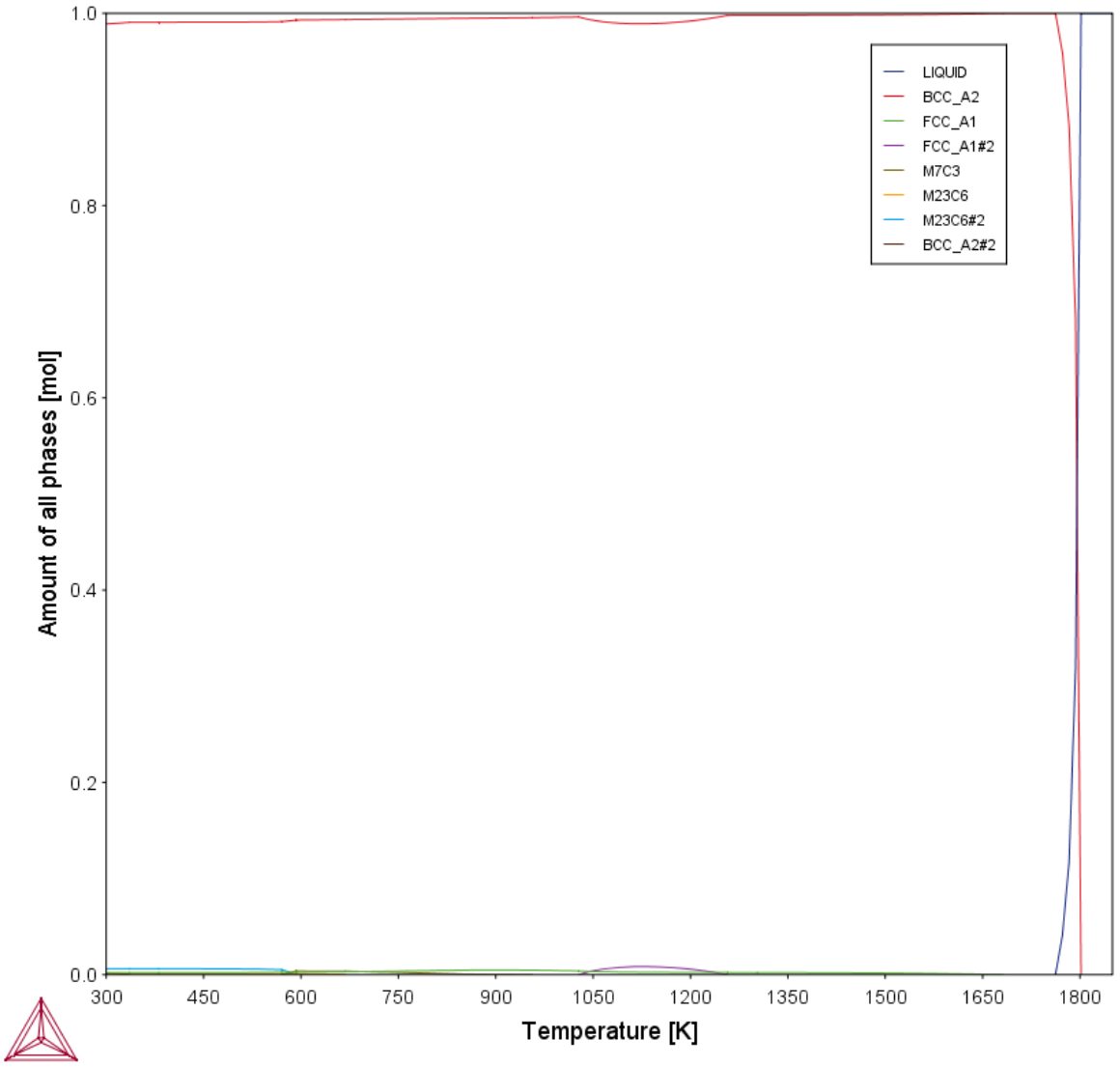

Figure 38 Property diagram of the 'Nano 1' steel, showing solidification occurring over a narrow range around 1800°K and small amounts of several phases developing through cooling.

Figure 38 shows the Lever simulation of phases that exist in the Nano 1 steel, showing that it solidifies as ferrite and then while several phases are predicted to develop during cooling under equilibrium conditions, the amounts are very low (never more than 5% combined) and are not expected during dynamic cooling. Table 12 shows the expected compositions due to segregation in the Nano 1 steel, calculated in Thermo-Calc from the first and last solid fractions, which assumes equilibrium conditions but no diffusion in the solid. Whilst these values will represent an extreme value, unlikely in practice, they are useful in placing boundaries on the expected behaviours and determining which elements to focus on to map segregation using EDX. Manganese appears to give the best combination of absolute value and proportion change, however titanium and aluminium segregation may also be detectable. While iron has the largest absolute difference in value, the

difference is quite small as a proportion of the values themselves making distinguishing between the regions difficult. And at the other extreme, carbon has the largest proportional difference but its absolute values are so low that gathering enough data for reliable results. From the Scheil solidification simulation for this material (*Figure 39*) it can be seen that in the final stages of solidification a new phase develops: titanium carbide.

Table 12 Expected segregation profile of the Nano 1 steel using Scheil calculations in Thermo-Calc.

Element	Fe	C	Al	Mn	Cr	Ti
Initial Solid (taken at 1.5% fraction solidified)(wt%)	92.0	0.008	6.74	0.38	0.44	0.062
Final Solid (taken at 98.5% fraction solidified wt%)	87.5	0.53	8.06	2.23	0.95	0.73
Peak (if at another point)	-	-	-	-	-	0.85 (at 3.6% liquid)

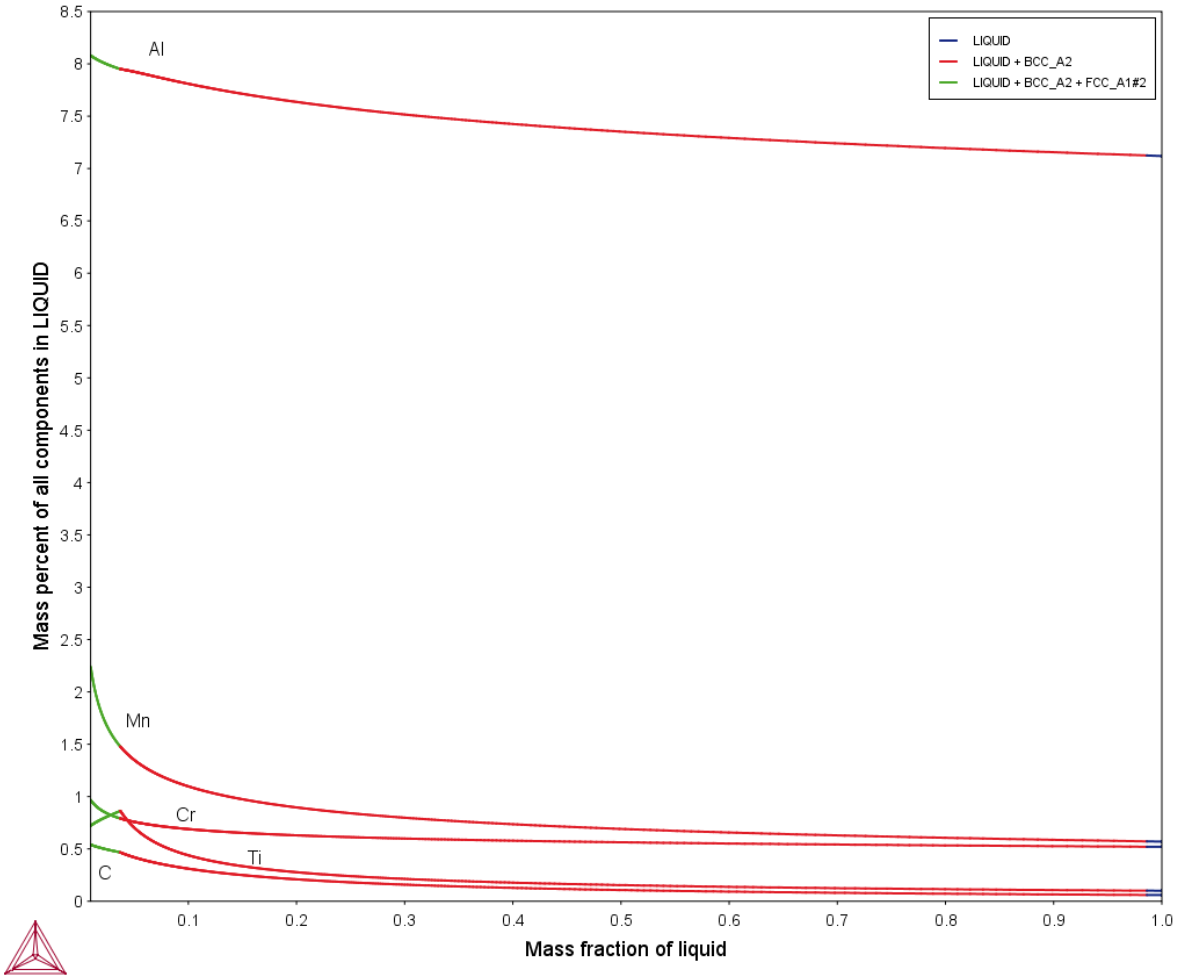

Figure 39 Segregation profiles of alloying elements in the Nano 1 steel.

5.2 Grain Size and Competition

Due to the strong dependence of mechanical properties on grain size, this section looks at the impact increasing solidification rate (as seen in near net shape casting) has on the grain size. As mentioned in an earlier chapter, post nucleation then the dominating mechanism for grain size control is grain competition. The extent and speed to which grains compete will dictate the cast grain size for the material (which strongly dictates the processability of these grades) as well as the texture (which may or not be favourable depending on the application of the steel).

For this section the Nano and BH LDS grades where used due to their single phase nature, range of mushy zone widths (see Methodology), and well as the inherent problems with currently processing these grades.

5.2.1 Cast Analysis

Figure 40 shows the grain structure across various regions of the first mould casting with optical images above and processed images better highlighting the grain structure below. With annotation, lines indicate cuts that were made, arrows indicate the face that was mounted to observe with a "X" indicating the plane of the image, and the coloured dots track which samples were mounted in the same piece of Bakelite. 4-1 clearly shows the multi directional solidification expected near the edges of the sample. 4-3 and 5-4 each show the directional solidification observed throughout the bulk, at different orientations and 6-6 shows the columnar structure breaking down near the top when a significant degree of solidification was occurring as the material was being poured. Figure 41 provides a bit more information about the grain structure, showing that the grain width was consistently about 200-300μm throughout the bulk region, except for row 2 which had a larger columnar grain width (approx. 400μm), suggesting that the extra cooling from the bottom is still influencing the structure.

This analysis has therefore shown that all subsequent analysis needs to be taken from above row 2 and between columns 2 and 6. This method has been used to assess both the BH and N1 LDS grades in 5 and 15mm thicknesses. Due to the difference in thickness and the difference in thermal reservoir it produces, then a different cooling rate is produced. These cooling rates are 150K/s and 10K/s for the 5 and 15mm cast respectively.

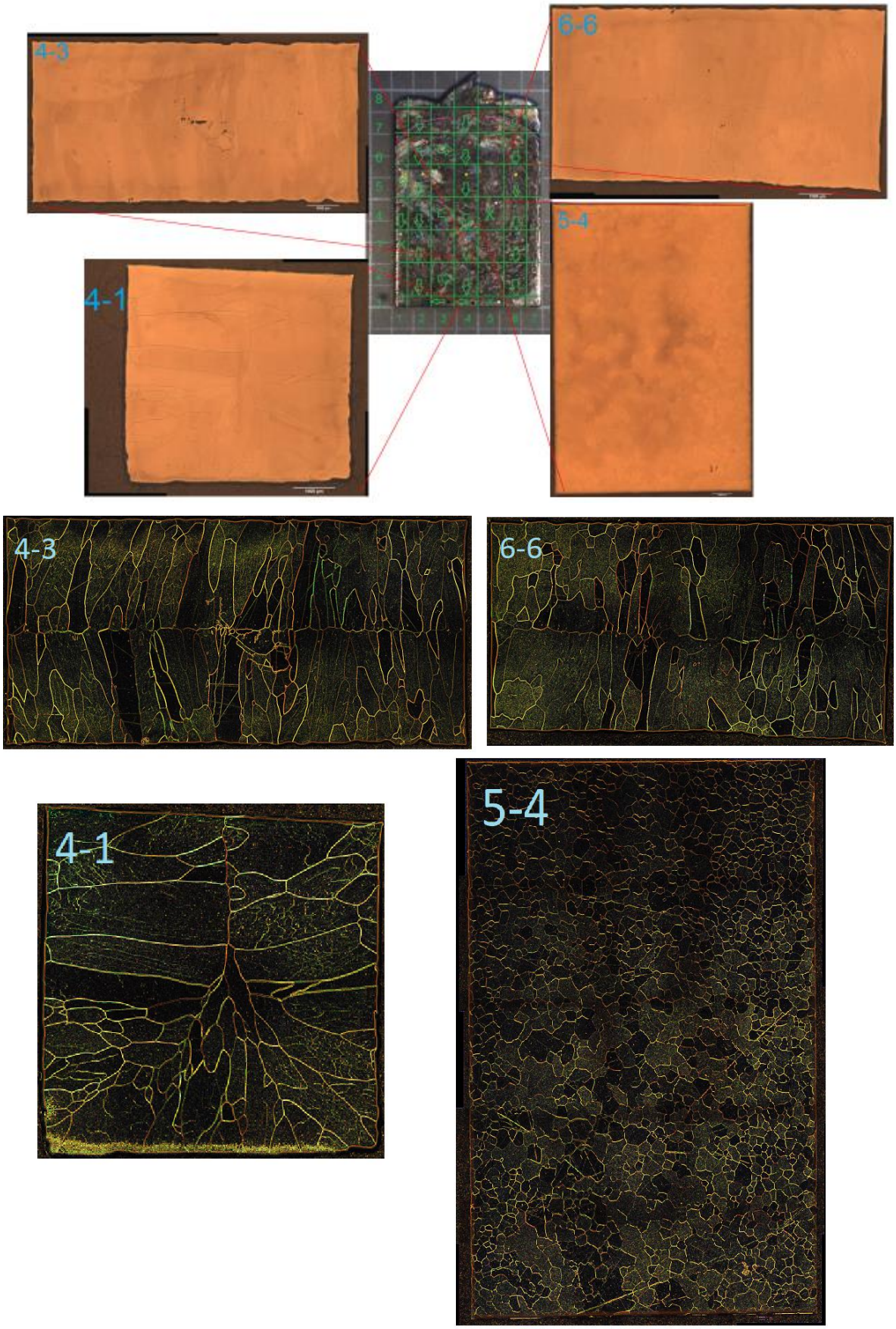

Figure 40 Grain structure at select regions throughout the first N1 casting optical (above) and processed (below)

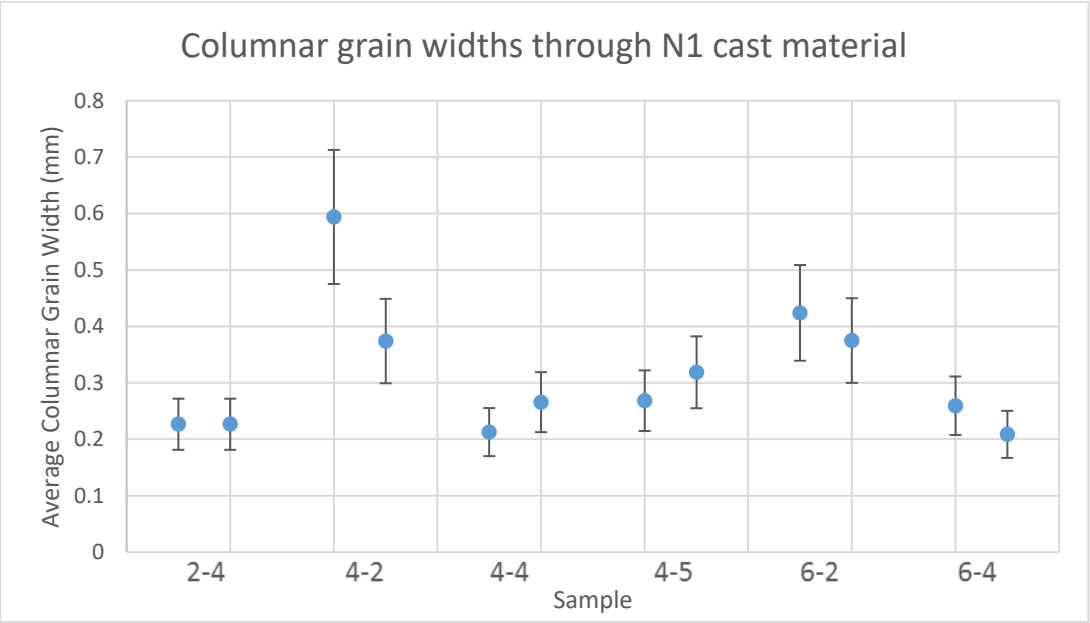

Figure 41 Columnar grain width through mould casting. 2-2 was excluded because impurities in the dendritic region had a significant impact on its structure.

This technique has the benefit of being quite adaptable, with the potential to adapt a variety of parameters; one cast was made to assess the impact of the boronitride coating on the grain structure. This produced a sample with equal sized grains to the coated mould, but also caused damage to the mould upon first contact with the liquid, partially melting it. Additional 5mm casts were made of the Nano 2 and BH grades, checking that the behaviour was consistent with what was seen in the received ingots. Results were consistent, both nano grades were very similar to each other and the BH grade had significantly larger grains. And a 15mm thick Nano 1 cast was also produced, this lowered the cooling rate, leading to larger structures, more detail is given later in this chapter.

5.2.2 EBSD

Using EBSD allows a much more precise assessment of grain sizes by eliminating the variation in etching responses and interpretation of how distinct a boundary must be to include. In deciding on the settings to use, grain boundaries were decided to be a local misorientation of >5° since this gave results that matched well with optical observations, allowing comparison between the two methods as necessary.

5.2.3 N1 Ingot

Figure 42 shows sections taken a regular intervals from the surface to a near centre region of the N1 ingot used throughout this work, the deepest part visible is 28mm from the surface. The surface micrograph clearly shows a surface chill zone followed by the development of a columnar zone while the deepest section shows the end of the columnar zone, with several equiaxed grains visible on the lower edge.

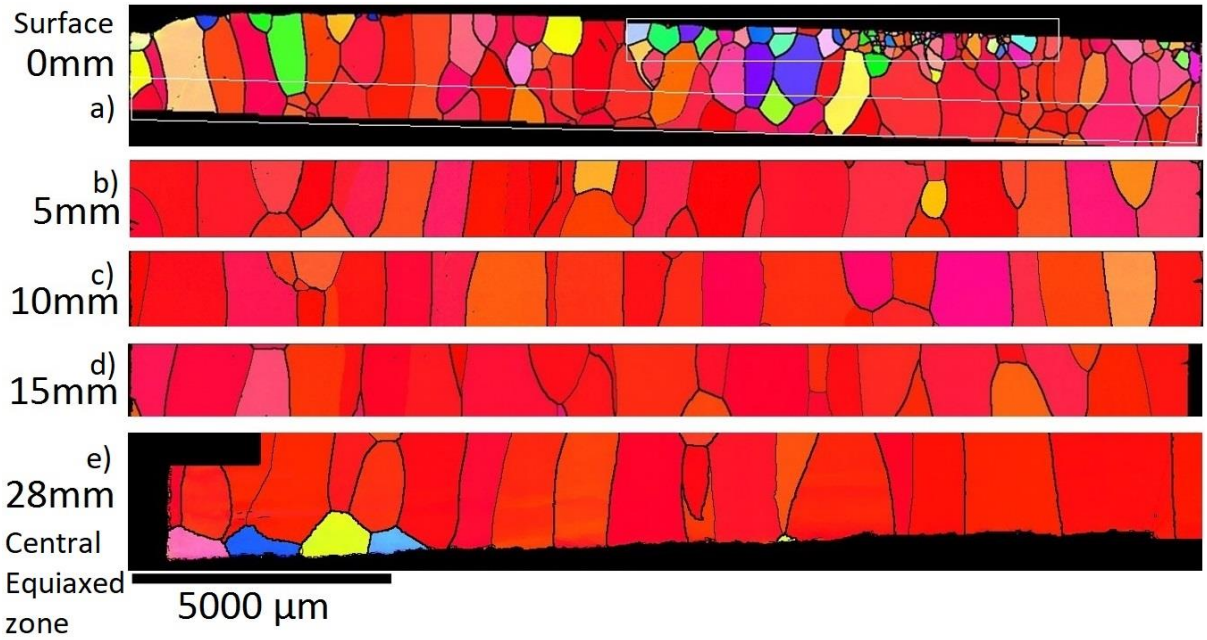

Figure 42 EBSD images showing a) the chill/early dendritic (with white boxes indicating regions studied as chill and early columnar) region at the ingot surface b)-d) sections taken of the columnar zone at 5mm, 10mm, and 15mm, from the surface and e) late dendritic regions of the N1 ingot, the bottom is 28mm from the surface.

Figure 43 shows the misorientation of grains in the N1 ingot against all 3 axes and in three significant regions, the colours of each point correspond to the colours of grains in Figure 42. The chill region shows the expected even distribution with no significant preference for any orientation, then the columnar start and columnar end regions each have progressively more texture, since the grains that are oriented close to the thermal gradient grow ahead of other grains, eventually out competing them this is expected. Measured compared to the growth axis, only a small range of grains will survive, while measured against a perpendicular axis one rotational degree of freedom is eliminated restricting grains to the +/-45° range of a single rotation. Since the IPFs for each orientation ignore rotations around an axis, only factoring in tilts away from it, the growth direction (Z axis) shows a strong preference for the <100> direction with no distinction between different rotations around the axis, but any grains that significant tilts away from the Z axis tend to be eliminated as grains compete. While in each of the X and Y orientations, twisting around the Z axis is mapped, leading to scatter between <100> directions and <101> directions. Figure 44 presents the same information as

Figure 43 but as a graph, while this does lose information about the direction of misorientation, it does provide a scale to clarify the magnitudes. Along the X and Y orientations there is some reduction in scatter with depth, with the maximum angle dropping to near 45° as the <111> misorientations are eliminated, while Z shows a large low angle spike with all grains in the columnar end region being within 12° of the growth direction. An interesting feature here is that it becomes apparent that some grains are misoriented by >45°, this is essentially due to the additional degrees of freedom in a 3D environment. As a quick thought experiment, a circle on the face of a cube that is 45° from the central point along an axis perpendicular to the face will form a tangent to each edge, the internal region will be less than 45° away and the corners will be more than 45°, if this is repeated for all faces then the corners remain outside the <45° range for all faces. A slightly more rigorous approach is included in Appendix 2, a full discussion can be found in (Mackenzie 1958).

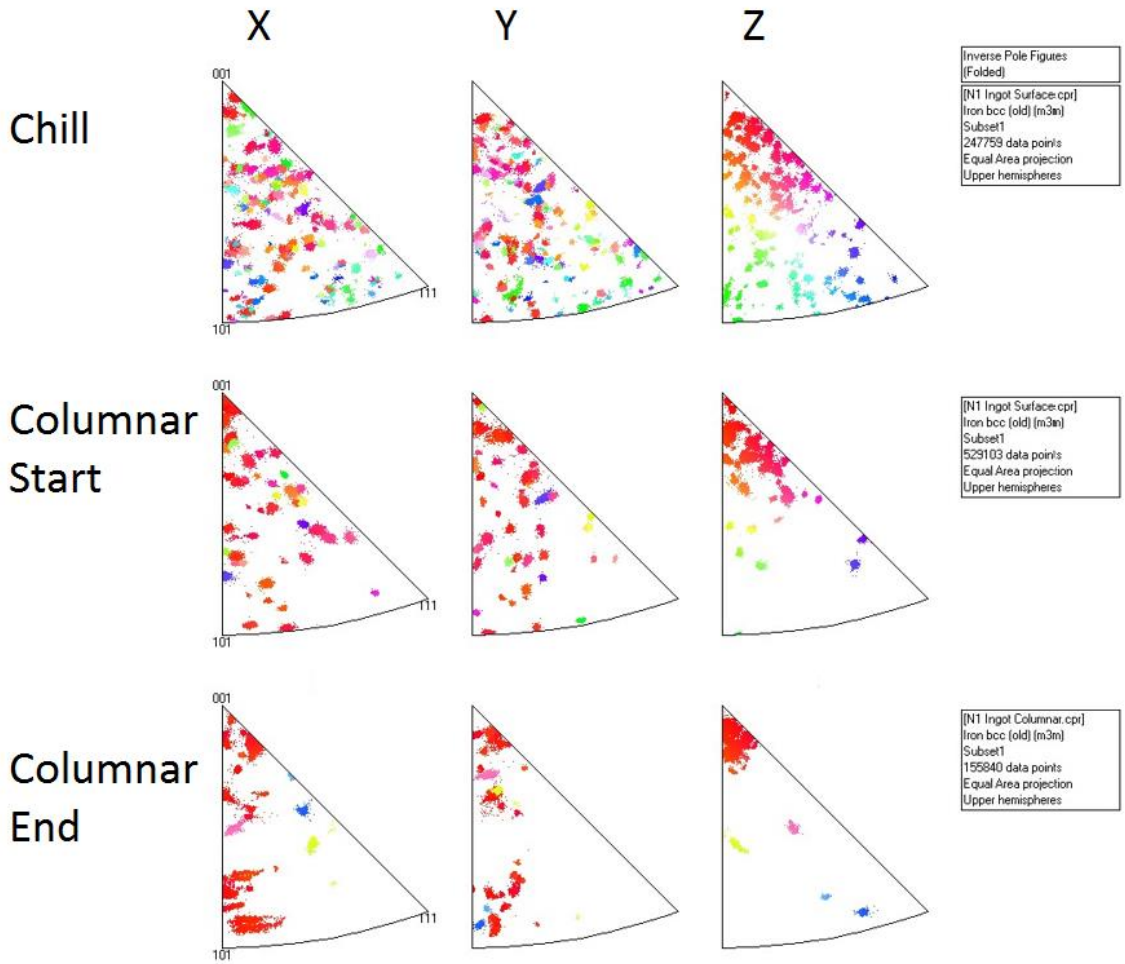

Figure 43 IPFs showing the distribution of grain misorientations from each axes in 3 regions of the N1 ingot.

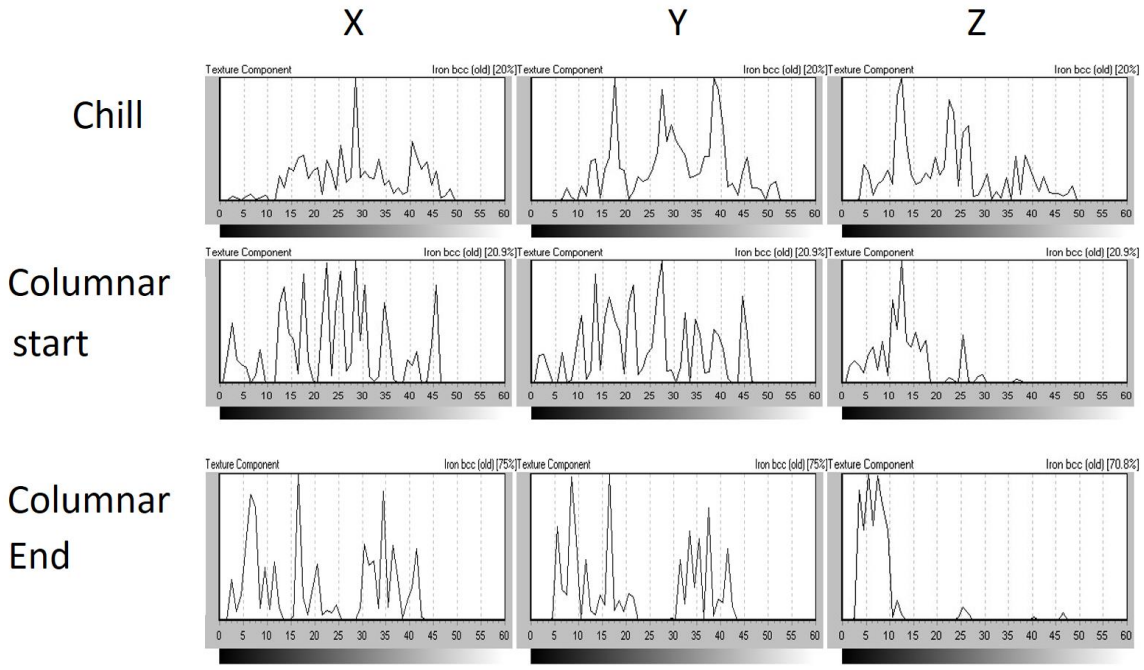

Figure 44 Graphs providing numerical values for the magnitudes of misorientations shown in Figure 43, the columnar zone starts at 1-2mm deep and extends to 28mm.

Figure 45 shows IPFs and misorientation graphs for each region in Figure 42, focusing specifically on misorientation from the growth direction, providing a more complete picture of structural changes with depth. It is clear that the misorientation range change rapidly in the early stages, then much more gradually later on (results from the chill, columnar start and 5mm regions are all very distinct but from 5mm to 28mm the differences are far less pronounced. This matches the EBSD maps in Figure 42 and quantified in Figure 46, showing an initially rapid increase in grain width as poorly aligned grains are eliminated and a much more uniform structure deeper into the material.

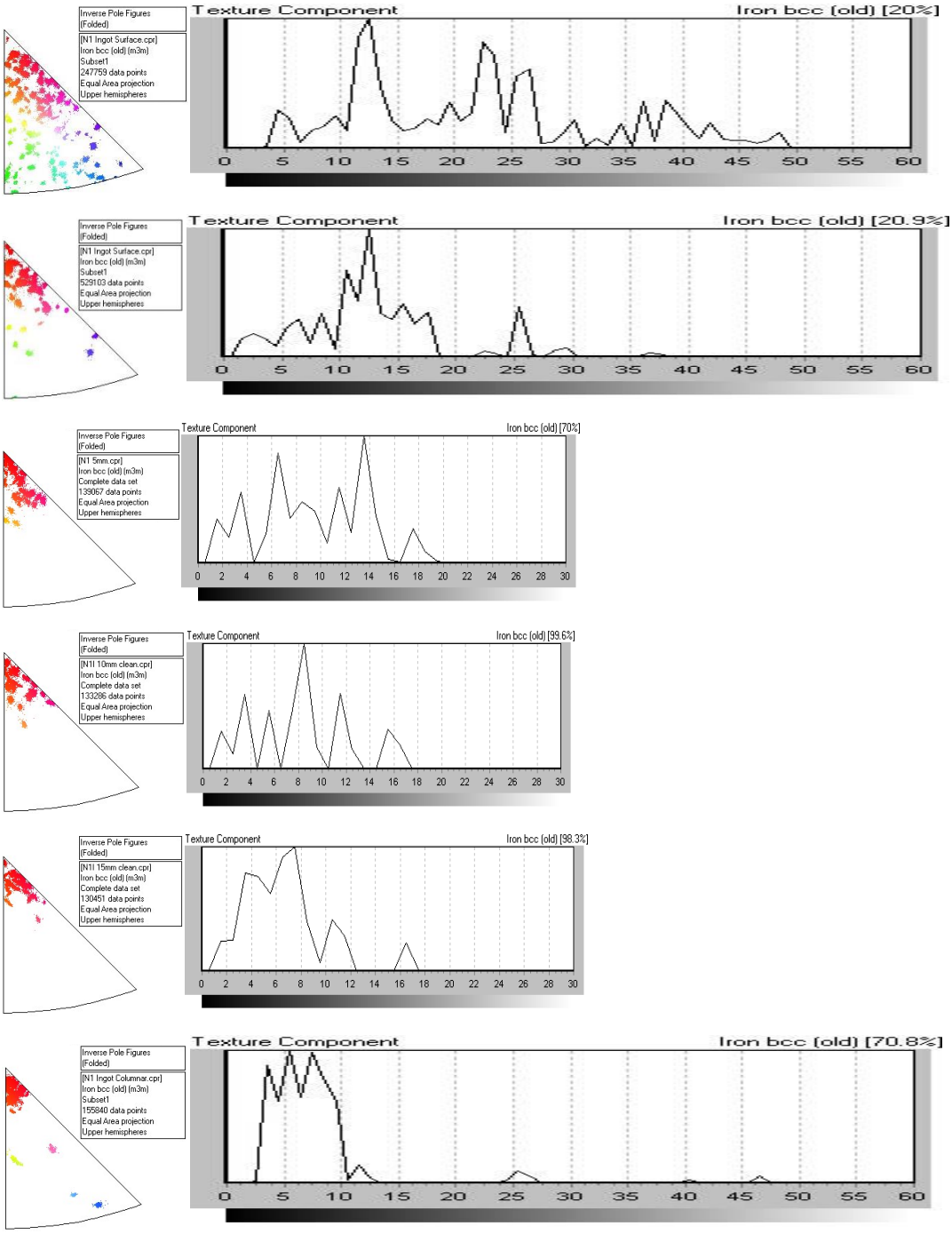

Figure 45 A complete set of IPFs and grain misorientation graphs against the Z axis for the regions of the N1 sample shown in Figure 42, contour IPFs are also shown, indicating how the distribution compares with a random distribution. Starting with the chill zone at the top and working towards the centre

Figure 46, shows how mean grain size compares with the average spacing of low misorientation grains through the N1 ingot. Low misorientation grains are the grains which fall in the range of orientations that are present at the deepest extent of the columnar zone, this was measured to be 12° in these ingots. While the grain size increases with depth, the spacing of low angle grains remains relatively constant. This is calculated by dividing the number of low misorientation grains by

the total width of all grains that are completely in the studied region so is best considered as the average spacing of the centre line of these grains and not just the space taken up by other grains. The deviation from the expected pattern for low angle grains in the chill zone may be due to a variety of factors such as competition from favourably oriented grains growing into the observed plane or simply an effect of the lowish sample size, since the size of grains in this work make large sample sizes difficult or time consuming to obtain. Particularly at the surface where surface roughness, curvature of the sample caused during polishing, and inconsistent conditions tend to result in some parts of the chill zone being lost or not visible. The size of individual samples throughout the EBSD section of this work has been limited by both the upper limit on the size of samples that can be mounted and a limit on the size of samples that can be mounted conveniently. The number of samples is also limited in part due to the time taken at both of the preparation and EBSD stages and difficulties in merging datasets for detailed orientation analysis of multiple samples as a single dataset. The orientation analysis is highly dependant on available software so developing work arounds to reliably combine data sets at that stage would likely require a significant time investment.

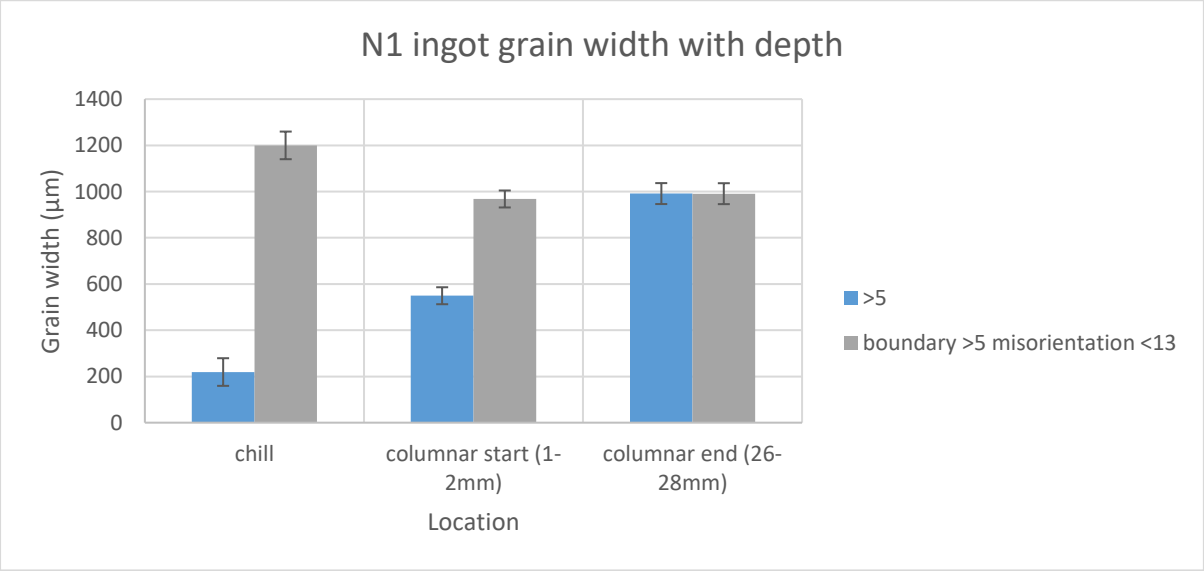

Figure 46 Grain width compared with low misorientation grain spacing through the N1 ingot.

5.2.4 N1 5mm cast

The first sample analysed from the Nano 1 5mm cast was from a middle height directly down the centre line where pouring occurred. Optical analysis showed grains smaller than in the large, slow cooled ingots, but with a distinct tilt to one side. EBSD later revealed that the crystallographic orientations of the grains were heavily offset from the thermal gradient. Given that results from

other regions of the cast show better agreement with a theoretical understanding of the driving force for growth being parallel to the thermal gradient, and perpendicular to the surface, this has been attributed to an effect of the column of pouring liquid. Figure 47 shows this effect, with one section taken from directly in the pouring column and the other taken off to one side, while the grain size in both are comparable, the one in the pouring column has noticeably tilted orientation while the other shows orientations perpendicular to the surface. There are 2 effects that seem likely to be at play here, one is the motion of the liquid causing a thermal gradient that varies with height and skewing the thermal gradient as columnar grains are starting to form. The other is the difference in thermal gradients, contact with the pouring stream will have already heated the mould surface before solidification fully begins, weakening any directionality compared to other parts of the mould.

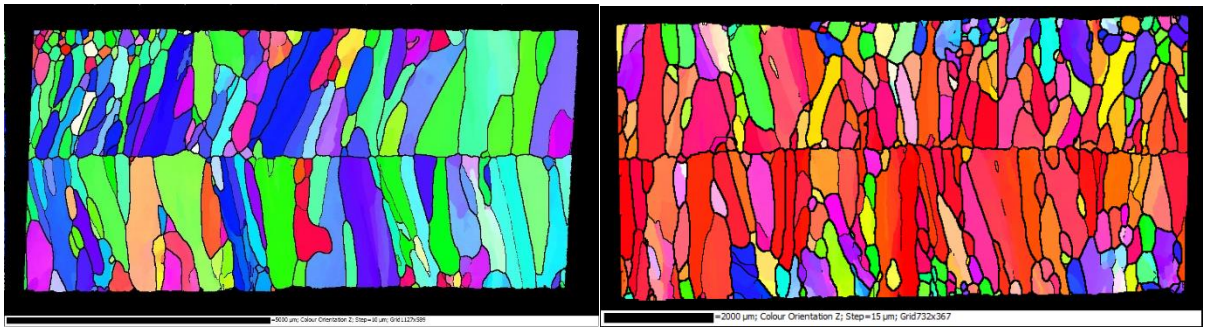

Figure 47 EBSD maps of the thin cast N1 sample a) in the centre where the pour was made and b) 1/4 width.

The 5mm cast of the Nano 1 material shows a finer grain size than the ingot but a comparable structure, with coarsening of the columnar grains. The IPFs and orientation distributions relative to an axis along the thermal gradient are shown in Figure 48. Since the samples are 5mm thick, there is only 2.5mm of material before the centre line, so data for the centre was taken at 2-2.4mm to avoid any effects that may be caused by the centreline.

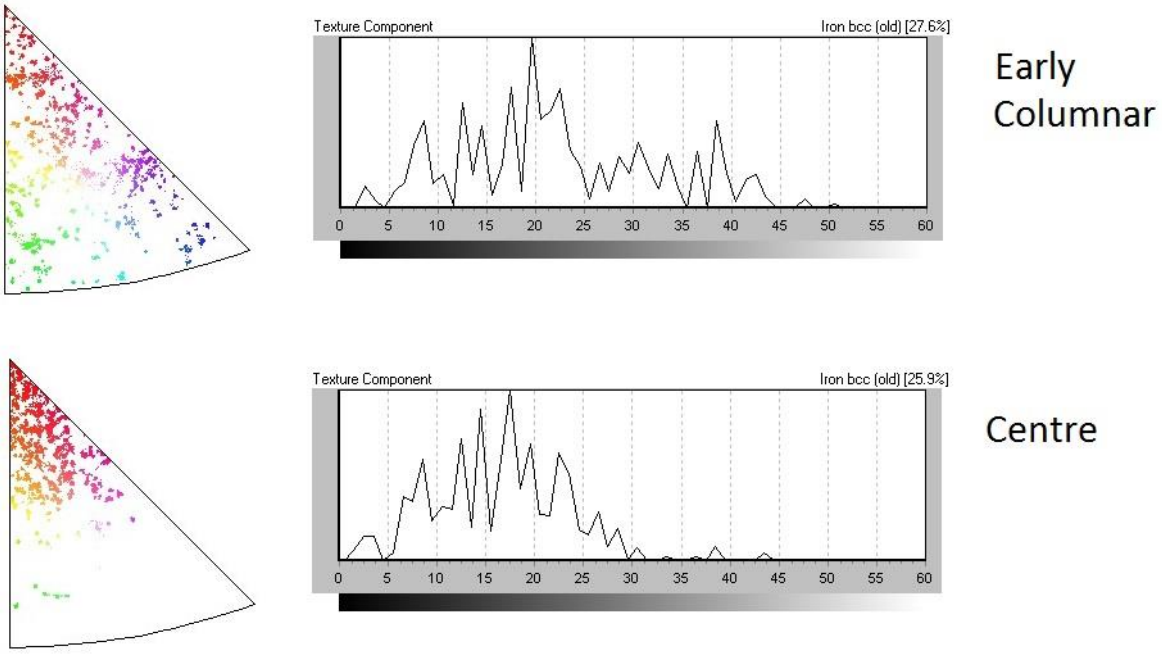

Figure 48 IPFs and misorientation graphs for the second section of the 5mm Nano 1 cast that was studied (Figure 47 right).

5.2.5 N1 15mm cast

Analysis of the 15mm cast, shown in Figure 49. Sections taken from the 15mm thick cast showed a few interesting features, the most noticeable of which was the central equiaxed zone, which formed despite being significantly thinner than the depth needed to produce equiaxed grains in the centre of the ingot. This can come from several factors such as reduced capacity of heat extraction of these mould compared to the ingot, as well as any difference in turbulences of the liquid steel. However, this will not impact columnar competition and the columnar to equiaxed transition length is not being assessed in this work.

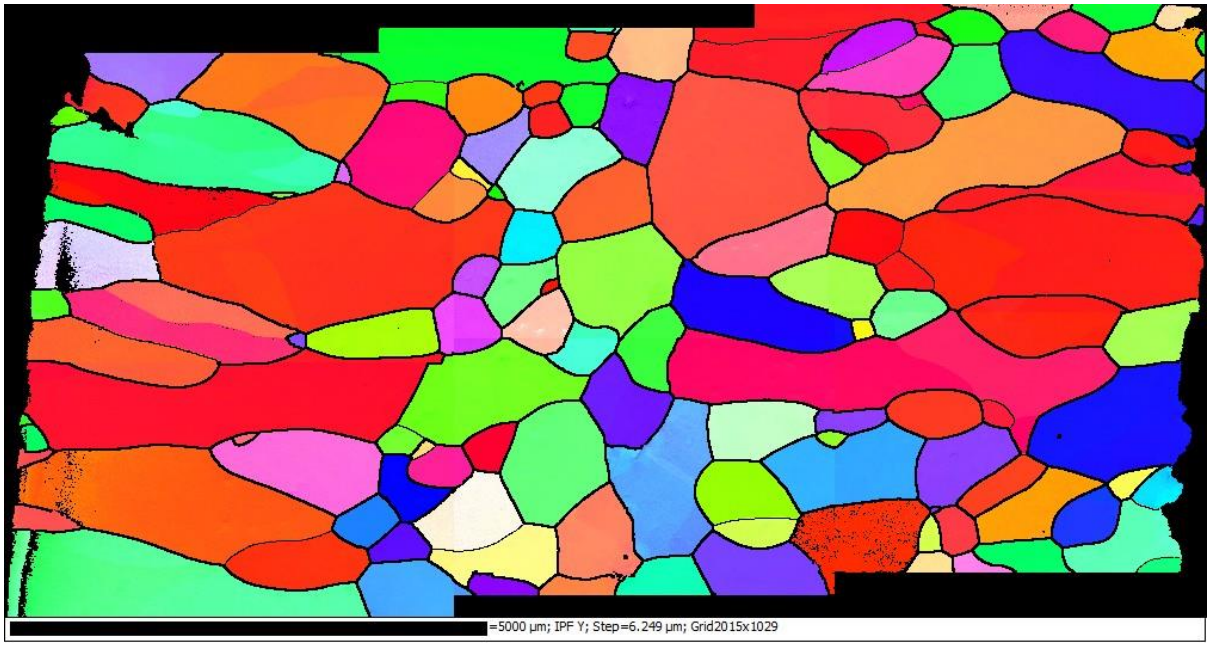

Figure 49 N1 15mm wide cast section.

5.2.6 BH Ingot

From Figure 50 it is clear that the BH ingot shows a similar pattern of development to the N1 ingot, with a surface region of diverse orientations, developing progressively more texture with depth. The IPFs and graphs in Figure 51 provide more exact descriptions of this variation. From 5mm deep the graphs have been shortened to keep the scale the same, since by this point all the most misaligned grains have been eliminated.

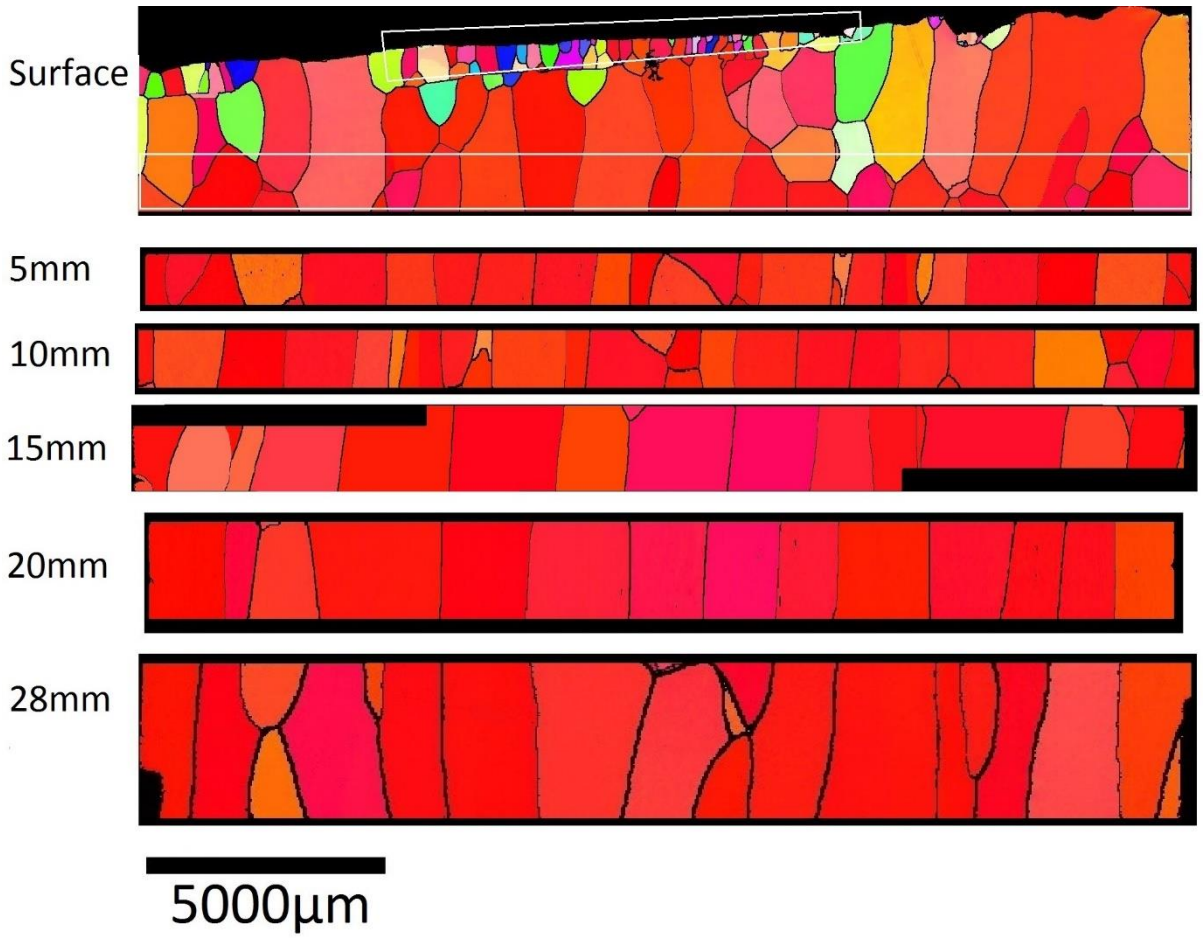

Figure 50 EBSD images taken through the BH ingot a)Surface, b)-e) 5mm, 10mm, 15mm, 20mm from the surface and f) 29mm from the surface.

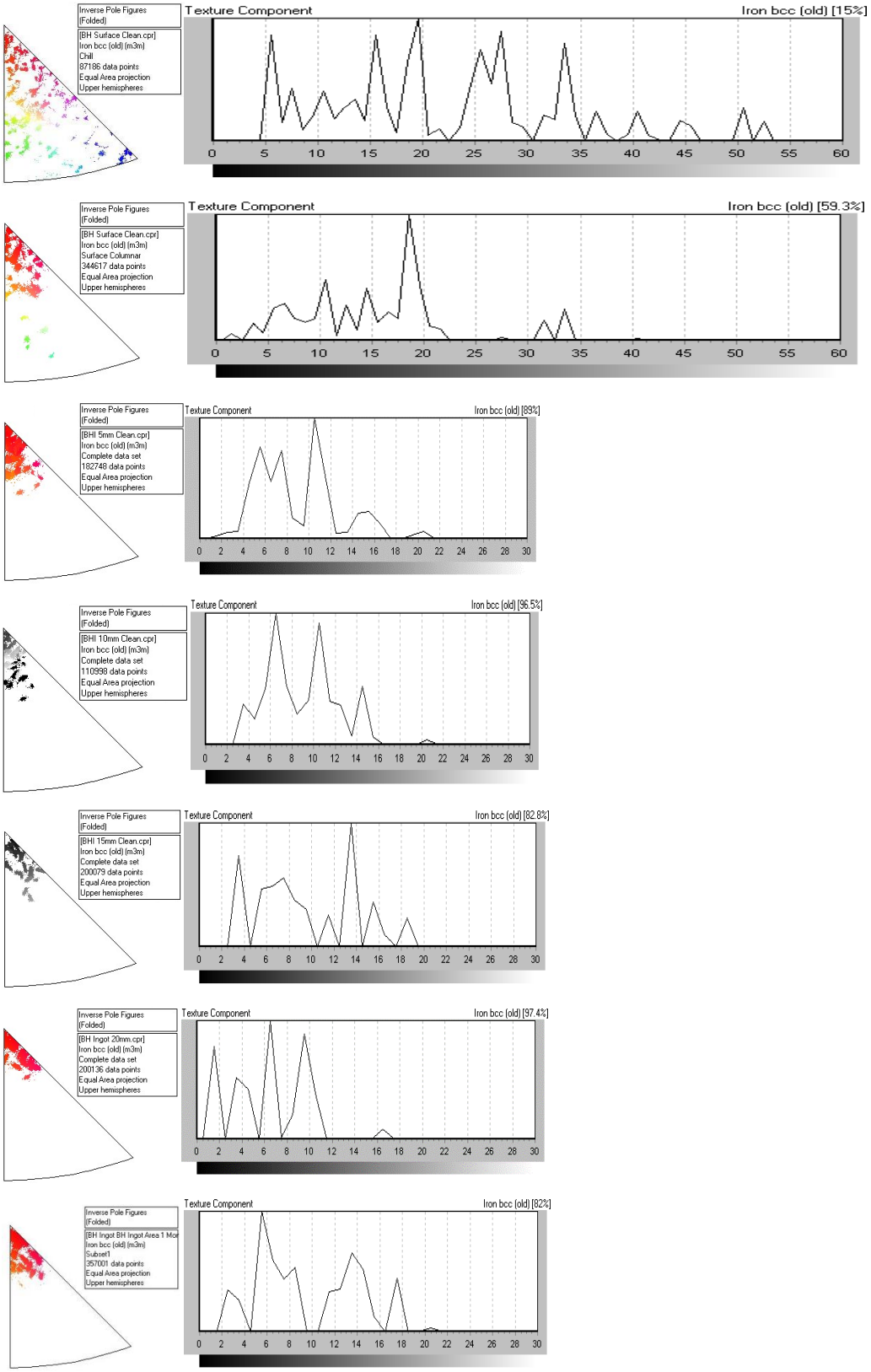

Figure 51 IPF and graph showing grain misorientation through the thickness of the BH ingot a) surface chill, through b)-f) surface columnar, 5mm, 10mm, 15mm, 20mm, to g) 28mm.

5.2.7 BH 5mm cast

Like with the Nano 1 thin cast, the BH thin cast (Figure 52) shows a finer grain size and more scatter of orientations than at the same depth into the ingots, but as with earlier results, the grain sizes are again larger in the BH than the Nano 1 for the same conditions. There is also significantly more variance in the structure, with some regions of very wide grains extending from surface to centre and others with thinner grains that are blocked off and replaced by other grains, compared to the more uniform mixture seen in the Nano grade.

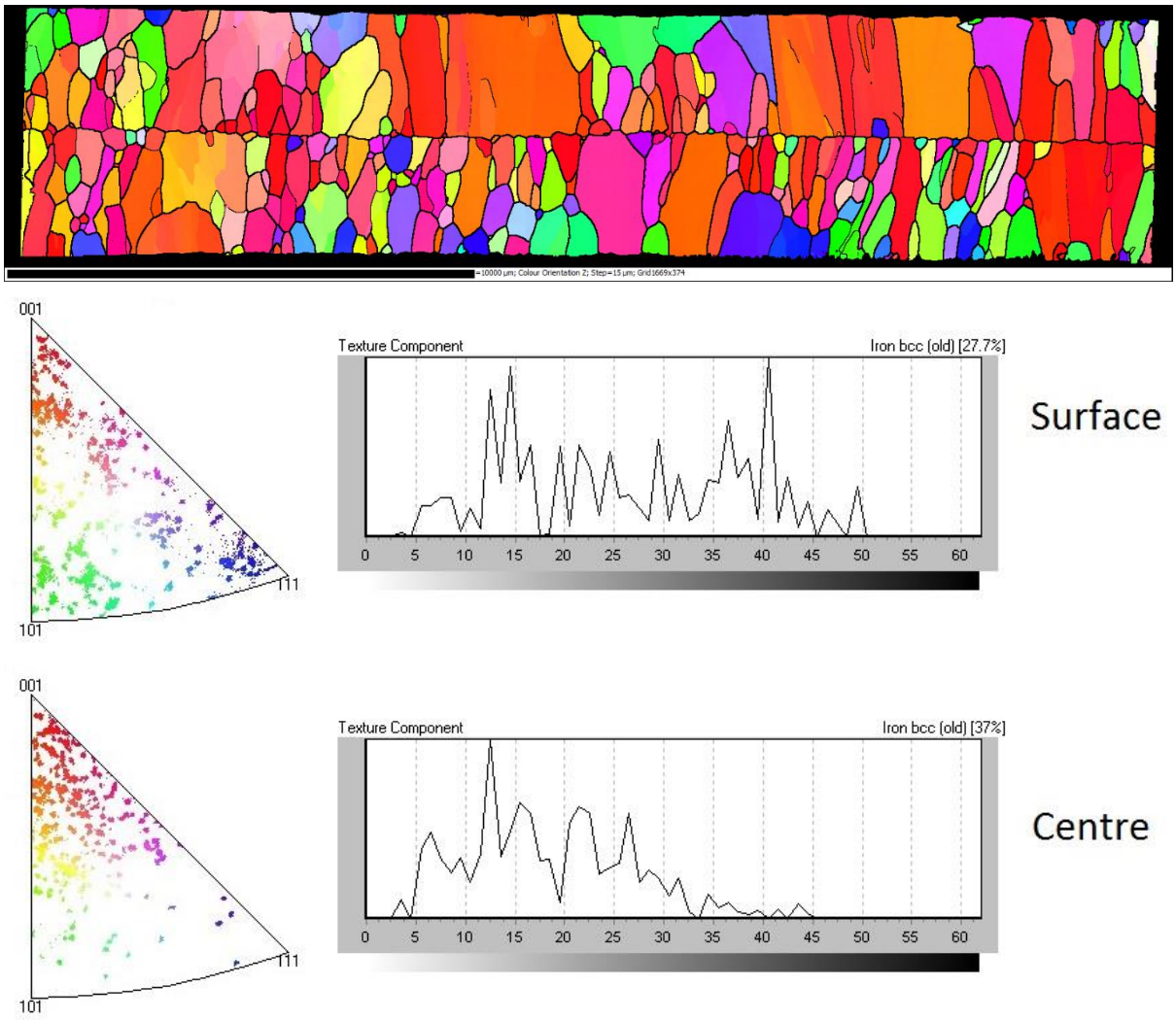

Figure 52 Map and IPFs and misorientation graphs for the BH 5mm cast.

5.2.8 Comparison

Figure 53 shows how the columnar grain width varies between samples at a fixed 2mm from the surface, allowing a comparison of the rate of elimination between different conditions, both the cooling rates achieved and changes in composition. The first notable factor is that comparing the two ingots we see that the BH grade has larger grains than the Nano grade, this is consistent with

the compositional differences giving the BH grade a much narrower mushy zone which inhibits nucleation after the first grains have started growing more readily than in the Nano grade with a wider mushy zone. Comparison of the different conditions for the Nano grade are also broadly consistent with expected behaviour but also suggest more nuance. The results suggest that while a slower cooling rate does lead to larger grain sizes, this is only true u to a point since the cast with a cooling rate of 150K/s has a notably finer microstructure than the 10K/s cast, but the 10K/s and 0.6K/s casts both show very similar grain sizes at 2mm deep into the material, indicating that there is a sensitive region where cooling rate strongly influences grain size and other regions where cooling rate is less of a factor. Obviously if taken to the extreme this would eventually reach a point where solid state grain coarsening mechanisms can come into play but that is beyond the scope of this work and outside the range of conditions considered. Results are shown for both a 5° local misorientation constituting a grain boundary because this matches well with the boundaries in the optical parts of this work and 15° local misorientation because in literature this is a commonly cited figure for the transition between low angle and high angle grain boundaries.

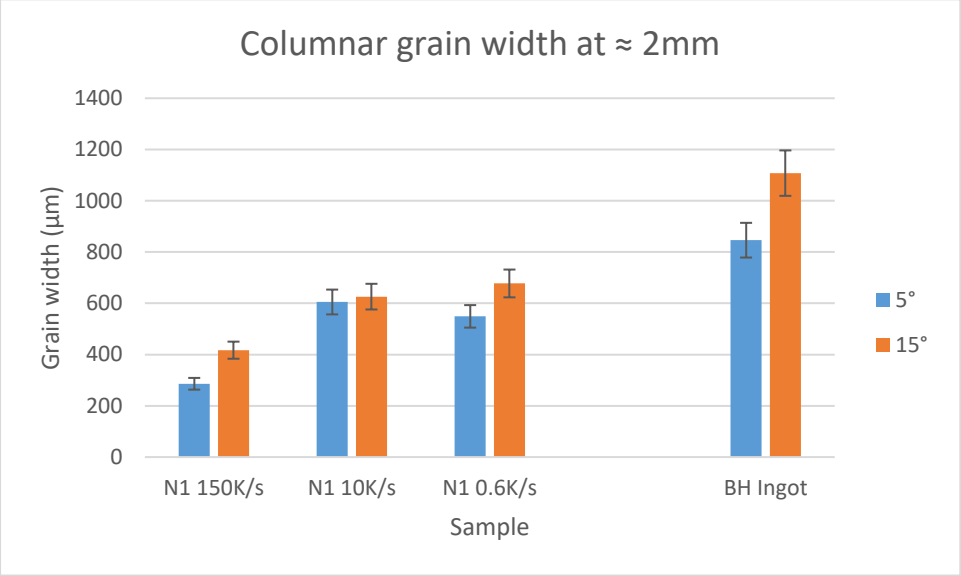

Figure 53 Variation of columnar width at 2mm deep across samples. Cast 1 has the high cooling rate of approx. 150K/s, the two ingots have slow cooling rates near 0.6K/s while the wide cast has an intermediate cooling rate measured around 10K/s.

Figure 54 and Figure 55 contrasts the changes of the N1 and BH ingots with differing depths. Again the low misorientation grain spacing is the distance between grains that are <12° from the thermal gradient and are thus in the range of orientations that survive the full length of the columnar zone. By measuring the average width of the grains completely within the studied area and plotting how the grain widths change with depth it is possible to start developing a more quantitative understanding of the rate of grain elimination through the columnar zone of materials. Figure 54 shows that the grains in the BH ingot are consistently larger than the N1 ingot across depths and this

trend also applies to the spacing between low misorientation grains. This matches with earlier results and both ingots have an initially rapid increase in grain width with depth that later plateaus, but relatively consistent low misorientation grain spacings, for the Nano grade this plateau seems to occur at around 10mm deep and the data for the BH grade is too noisy to be specific, but seems to plateau somewhere in the 10-20mm range. While none of the built in trend lines were suitable for plotting an asymptote, moving averaged were consistent with this behaviour, showing a clear upward trend at the start of the grain width lines and chaotic but usually subtle behaviour in the rest of the graph. Figure 55 then shows that both alloys have broadly the same progression of texture development as depth increases, again a rapid change at shallow depths then slower change deeper into the material. Since the behaviours are consistent with what was expected, it should be possible to produce a model that allows more specific prediction of as cast grain and misorientation behaviours in different conditions. The error bars here are based on the accuracy of marking depths with the mm markings on a standard ruler and misorientation with placing the sample in the SEM.

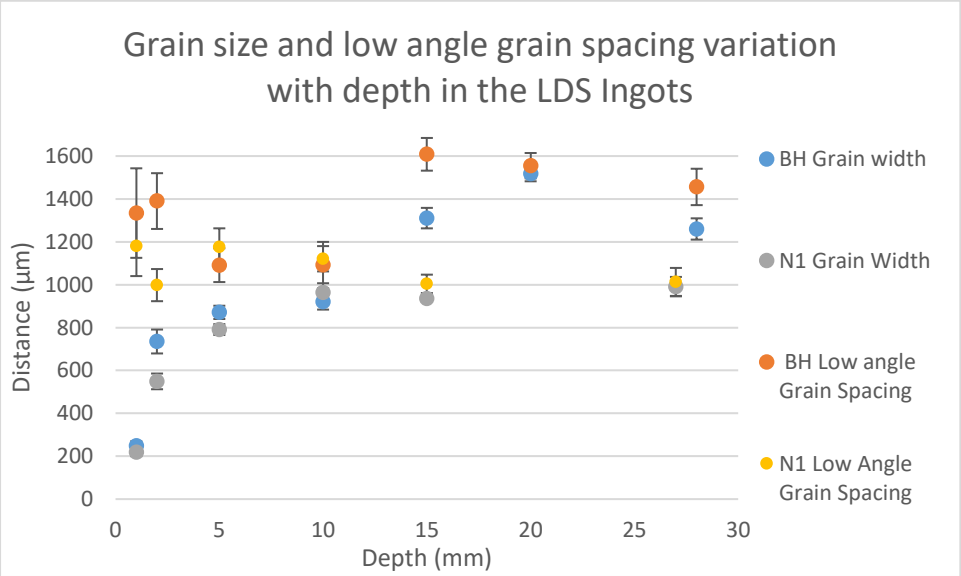

Figure 54 Grain widths and low misorientation grain spacings with varying depths in the BH and N1 ingots.

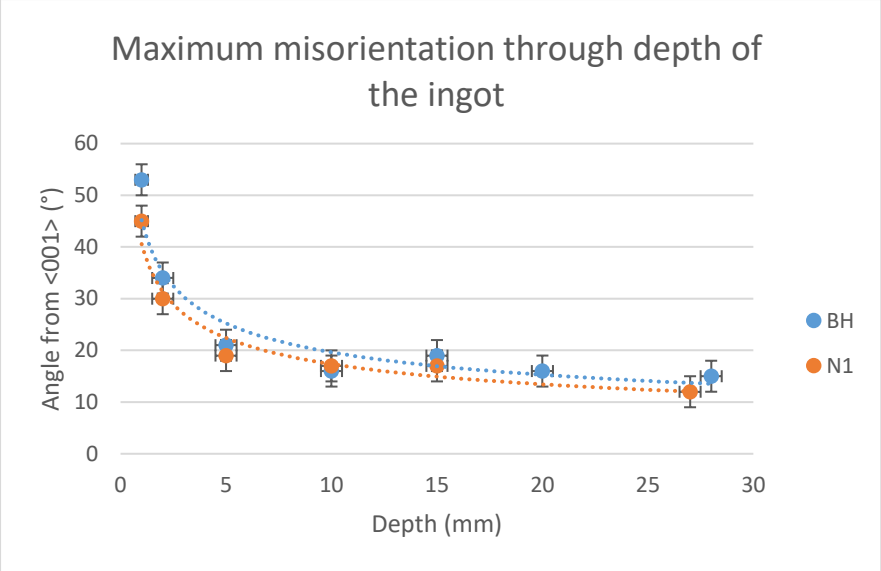

Figure 55 Changes in maximum misorientation from the growth direction through different depths of the BH and N1 ingots.

Figure 56 Shows how maximum misorientation changes with depth in the Nano grade with changes in cooling rate. This shows that the 15mm and ingot casts have very similar changes in misorientation with depth, but that the thin cast maintains greater misorientation deeper into the material.

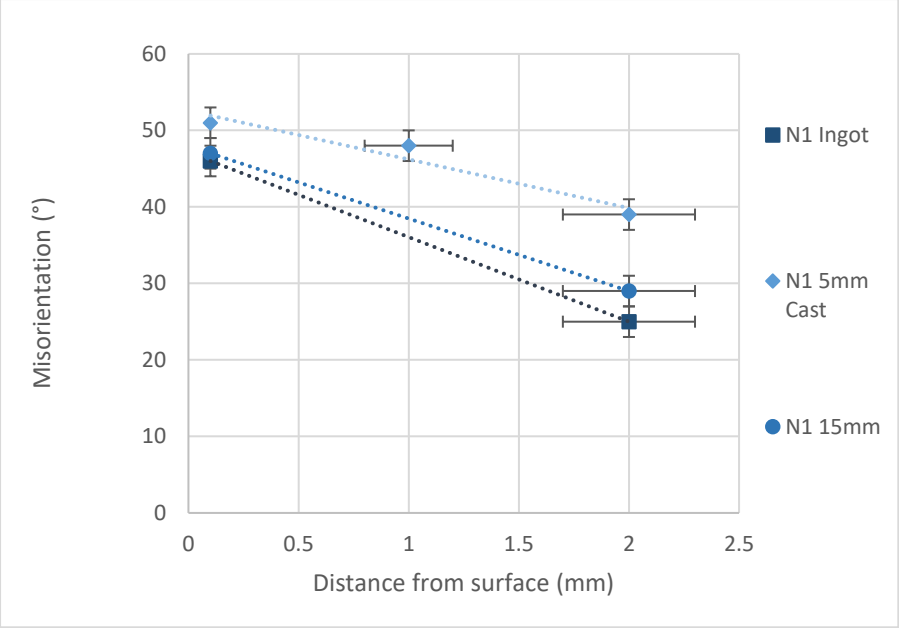

Figure 56 Comparison of the maximum misorientation with depth for the Nano grade with various cooling rates.

Figure 57 and Figure 58 quantitatively show the distribution of orientations across the samples studied, this confirms what was already apparent, but allows us to put numbers on the densities of orientations throughout the experiments. It is apparent that the thin cast surface either has the

same distribution as the ingot surface, or possibly has a slight bias for well aligned grains, but by 2mm deep seems less aligned than 2mm deep into the ingots. This hints at the thin casts maintaining misaligned grains and thus a finer grain size deeper into the columnar zone. There is also strong agreement between both cooling rates for the two materials, especially in the ingot samples, suggesting cooling rate has a more pronounced effect on the rate of coarsening through the columnar zone than the change in composition, despite the composition change having significant effects on related properties such as the absolute grain size.

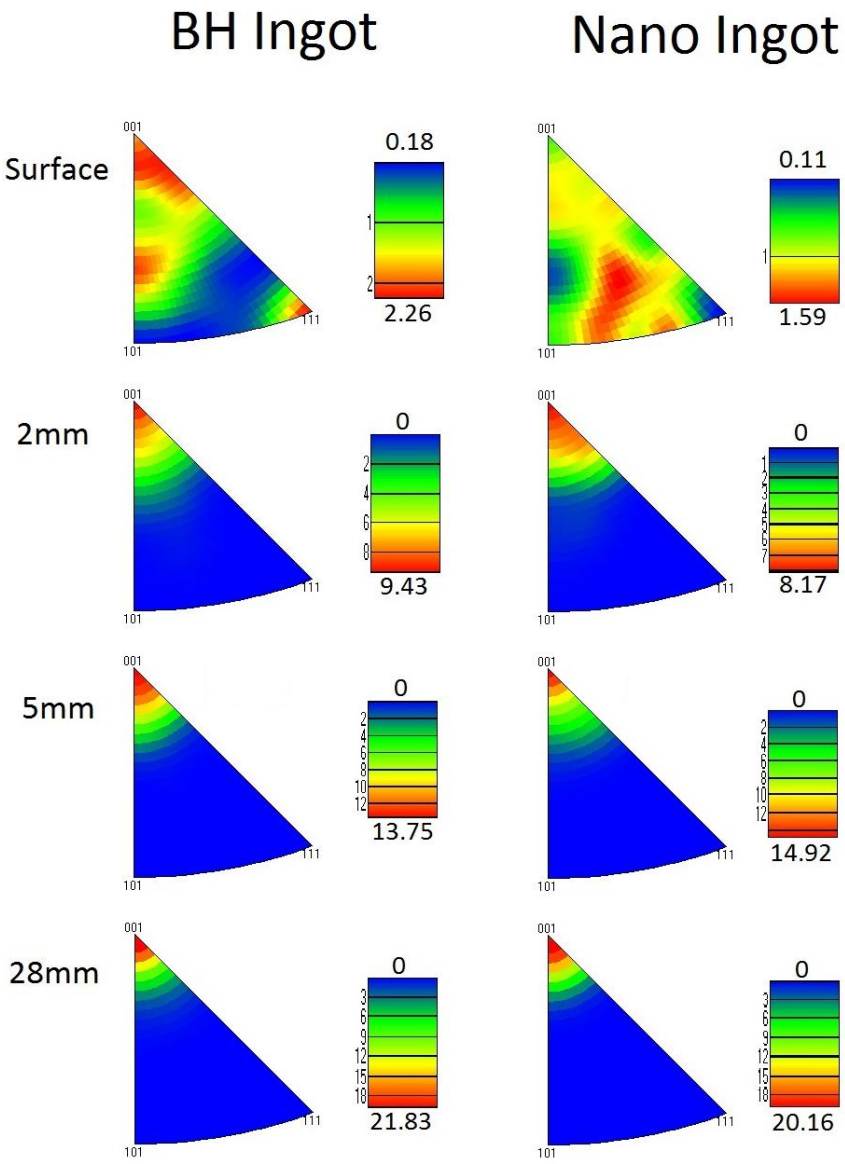

Figure 57 Orientation densities in the received ingots

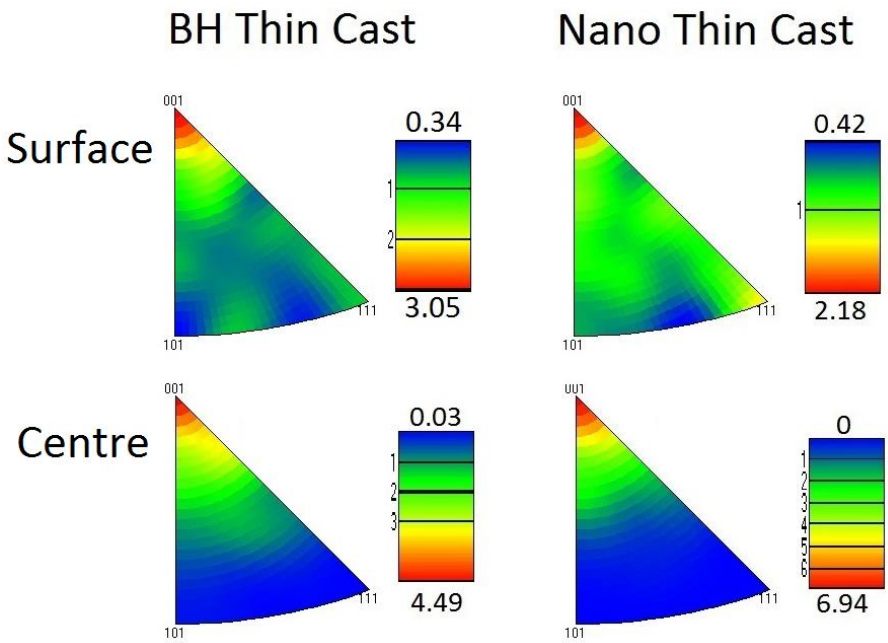

Figure 58 Thin cast orientation densities.

Figure 59 includes IPFs for both grades at the extremes of observed cooling rates over a range of depths suitable for comparison, allowing for easier comparison of the different conditions. And highlighting that while the ingots appear to have slightly more texture at the surface, by 2mm deep the ingots have developed a stronger texture than the thin casts. This offers another way of measuring the phenomena seen in Figure 56.

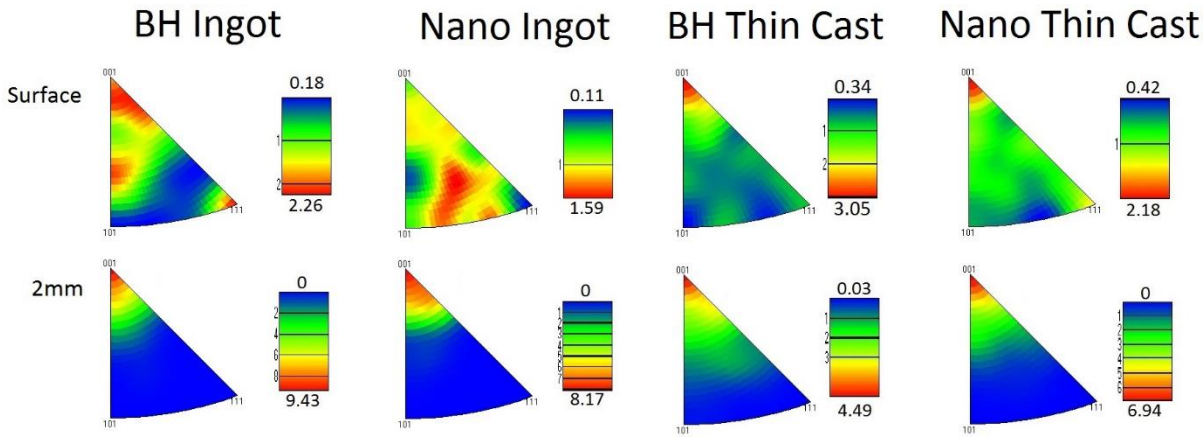

Figure 59 Surface and 2mm IPF contour plots for both materials at the lowest and highest studied cooling rates

The highest cooling rates here are similar to the lowest cooling rates that will be seen in belt casting, and still at least an order of magnitude below those seen in twin roll casting. Thus while they can provide insight for thicker single belt casts, these results are not as suitable for these higher cooling rates. They do however add to the limited data available for higher cooling rates under controlled conditions, bringing the range of experimental data closer to the cooling rates seen in these

techniques which will allow for better testing and confirmation of the reliability of models into the extreme cooling rates of twin roll casting.

5.2.9 Wedge Mould

The predictions of the COMSOL model for 5mm and 15mm wide sections matched well with the results for conventionally shaped ingots of these thicknesses, initially supporting the viability of this technique, the top surface of this model also matched well with the thermal imaging measurements.

The wedge mould proved effective in giving an easy to comprehend view of the impact of cooling rate on grain size, however it was realised that the approach may not be suitable for more quantitative work. When sectioning the options are either across the full range of cooling rates, which gives a very small sample size for each condition. Or across a single cooling rate which has the issue of the grains growing at a slight angle relative to the cut, meaning some grains will appear shorter as they pass through the sectioned plane, and this reduced apparent grain length will likely have a smaller but non zero impact on the observed grain width.

Thus the benefit in being able to produce results for multiple thicknesses (cooling rates) from a single cast are offset by the difficulties incurred in analysis. Figure 60 shows this clearly, since the EBDS map of the tip seems to show a clear increase in grain size with sample width but then none of the grains from the middle section are as wide as the widest grains from the map near the tip. However the continuously changing thickness gives a very limited sample size for each thickness so this unexpected result is likely just statistical noise.

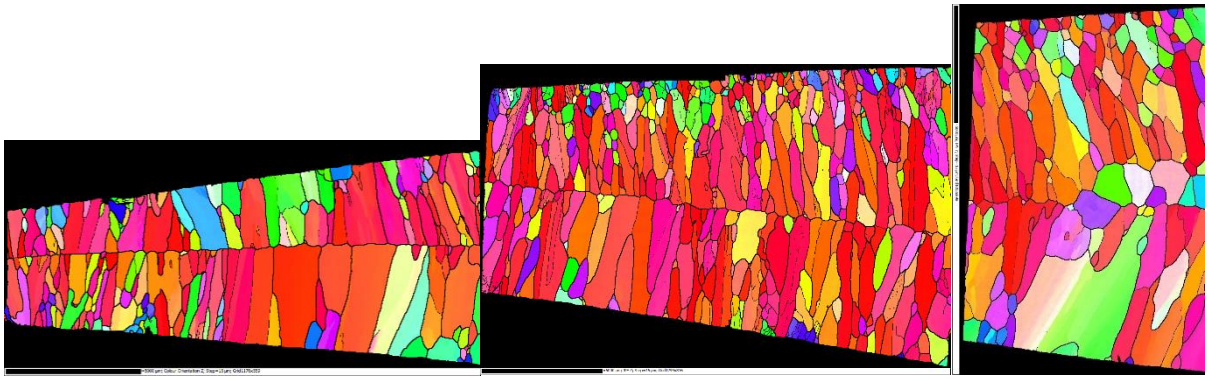

Figure 60 EBSD maps of a single section through a N1 Wedge casting.

5.2.10 Understanding the influence of SDAS on columnar competition

At the solidification front less well aligned grains lag behind more well aligned grains, where the increase in thermal gradient causes faster growth, which compensates for the component of growth

that is perpendicular to the thermal gradient. And while there are additional complexities to columnar competition that have been discussed earlier, the requirement for grains to out compete is for a secondary arm to grow over the top of one of the lagging grains. The practical upshot of this is that the aggressiveness of competition is dependant on an interplay of SDAS and mushy length, with some element of chance relating to the positions and orientations of nucleating grains. The mushy zone was calculated using the alloys solidus-liquidus range and the thermal gradient obtained from the COMSOL model. Since the mushy length is determined by the mushy zone temperature range and the thermal gradient, which itself changes linearly with cooling rate, but SDAS has an exponential component, this leads to the variations in competition with cooling rate. Table 13 consolidates this information

Table 13 SDAS and Mushy Length values for the Nano steel grade

	Ingot	15mm cast	5mm cast
Cooling rate (K/s)	0.6	10	50
Mushy Length (µm)	26000	1600	110
SDAS (µm)	70.3	35.2	18.1
SDAS % of mushy length	0.27	2.2	16.4

The mushy zone lengths shown are calculated by combining the thermal gradients seen in the COMSOL model with the thermal mushy zone for each composition to get the distance between the solidus and liquidus boundaries. Considering the results discussed earlier, where competition is very similar between the 15mm cast and the ingot, but the 5mm cast shows a notably slower elimination of misaligned grains, this puts a limit on the sensitive region. With a SDAS of <≈ 2% of the mushy length having at most a minor influence on competition, but there being a sensitive range somewhere above this. This seems a reasonable value since behaviour of interest takes place within a few SDAS of the tip, but many secondary dendrites can exist down the mushy length. It is also likely that there will be a region of extreme cooling rates where the SDAS is so large compared to the mushy width that the system again becomes insensitive because regardless of orientation, the secondary arms will always be too far behind the tip to influence adjacent grains so changes within this region have a negligible effect on competition. This is a topic that seems to have been largely overlooked in the literature before now and these results indicate that one end of the sensitive region begins with a SDAS between 1/6 and 1/50 of the mushy length, with the other boundary being somewhere > 1/6.

5.3 Dendritic Spacing

This section looks at the relationship between cooling rate and SDAS in the LDS grades, primarily with optical microscopy and the CLSM method discussed earlier. The industrial interest here is in gaining understanding of these grades to help with developing a production route. And the scientific interest is a better understanding of solidification more generally, since these are single phase they are well suited to this more fundamental comprehension. The method is also a novel contribution in its own right, demonstrating the ability to observe dendrites structures in situ, including grades where conventional techniques are not suitable. A better understanding of the variations in SDAS are of particular interest in light of the proposed dependence of columnar grain morphologies on an interaction between the mushy length and SDAS.

5.3.1 CLSM Method Pros and Cons

Table 14 gives a quick summary of the major advantages and limitations of the CLSM that was used for this work.

Table 14 Summary of the CLSMs advantages and disadvantages for this work.

CLSM	
Advantages	**Disadvantages**
Can achieve arbitrarily low cooling rates	Small sample sizes (very small for in situ observations)
Good control over cooling rates	Can't achieve high cooling rates
Very good atmospheric control	Heating and cooling must be programmed at the start
In situ observation of microstructure is possible	Surface observation only

5.3.2 Effects of Ta

One of the Ta doped CLSM samples was placed in the SEM for composition and segregation analysis. A line scan through an enriched late solidifying region shows a fine network of precipitates rather than a single structure (Figure 61) and the precipitates are made up of Ti, Ta and C, with Fe and Al signals dropping sharply and other elements not giving a significant number of counts anyway. This matches well with the Thermo-Calc models which predict a TiC phase coming out In the final stages of solidification for the standard N1 alloy (without Ta impurities) and the model with 0.8%Ta makes similar predictions, although this amount is only an educated guess not the exact amount of Ta dissolved into the sample.

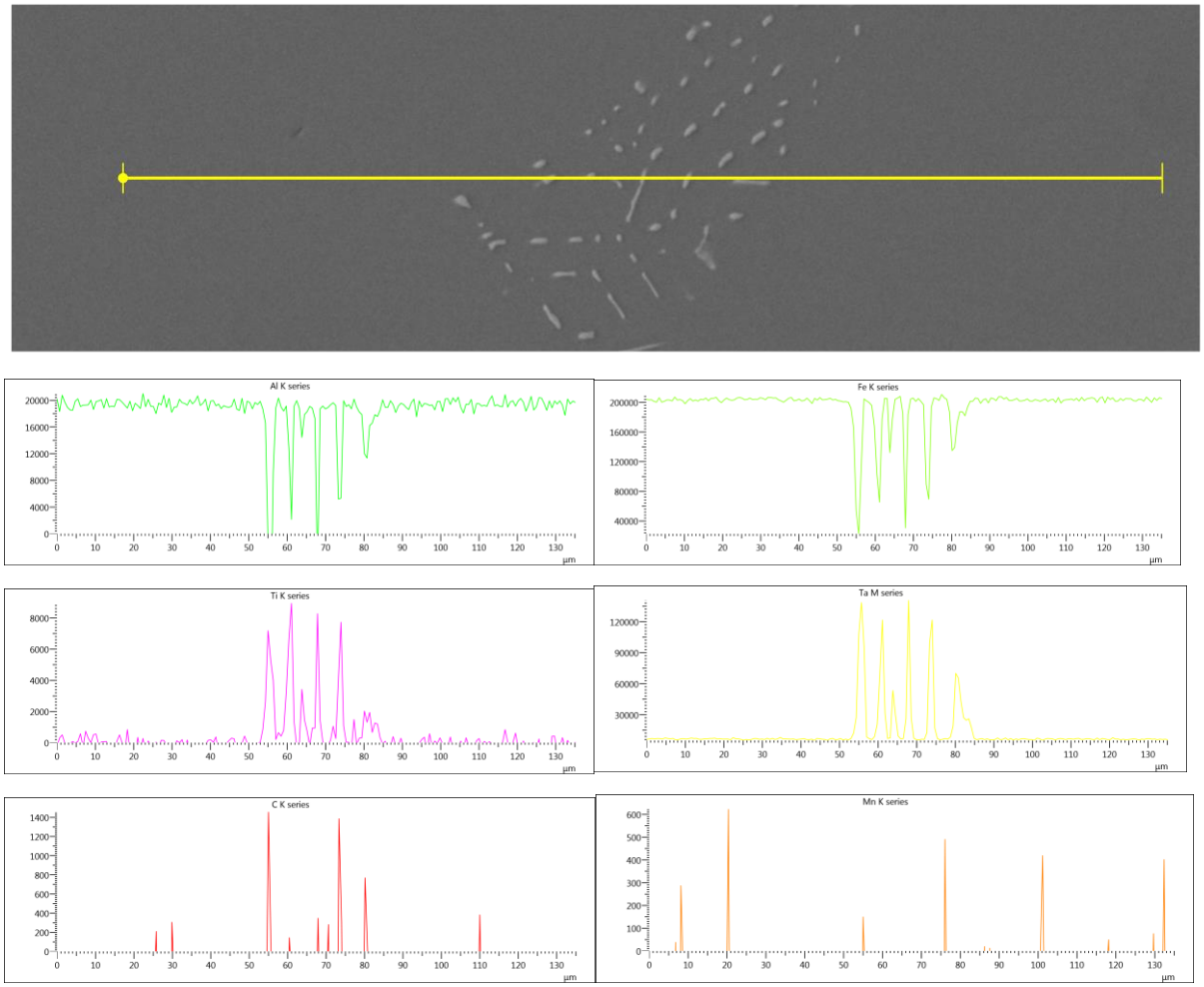

Figure 61 Line scan through a late solidifying section of the Ta enriched N1 material and the associated counts for significant elements.

Since Ta doping could be used to reveal the dendritic structure it is important to understand the degree to which this doping influences the structure, Figure 62 shows surface SDAS measurements for the Nano1 grade with and without Ta additions. Even though the lines do appear to begin diverging, the larger error bars inherent to this technique still overlap. These results are consistent with the Ta doping having a small or negligible effect on the SDAS of the materials and give confidence that the bulk Ta doped samples provide results that are at least close to the size of the dendritic structures in undoped samples. Especially since the surface observations are of the last solidifying material, so segregation and thus the effect of additional elements will be most pronounced.

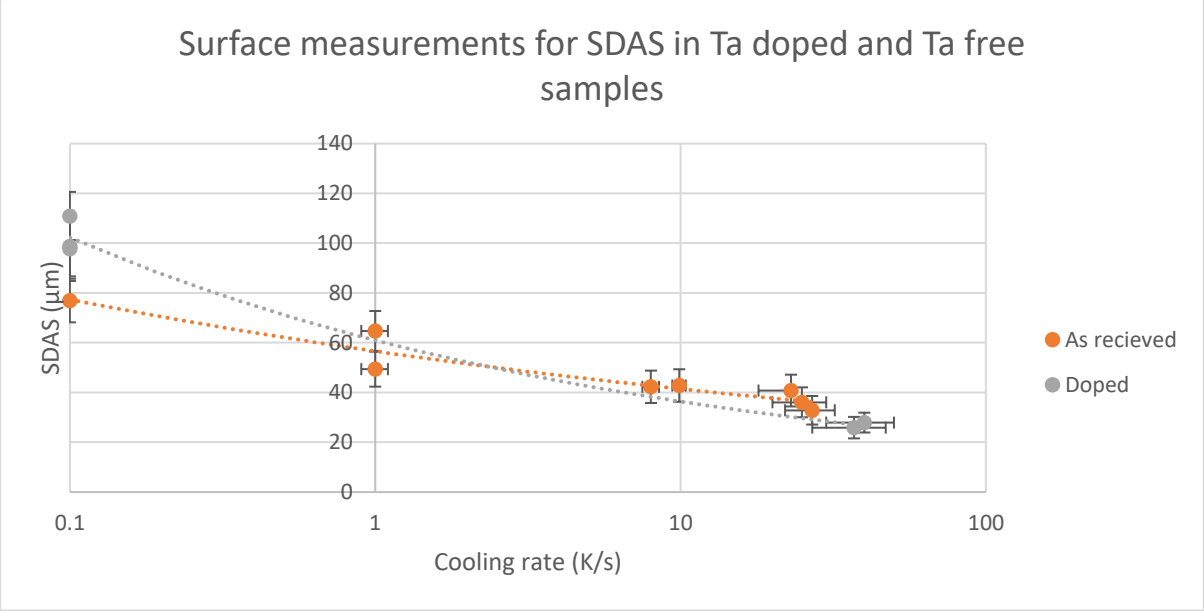

Figure 62 SDAS variation with cooling rate on the surface of samples with and without Ta doping

5.3.3 CLSM in depth primary and secondary dendrites

After preliminary work had eliminated most of the experimental difficulties an in depth study of primary and secondary dendrite spacings with cooling rate was carried out using the N1, N2 and BH. Unfortunately the Ta doping technique which proved effective at revealing the dendritic structure in the nano precipitate hardened samples had no effect on the bake hardenable samples. In addition to this the BH samples developed a significant fraction of floating impurities, covering the surface and preventing in situ dendrite observation during growth. Between these complications, very little useful information could be gained from the BH samples and the grade was excluded from the analysis. Both Nano samples however proved much simpler to work with and surface measurements from both showed good consistency with bulk measurements taken later, meaning the surface results can be reliably taken as comparable to bulk SDAS. The tests performed are shown in Table 15, for each condition 3 tests were performed to increase the reliability of the data. Since N1 and N2 are so similar only the extremes for N2 were initially performed and since the results were as expected this was considered sufficient to assume the same behaviour. The dashes in the BH column indicate which conditions were attempted.

As noted in the methodology section, the equipment struggled to achieve the intended cooling rates above around 10K/s, with the 50K/s target leading to cooling rates more in the region of 25-30K/s, operating near the limit of the cooling rates achievable by the equipment is the cause of cooling rate variation for the highest cooling rates.

Table 15 Matrix of tests for CLSM in depth dendrite analysis

Intended cooling rate (K/s)	Material		
	N1	N2	BH
0.1	X	X	-
1	X		
10	X		
24			
50	X	X	-

Figure 63, and Figure 64 show the primary and secondary dendrite spacing with temperature for two of the low density steels. Results for both show the ratio of primary to secondary spacing is an approximate fit for literature results of $\lambda_1 \approx 2\lambda_2$, with the highest ratio being 2.7:1 and the lowest 1.3:1. The N1 materials also showed good consistency with the expected form of $\lambda_2 = a\dot{T}^{-b}$ (the two data points for N2 prevent making this conclusion, but they fall where expected so the same behaviour was assumed).

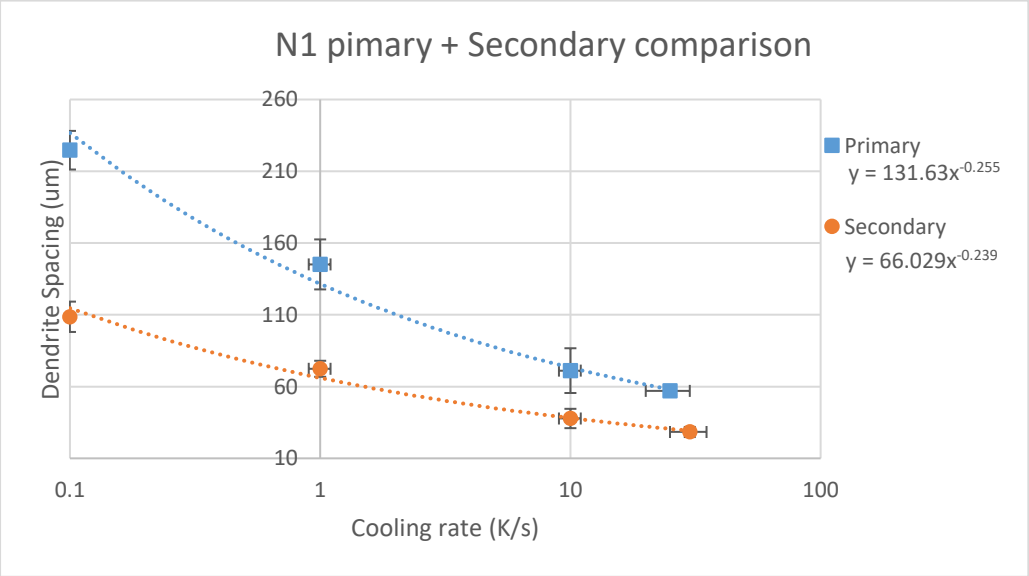

Figure 63 Primary and secondary dendrite spacing for the Nano 1 steel.

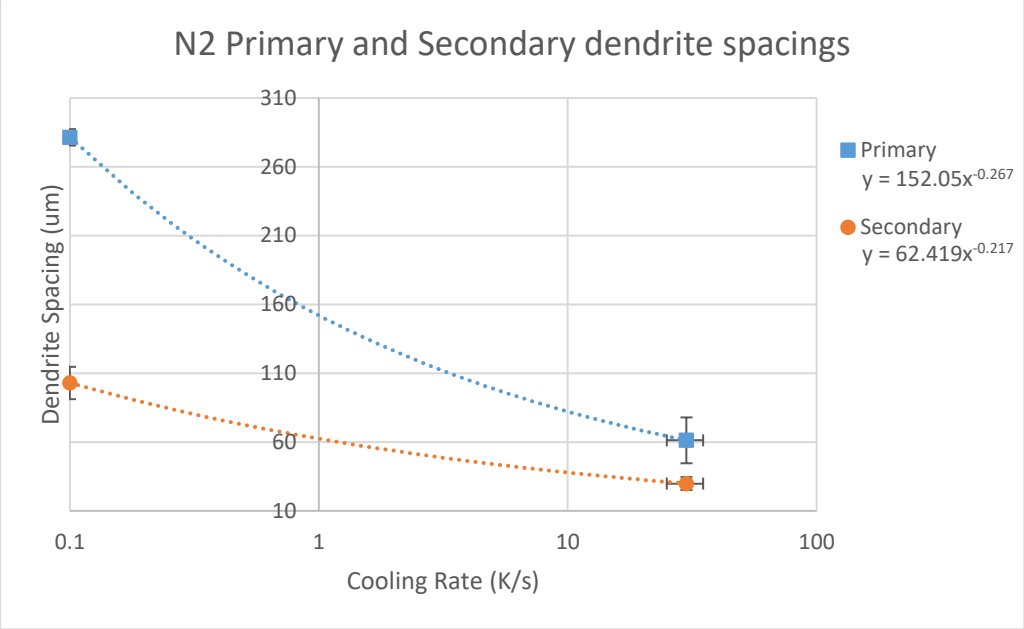

Figure 64 Primary and secondary dendrite spacing for the Nano 2 steel.

Figure 65 and Figure 66 show the combined primary and secondary spacing results from the preceding graphs in order to more clearly show the variation of each spacing between materials.

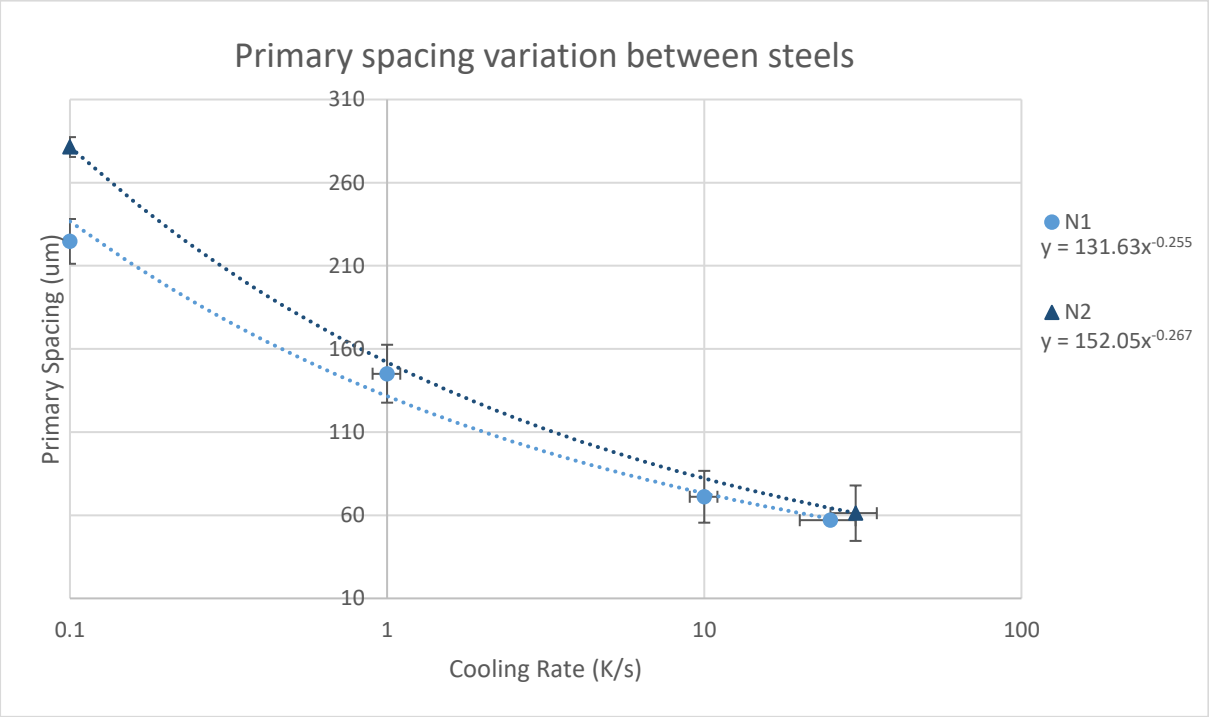

Figure 65 Cooling rate to primary dendrite spacing curves for the three steels studied.

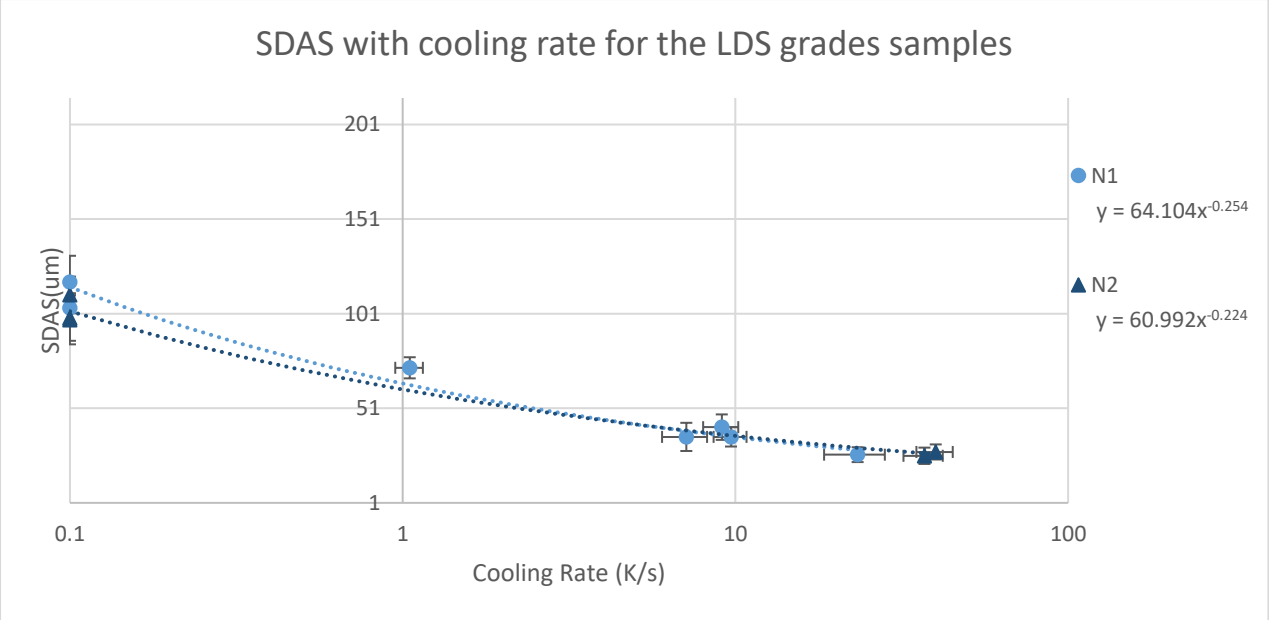

Figure 66 Cooling rate to SDAS curves for the steels studied, including two curves calculated from fitting parameters found in the literature for 304 stainless steel.

5.3.4 Surface and bulk comparison

Figure 67 compares SDAS measured through the bulk of samples using the conventional cut, polish, and etch methodology, to measurements made in situ during solidification at the surface of the samples. While the domed surface only allowed for observation of a small region of the surface, and as such the surface results show more scatter and are less precise, they clearly show a strong tendency to approximate the results for the bulk material, with trend lines for the two observation methodologies falling very close to each other for both materials. This suggests that while composition may impact SDAS between materials, within a material segregation can have a sufficiently minor effect between regions of a sample, and that results from the surface can in at last some situations be taken as a good approximation to bulk SDAS.

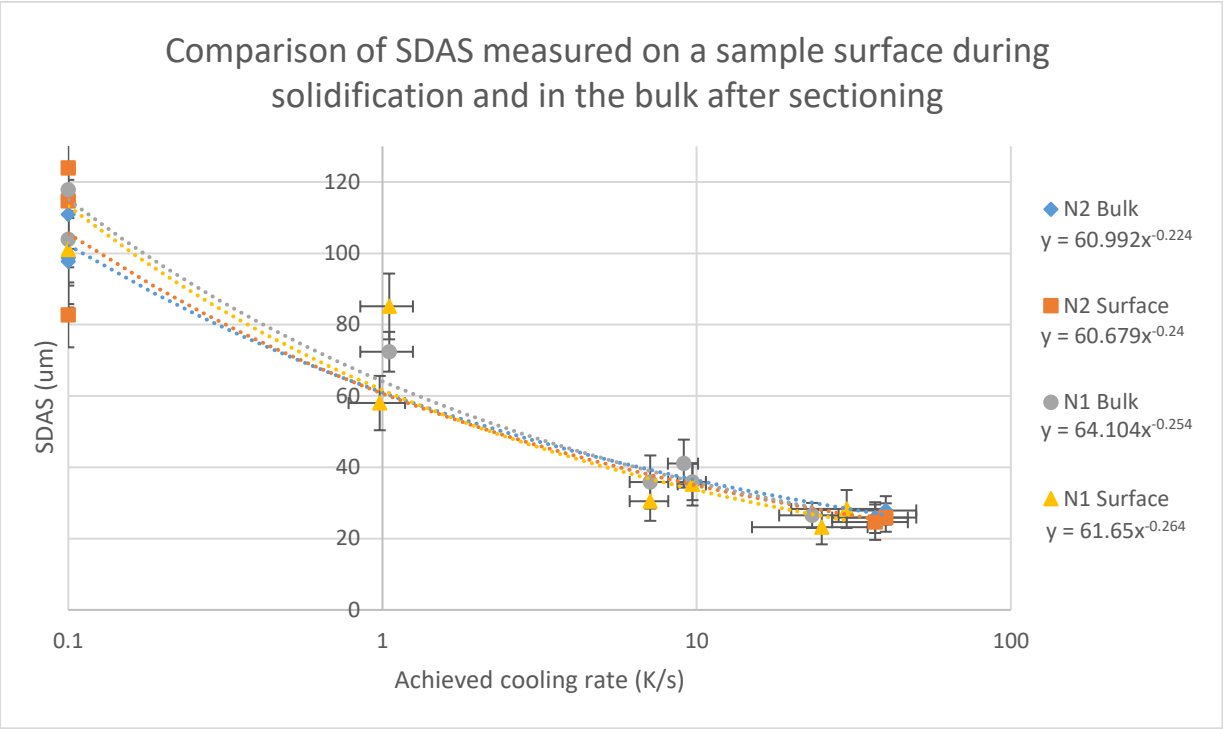

Figure 67 Comparison of SDAS with cooling rate for high Aluminium steels both at the surface and in the bulk material.

It may be that since the main alloying element in these grades was Al, which only segregates weakly, the low amount of segregation makes these grades particularly well suited to this technique and that more conventional grades with greater degrees of segregation would show more deviation.
Another point of consideration is that the testing methodology used permits a much more consistent cooling rate than industrial conditions and also better than many other experimental methodologies, and since SDAS tends to be sensitive to changes in conditions throughout the experiment, the consistency of this method is another aspect that can make it useful.
Despite the limitations in observed area, and being currently untested on grades with more pronounced segregation, this methodology still shows significant promise as a new approach to better understand solidification, specifically the development of dendritic structures.

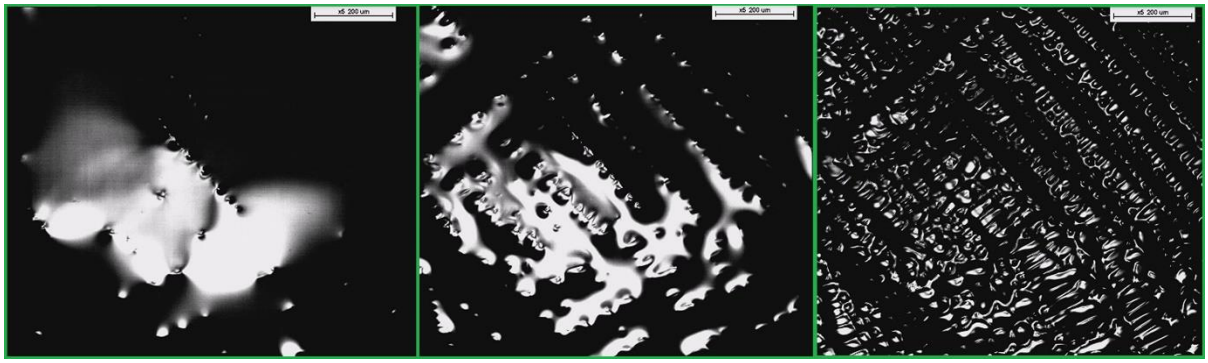

Figure 68 Progression of solidification at the surface of the Nano grade cooled at 30K/s.

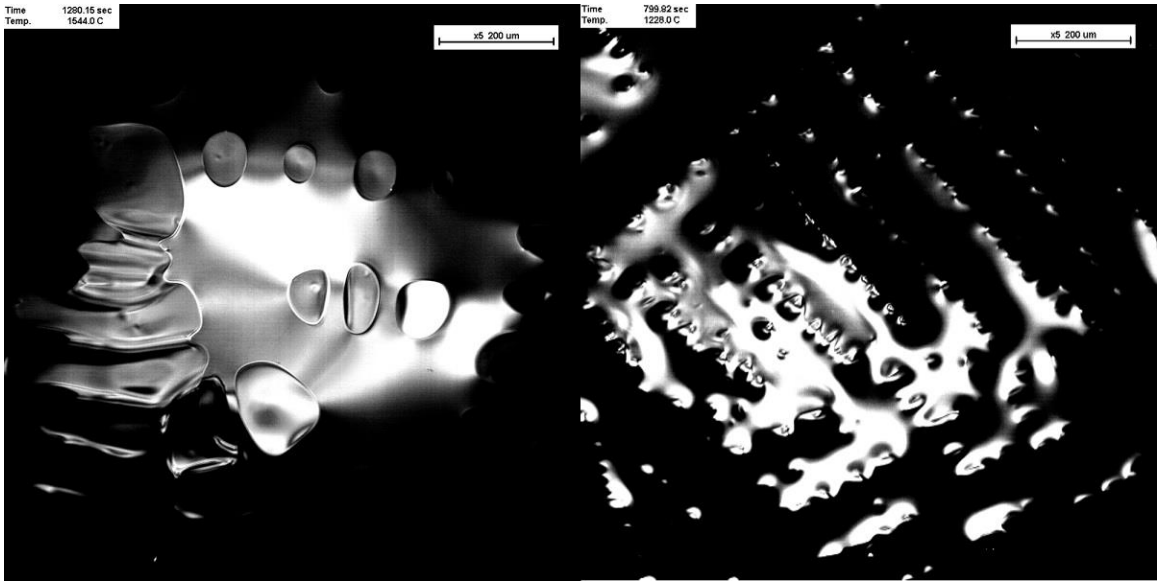

Figure 69 Steel surface during solidification of samples of the Nano 1 material, left cooled at 0.1K/s and right cooled at 30K/s.

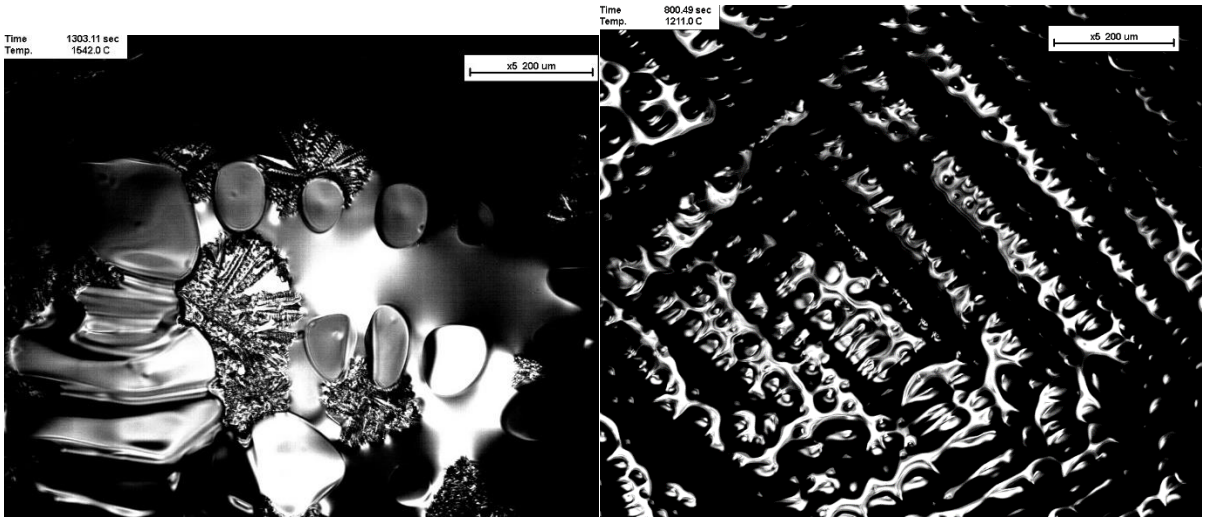

Figure 70 The same samples as Figure 69, later in solidification, it can be seen that the lowest cooling rate produces a eutectic phase while the higher cooling rate does not.

Figure 68, Figure 69, and Figure 70 provide examples of the results seen through the CLSM in situ observations, since the equipment can easily record video it is simple to later go back and make measurements on frames where the structure is most readily apparent, this is typically near the end of solidification but before further cooling has occurred. Figure 68 shows the progression of solidification for a single sample. Then Figure 69 compares the surface of the same grade at the extremes of cooling rates available in the CLSM, with Figure 70 building on this by showing the eutectic phase that was commonly seen in samples at the lowest cooling rate, but not in any of the more rapidly cooled samples.

6 MICRESS Modelling

The development of a 2d solidification model in MICRESS is described in this section. The aim was to model the solidification behaviour of the low density steels studied in the practical parts of this work; a comparison between the model and measured behaviour is reported. The model has then been used to predict the solidification structure of a different steel, a TWIP grade, and the results are compared to experimental data to consider the generic applicability of the approach. Since much of the model was fine tuned using a trial and error approach the section below discusses parameters that were adjusted in order to improve the model.

6.1 Developing the Model

The models started with default values from example code for a steel grade on the reasoning that many parameters would already be approximately suitable for this work. Then parameters were adjusted as needed to better suit the specifics of the grade and experimental conditions of the physical experiments. While some parameters such as composition and cooling rate were carefully selected, others such as spatial and temporal resolutions were adjusted on a trial and error basis. Since the cooling rates in the COMSOL model matched well with those that had been determined for the experimental samples, the MICRESS model used a similar range of cooling rates, from 1K/s, similar to the received ingots, to 150K/s, the experimental cooling rate for the thin casts. Intermediate values of 10K/s and 50K/s were also used because this matched with the cooling rates achievable in the CLSM. Based on results from the COMSOL model the thermal gradient was assumed to be double the cooling rate in each condition.

MICRESS takes material data from a GES5 file generated in Thermo-Calc, essentially this is a database of thermodynamic information for the components of the system, then other details are defined in a driving file. This lists all the required inputs, such as dimensions of the system, the position, size and orientation of any starting grains, and composition of the steel, as well as logistical concerns like resolution and which outputs to save. Sets of random grains were generated using a Matlab script to represent the initial chill zone, including size, location and orientation (see appendix 1). The Matlab script for generating the initial chill zone grain structure was verified by generating 10,000 grains and ensuring they showed a distribution consistent with the expected distribution, both with respect to the scatter of orientations and the spacing between grains. After verifying the distribution, a smaller set of grains was generated and used in all subsequent simulations. The spacing between these grains was chosen to match the spacing seen in EBSD results ensuring the initial conditions for columnar competition were as close as possible to the physical system. Since

each condition used the same set of random grains, variation in the initial orientation and spacing distribution is not a factor contributing to the differences between conditions, therefore any differences are due to altering parameters of the model, which in the final results is limited to changes in cooling rate and composition. It was confirmed that MICRESS itself is purely deterministic since repeating a simulation without changing any parameters yielded identical results. The random number generator used in the Matlab script created orientations to 3 decimal places, ensuring that neighbouring grains did not share an orientation.

The model is set up to allow wrap around on the X axis, this allows all grains to be measured and analysed by eliminating edge effects, a grain present at both ends is counted as a single grain. By using a sliding window in the Y direction that keeps pace with the most developed dendrite tip, sections that fall too far behind are no longer calculated but are still visible in the final data, this allows modelling of deep growth with a significant improvement in computation times over continuing to calculate the entire dendrite length throughout. This then allows accurate measurements of changes to grain widths with depth. However it was found that, whilst reducing computation time, this approach is not necessarily suitable for samples with a large mushy zone, since sections may be excluded from full simulation before the dendrites have grown to suitably fill the space, or in extreme cases the slowest growing dendrites may not be represented in the calculated region when they are blocked off (i.e. overgrown by faster growing dendrites), making them appear to stop growing at even shallower depths than they otherwise would. The solution to this is to increase the height of the calculated region, reducing the benefits in reduced computation time in order to allow sufficient depth for the primary phase to solidify and grow before being cut off. Figure 71 shows a short simulation to demonstrates both the wrap around effect, with the boundary between the final time step and the complete model clearly showing the same grain and the sliding window, in each intermediate step the same point in a grain appears lower in the window.

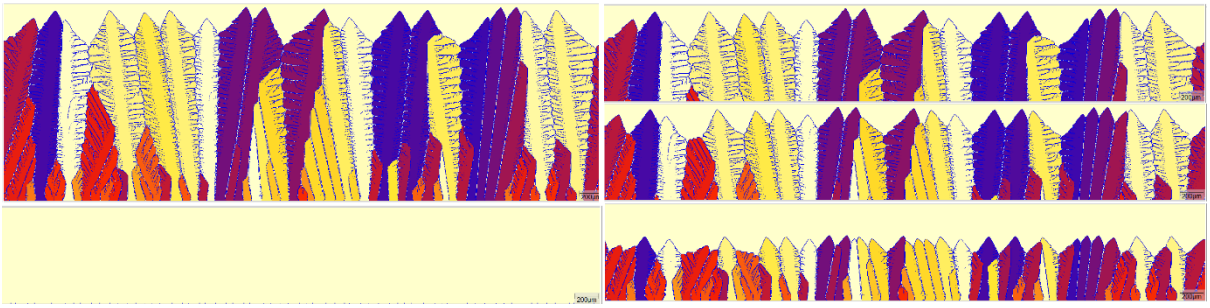

Figure 71 Shows the development of a model from starting conditions (bottom left) to the final condition (top left) with each intermediate step progressing from top to bottom on the right.

For the work presented the simulations begin at the liquidus temperature with pre nucleated grains (representing the chill zone, as described above) and use linear cooling rates. While MICRESS is capable of running 3D models, even a preliminary test with too few grains to provide meaningful data was prohibitively slow to run on a desktop computer, so this work is restricted to 2D simulations.

Table 16 shows how the compositions of simulated grades compared to the physical samples, the most apparent changes are removing trace elements in order to speed up calculation. ThermoCalc predictions for the full and simplified compositions showed that there was no significant difference in the phases produced or the temperatures of phase transitions, provided that all elements at >≈0.5% were included. The exception is Ti, which, whilst important for the final structure of the Nano grade as it forms fine scale precipitation after solidification, and as such does not affect the grain structure. The TWIP steels included here are experimental grades and only the major elements required to induce TWIP behaviour were included.

Table 16 Comparison of compositions in samples and models

Material	Mushy Zone (K)	Description	C	Si	Mn	P	S	Cr	Mo	Al	N	Nb	Ti
BH	5	Sample	0.0048	0.06	0.54	0.002	0.0005	0.58	0.01	6.98	0.0011	0.017	0.01
		Model	0.005	-	0.54	-	-	0.58	-	7	-	-	-
Nano	35	Sample	0.059	0.07	0.57	0.003	0.0007	0.52	0.02	7.12	0.0011	0.003	0.10
		Model	0.06	-	0.57	-	-	0.52	-	7	-	-	-
TWIP21	147	Sample	0.6	2.5	14	-	-	-	-	1.5	-	-	-
		Model	0.6	2.5	14	-	-	-	-	1.5	-	-	-
TWIP14	77	Sample	0.3	3	21	-	-	-	-	9	-	-	-
		Model	0.3	3	21	-	-	-	-	9	-	-	-

It was found that since the computer available for the simulations relied on having many processors rather than a few powerful processors only a limited number of grains could be modelled efficiently. To increase the number of grains considered overall, multiple intermediate size simulations were run and the results combined (8 simulations containing ≈150 grains each as opposed to a single model of ≈1000 starting grains). These smaller simulations could be run simultaneously and typically had cpu times ranging from 2000 per 0.1s of time simulated to 4500 per 0.1s, producing results much faster than the larger simulations. For conditions that gave simulations that were relatively fast a single simulation of around 1000 grains was also carried out to confirm that the results between the two methods are comparable. Such large numbers of grains are required because a significant dataset is

required after most grains have been eliminated by competition. Each of these smaller sections was 5mm across so the number of cells was rescaled based on the size of each individual cell with 4µm seeming sufficient for the high Al grades, but this was refined to 2µm for the TWIP grades. The height of each simulation was not set in advance, a scrolling window was used to allow the dendrites to keep growing as far as they could in the time allocates, and the height of this window was determined by the shortest window that would not risk removing dendrites by them falling off the bottom of the window and for the low density steels a height of 1.6mm was used.

Additionally, modifying variables with a significant impact on simulation run time allowed improvements in efficiency see Figure 72. The two variables used here were cell size (resolution) and minimum phase fraction. Increasing the minimum phase fraction in a cell sped up the final stages of pores closing far behind the solidification front, eliminating surface area that was no longer important to grain competition or growth, changing from the default $1*10^{-4}$ to $1*10^{-2}$ gave a 5-10% performance increase. While increasing the cell size obviously reduces the number of components that need to be calculated, doubling cell width from 2 microns to 4 microns gave around a 70% improvement in simulation speed. Combining both of these gave around an 80% improvement in computation time (Figure 73) without a meaningful impact on the grain distributions. There were some variations in exactly which grains were favoured, but the number of grains and range of orientations remained within expected scatter, which can be seen in the strong similarity between all 4 conditions in Figure 72, which also shows the scale bar at the top of each simulation, showing which colour correlates to which orientation.

Additionally varying the size of the starting nucleation points was looked at, the main reason for this was that with conditions starting close to the liquidus, in simulations with low cooling rates very small (single pixel) grains had a tendency to melt back into the liquid. The minor influences of this change are also looked at in Figure 72. This gives confidence that increases in grain size for later simulations with low cooling rates and resolution, in order to prevent remelting did not otherwise skew results.

In order to minimise computation time the option to approximate to a 1D concentration field far from the solidified material was also used and due to the large size of each individual cell this distance was reduced to 10 cells.

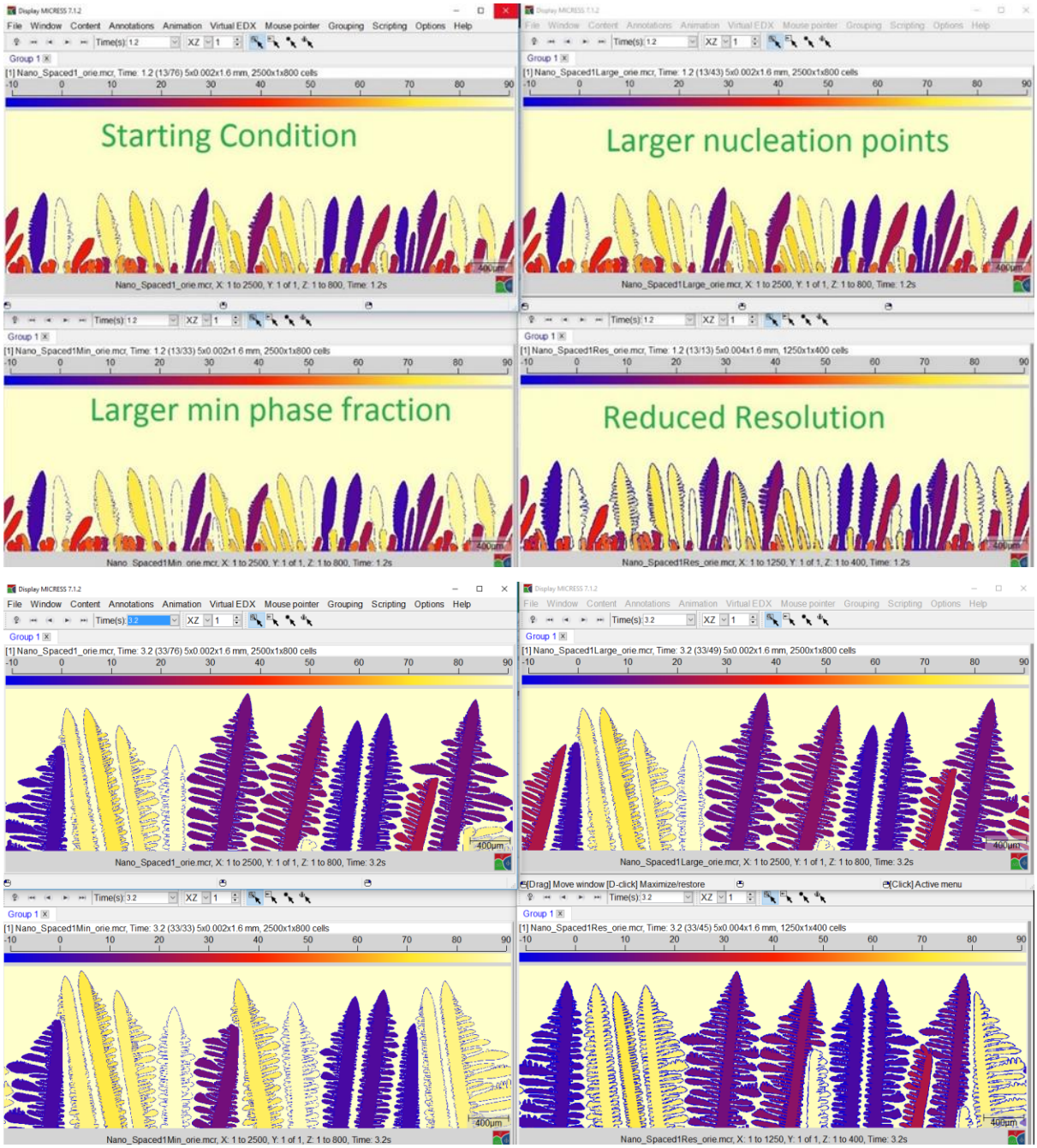

Figure 72 While different optimisation approaches did lead to different grains outcompeting others, the overall structure remains similar throughout solidification for all approaches, the bottom four images are at a later time step than their corresponding image in the upper set.

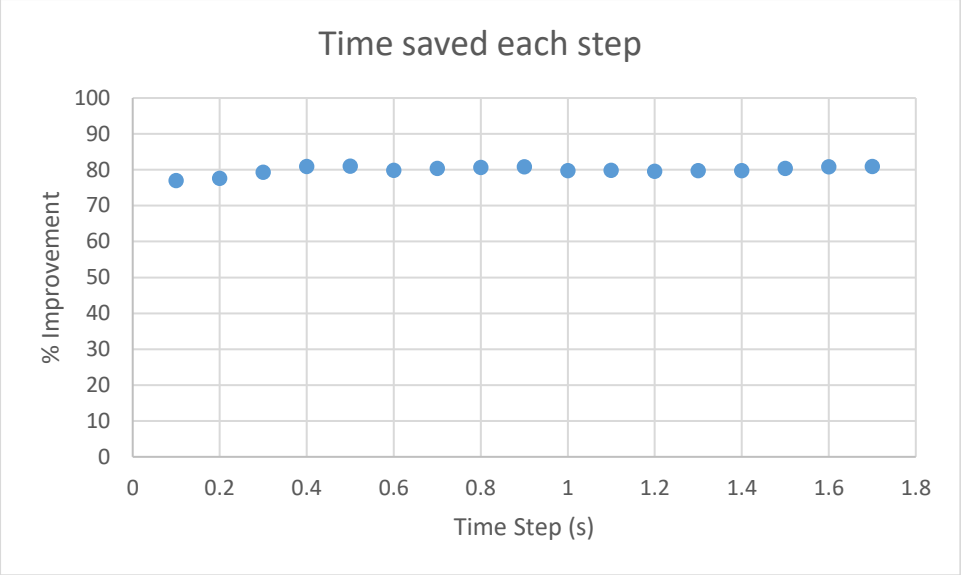

Figure 73 Percentage reduction in each time step for applying both efficiency improving changes opposed to neither.

Upon further analysis it was found that while the results from the models were within the same range as experimental results, the elimination of unfavourable grains was too linear with depth compared to the physical system. This was attributed to the distribution of orientations used in the initial grains from the Matlab script. The 2D model used a linear distribution where as in a physical system the number of grains within a given orientation range is proportional to an area, meaning that misaligned grains are more common than in the linear approximation.

Figure 74 shows the frequency of minimum misorientations of a random distribution from a reference orientation, after accounting for cubic symmetries. A simplified distribution function was created to represent the two regions (<45° and >45°). The grain generating Matlab code was modified to include these functions and to output percentiles which were passed through the inverted cumulative distribution function. Grains were also randomly assigned misorientations to be positive or negative and fit in the range $-45° \leq \theta \leq 45°$, giving the 2D model a distribution of grains that more closely approximates the distribution found in a full 3D system. The initial spacing of 'chill zone' grains was also modified from the first simulations, where experimental data from the observed chill zone was used. The modified approach used the number of grains within an orientation range at deeper points in the material (within the columnar region) then based on the expected proportion of random grains falling within that range, this density can be multiplied up to get an estimate of the total grain density.

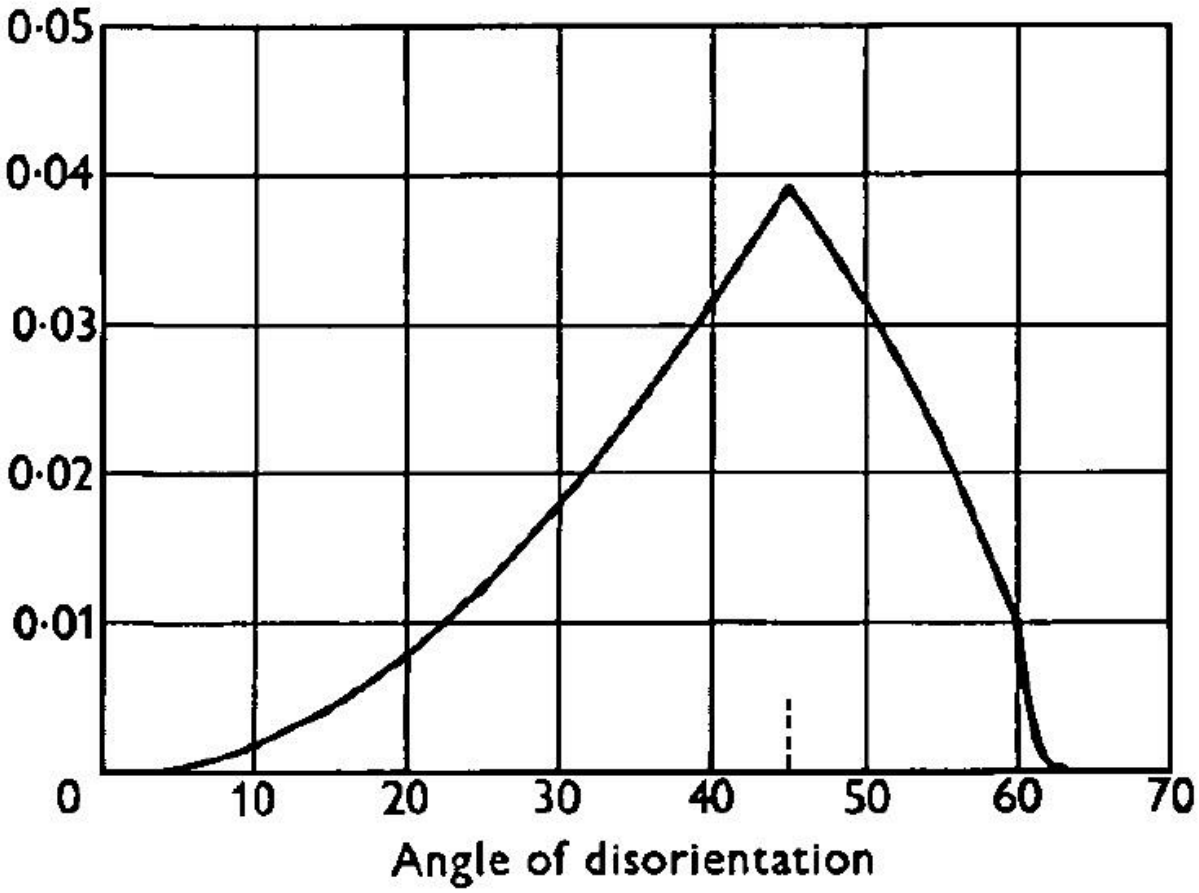

Figure 74 Frequency distribution of minimum rotations to return from a random orientation to a specified orientation in a cubic system. (Mackenzie 1958)

Observing how the primary phase develop in these models suggests explanations to why a slower cooling rate leads to more aggressive elimination of unfavourably oriented grains. Since the system being modelled has no source of continued heat input or moving parts, and cooling is happening entirely based on thermodynamics, the thermal gradient will change with the cooling rate. Due to the difference in relationships between cooling rate and each of mushy length and SDAS, unfavourably oriented dendrite tips lag less compared to the favourable dendrite tips, making overgrowth less likely and allowing a wider selection of dendrite orientations to survive deeper into the material. While a slower cooling rate elongates the mushy length, causing a greater distance between the tips of well aligned and poorly aligned grains and making it easier for the well aligned grains to out compete the poorly aligned grains. These observations are expanded upon below.

6.2 LDS model results

Figure 75 shows the development of the structure for both LDS grades at the extremes of the studied cooling rates. It can be seen that the Nano grade, which has a wider mushy zone has more

interdendritic liquid than the BH grade for the same conditions, seen as gaps between the dendrites at the lower cooling rate and the more defined dendritic structure at higher cooling rates. For each material, the SDAS becomes too fine for to resolve clearly for the higher cooling rates at the resolution used, but the primary dendrites are still visible in the Nano grade, and can be extrapolated in the BH grade from the uneven boundaries between grains. This suggests that the work would have benefited from a finer resolution at higher cooling rates. The increase in interdendritic liquid is due to the increased mushy zone in the Nano steel (due to compositional differences to the BH grade) causing the same thermal gradient to have a longer mushy length. It is also clear that structures are coarser at lower cooling rates (i.e. at the top of the images there are fewer grains (different colour regions) for the 1 K/s than 150 K/s simulations).

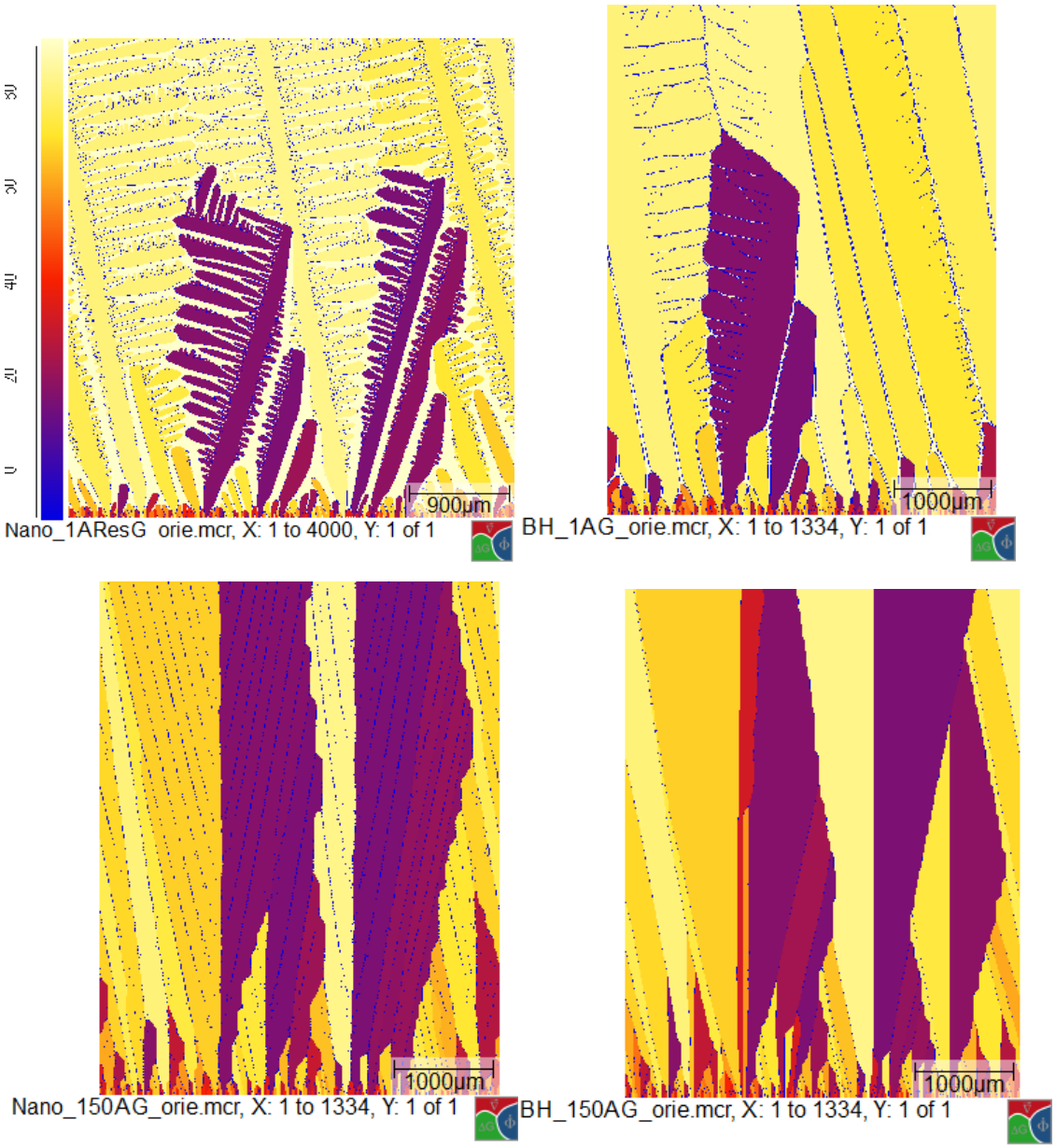

Figure 75 Grain structure during the early stages of models for both the Nano (left) and BH grades (right) at 1 (top) and 150 (bottom) K/s. Note that the initial 'chill zone' nucleating grains can be seen at the bottom of the images.

Figure 76 shows a complete simulations of the Nano grade at both 1K/s and 150K/s. Not only is the coarser structure of the slower cooling rate apparent, both on the level of dendrites and grains, but the smaller thermal gradient caused by the lower cooling rate is also visible as an extended mushy length. This is observable as both the increased distance between the most advanced dendrite tip and the least advanced dendrite meeting point and in the liquid persisting between SDAs long enough to fall out of the moving frame before solidification is complete.

Figure 77 compares the two grades under identical conditions 0.2s into solidification, this figure highlights the wider mushy zone giving a longer mushy length, manifesting as a less even top surface, as well as interdendritic liquid persisting further behind the leading tips in the Nano grade. The Nano grade also lags behind the BH grade slightly, due to the wider mushy zone meaning that the solid phase fraction increases more slowly behind the liquidus. Figure 78 shows the same systems after being allowed to develop further, at this point the lagging of the Nano grade compared to the BH grade is no longer apparent because the mushy length is small compared to the total growth length. But with the increased growth length differences in grain shape from the morphology seen in physical systems (for example shown in Figure 42 the grain competition chapter) are becoming apparent. Without the complexities of a physical system, such as a third dimension allowing grains to grow in and out of the observed plane the boundaries are far straighter than is typically observed in a physical system.

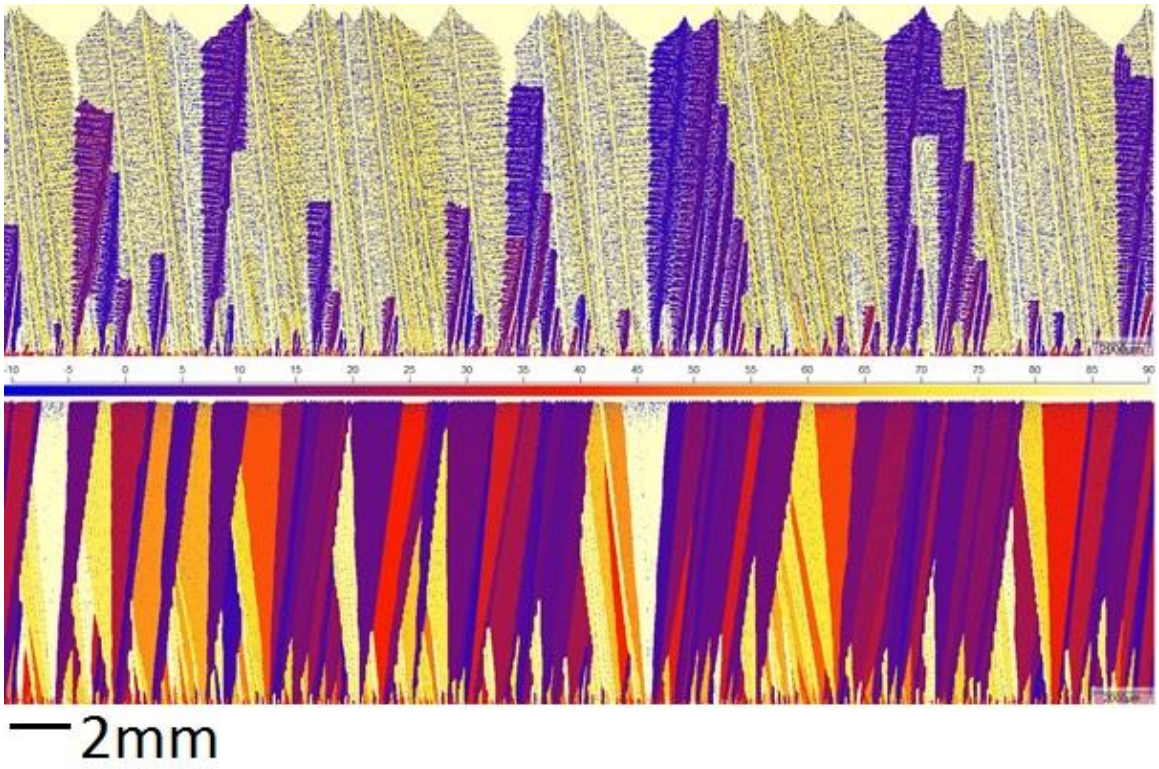

Figure 76 Nano models cooled at 1K/s (top) and 150K/s (bottom).

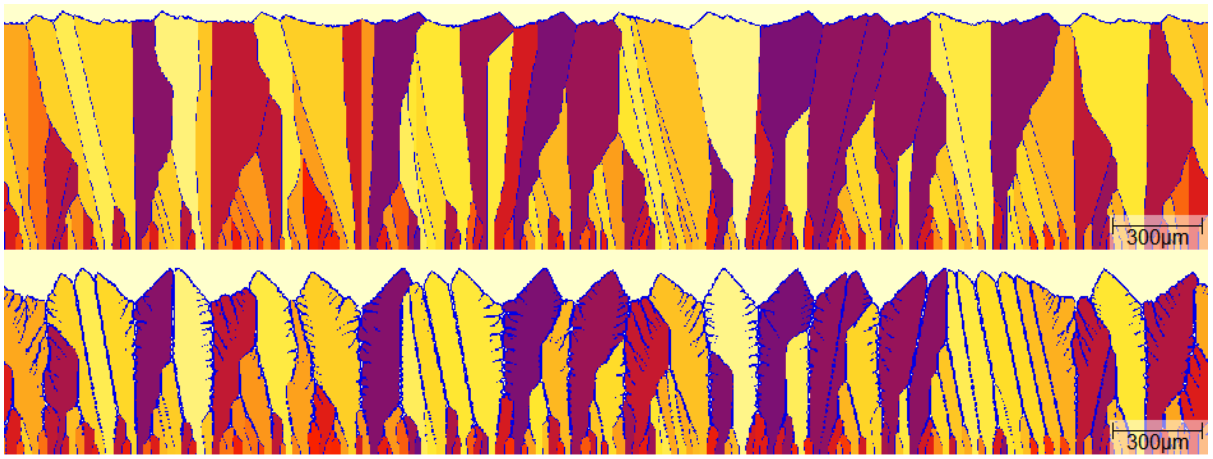

Figure 77 BH (top) and Nano (bottom) grades cooled at 150k/s after 0.2s

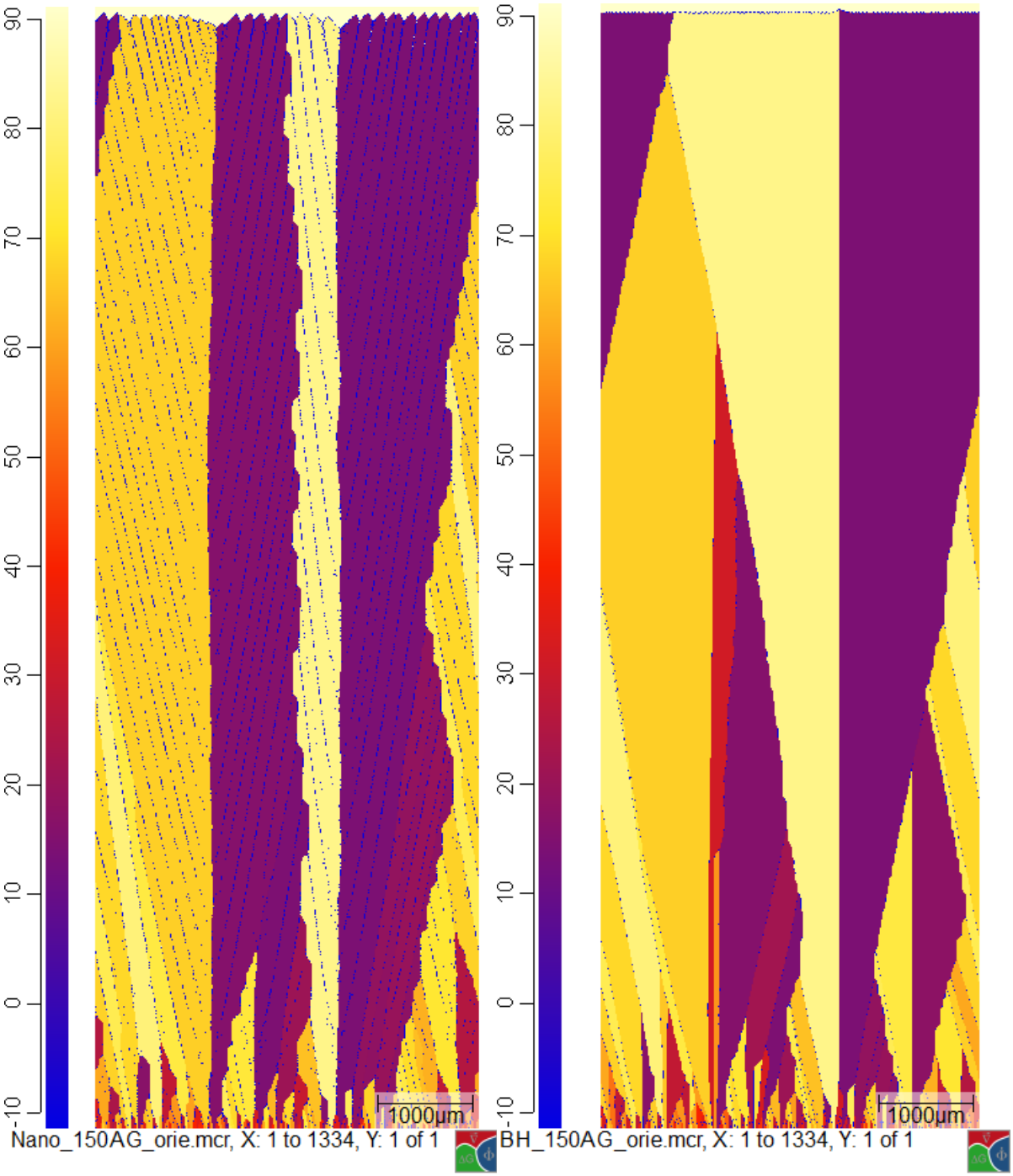

Figure 78 Comparison of each grade under otherwise identical conditions with a cooling rate of 150K/s after 2.4s.

6.3 Comparison to experimental results

Figure 79 shows the variation of columnar zone with depth, contrasting both cooling rates measured experimentally plus models with similar cooling rates. Models that use a single large region are also compared to combined data from several smaller regions (as discussed earlier in this chapter. These results show that the smaller simulations can be combined to give equivalent results to running a single large model, this is useful for running simulations faster. The blue lines, which are the lower

cooling rate conditions also show that despite several refinements to the randomisation of grain orientation and spacing there is still some discrepancy between the model and experimental results. Two possible reasons are suggested: first is that the collapse from 3d to 2d reduces the number of neighbours a grain can have, essentially slowing competition when many grains are present. The second is that it also prohibits the rotation of secondary dendrites around the primary axis, which (Liu et al. 2013) found to be an important factor when grains were converging. This may explain the fast coarsening of grain width seen experimentally than in the models. However, the difference due to cooling rate is clearly seen in the model results with much fast coarsening for the lower cooling rate systems.

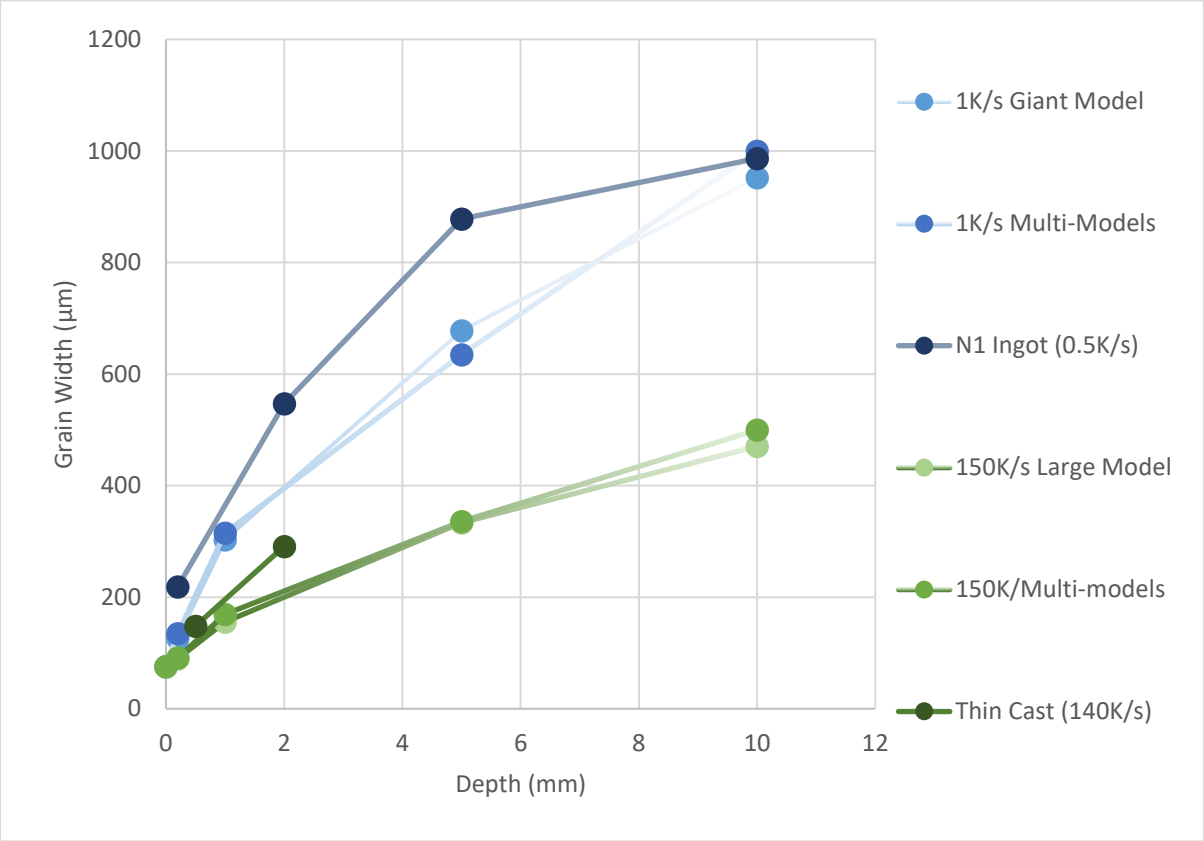

Figure 79 Variation of grain width with depth through the columnar zone for the Nano 1 steel

Comparison of SDAS between experimental results and MICRESS models for the Nano grades gave mixed results. At a cooling rate of 150K/s dendrite arms tended to be very short and impede on other grains rapidly, these gave a SDAS of around 35µm, about double the experimentally observed value for similar cooling rates. For lower cooing rates (1K/s) the secondary arms had a greater length to grow, leading to competition and elimination between the secondary arms, if measured immediately adjacent to the primary trunk these gave a similar value to higher cooling rates, 40µm, however if measured further from the trunk only including branches that survive long enough to be

blocked by a different grain then the spacing is around 70-75µm, which is closer match for the experimentally observed results in similar conditions (60µm for 1K/s CLSM experiments and 70µm for 0.6K/s ingots as received from Tata.

6.4 Predicting TWIP results from the model

The behaviour seen in the model of the BH grade compared to the Nano grade compares well with comparison to experimental results between the grades. Notably, the structure is much more cellular as opposed to dendritic, which correlates with the CLSM results where dendritic structure were much harder, or impossible to observe during solidification. And the grain sizes are larger than the Nano grade under the same conditions.

To determine how generically applicable the model is it was tried with a very different steel grade (TWIP steel which solidifies as austenite compared to the LDS which solidifies as delta ferrite – both cubic structures). To run the simulation the composition in the model was modified to a TWIP grade, shown up in Table 16, but the 'chill zone' grain structure was kept constant to maintain constant nucleation conditions.

The model of the TWIP21 grade solidified at 150K/s gave a SDAS of around 20-25µm, the experimentally determined value was 13µm, so similar to the nano grade cooled at 150K/s the values predicted by MICRESS were approximately double the experimentally determined values. This may be a consequence of the cooling rates in the experimental parts of this work being average cooling rates, and because the cooling is passive it will be a curve that asymptotically approaches room temperature. Meaning that the high temperature behaviour is only approximately linear and different parts may be above or below this rate.

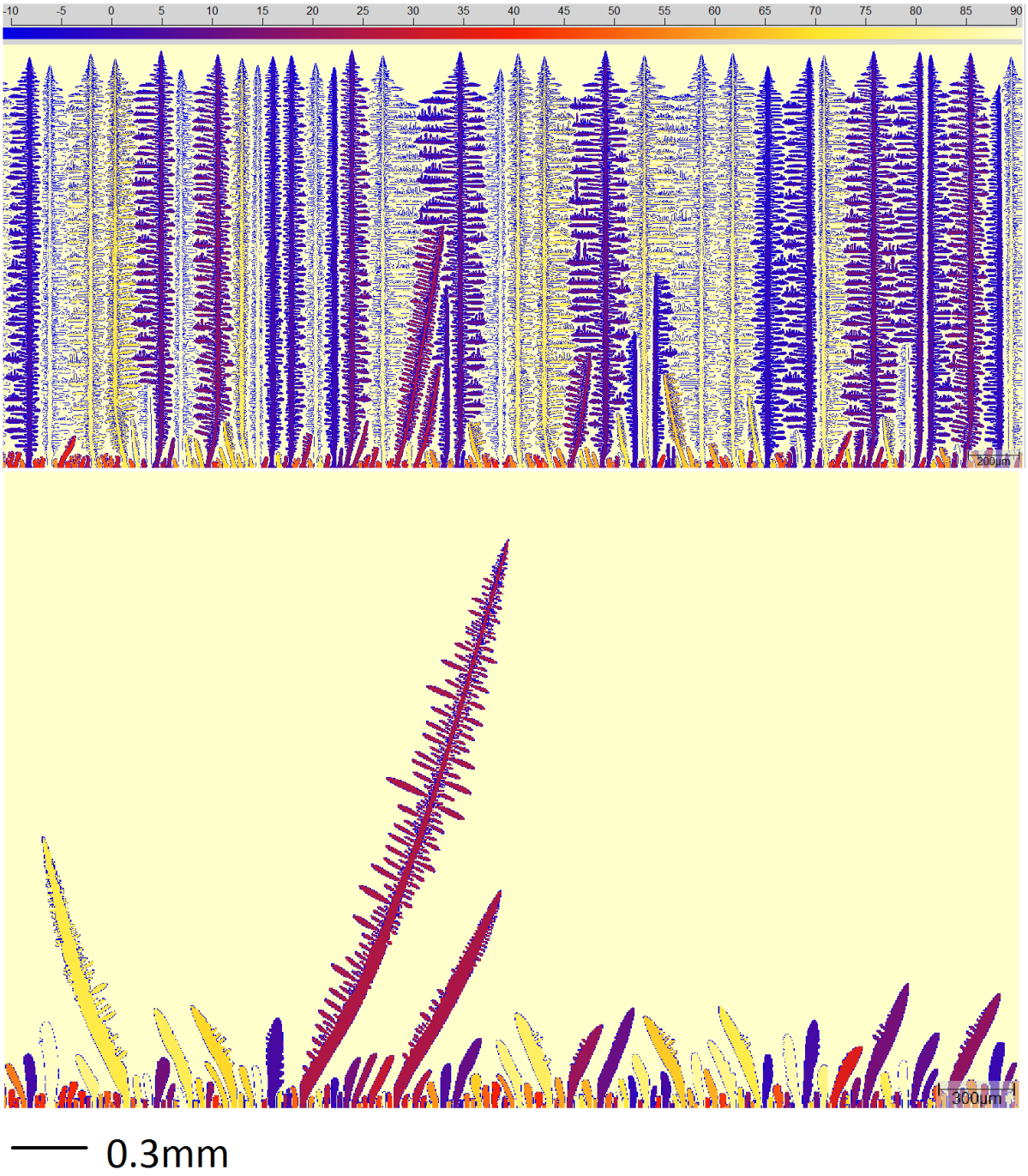

Figure 80 TWIP21 models with cooling rates of 150K/s (top) and 1K/s (bottom)

The TWIP models were much more computationally intensive than the LDS models, resulting in much longer run times this was due to both an increase in resolution to better deal with the finer structure and the increased height needed to keep all of the solidification range in the calculated window. The early stages of simulations are shown in Figure 80. The most notable feature here is several dendrites in the 1K/s condition that are growing far ahead of the rest, and that it has a misorientation of around 15-25°, more than expected from the LDS work. The degree to which a small number of grains (and 1 in particular) are outpacing the rest likely hint at an instability in the

model, but this still provide a useful contrast to other models and to experimental results. Such as the dendritic structure at high cooling being far finer and more pronounced than the LDS grades shown in Figure 77 and for the lower cooling rate, even ignoring the 3 grains that stand out most, the rest are showing a larger range of depths, both of these are consistent with the wider mushy zone.

However this actually ends up matching with the EBSD map (Figure 81) for this grade, which shows a much weaker selection effect, with many grains in the 15-30° range surviving to depths where they had been eliminated in the LDS grades. This further supports the idea that less well aligned grains survive to greater depths with a longer mushy length, as discussed in section 5.2.10.

Figure 81 Shows EBSD maps of the two TWIP grades studied. TWIP14 is belt cast, with its chill zone on the right hand side and the equiaxed zone on the left, it had a low cooling rate ≈5K/s. TWIP21 was laboratory belt cast simulated at McGill University with the left hand side in contact with the belt and the right exposed to the atmosphere, with a much higher cooling rate of ≈ 150K/s being seen for the initial solidification close to the belt. A band contrast image of the TWIP21 grade belt cast microstructure clearly shows the dendritic structure, allowing measurement of SDAS to additionally compare the SDAS:mushy length ratio to those obtained for the LDS grades, shown in Table 17; dendrites were not visible in the TWIP14 grade. IPF contour plots for these cast structures (Figure 82) show a wider range of persisting orientations than in the LDS casts (see Figure 57), which fits well with the trend seen in the modelling results where a larger range of orientations were able to grow ahead of their neighbours than in the LDS grades.

The idea of a correlation between the ratio of SDAS and mushy length (the physical distance between the first solidifying material and last solidifying material in a solidification front, as opposed to the mushy zone which is the difference between the solidus and liquidus temperatures) developed because a major factor in competition between grains is secondary dendrites growing out and blocking off grains that are lagging behind the solidification front. The speculation is that grains of a given misorientation will be in steady state with the solidification front at a fixed percentage of the mushy length, thus a short mushy length will offer little opportunity for overgrowth while a longer mushy length will increase the probability of a given well aligned grain blocking off a poorly aligned grain. Building further on this idea, if the SDAS is large compared to the mushy length then the secondary arms will develop further behind the solidification front while a shorter SDAS would lead to secondary arm growth closer to the dendrite tip and to the solidification front, meaning that a smaller SDAS should increase the rate of elimination of poorly aligned grains by making overgrowth easier while a large SDAS will lead to secondary arms developing when poorly aligned

grains have already grown past them. The SDAS:mushy length ratio is then an attempt to consider both these factors as a single parameter.

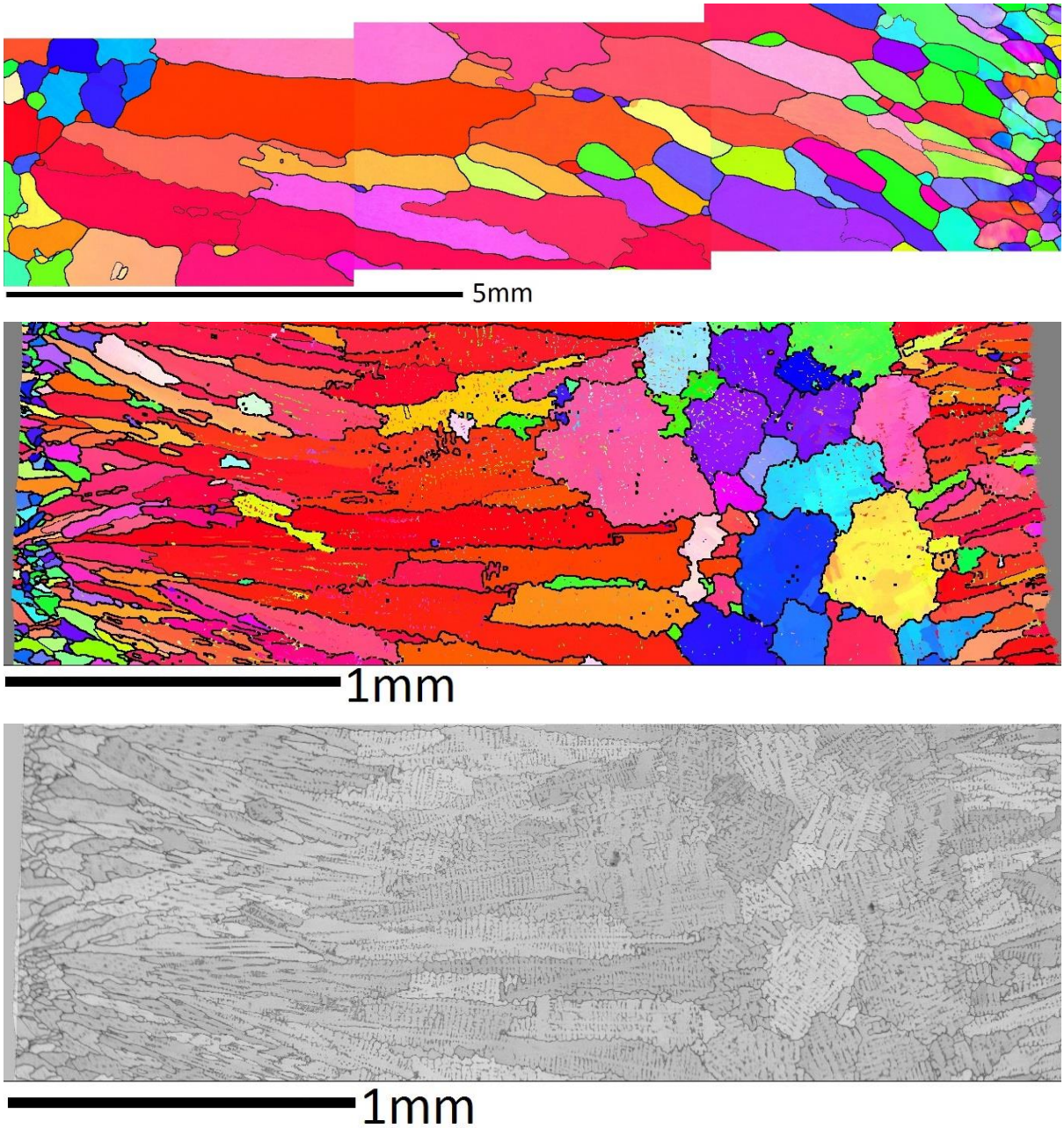

Figure 81 EBSD map of the TWIP14 grade (top) and TWIP21 grade (middle), and a band contrast image of TWIP21 (bottom) which more clearly highlights the dendritic structure. The solidification direction is horizontal with the chill zone being evident on the right hand side of TWIP14 and the left hand side of TWIP21.

Since the coarsening behaviour of the ingot and 15mm casts were within experimental error of each other, and the SDAS:mushy length ratio for the TWIP grade is only just outside the bounds of these conditions then the hypothesised relationship predicts that there will at most be a small reduction in coarsening rate compared to the ingot and 15mm conditions. The ratio between SDAS and mushy zone is an interesting perimeter to consider since mushy length is a factor of thermal gradient, while

SDAS is determined by temperature and as such is a combination of the cooling rate and kinetics of solidification. While cooling rate and thermal gradient are correlated in static systems without additional heat input, this means that the mushy length and the SDAS will have different sensitivities to changes in solidification conditions.

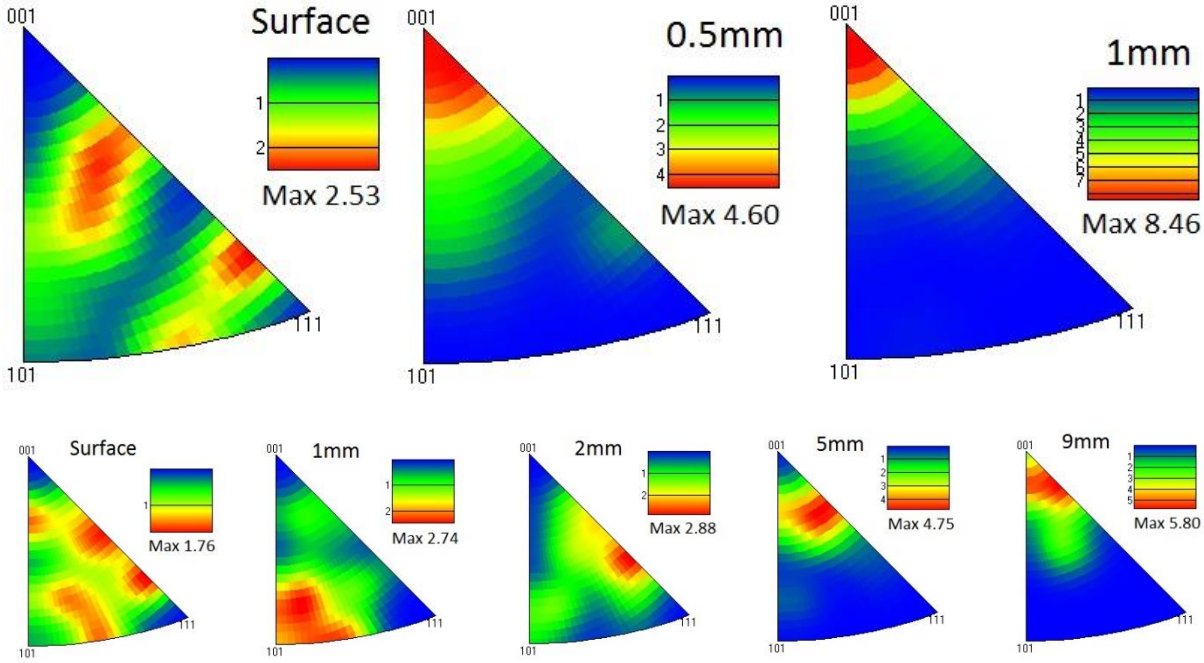

Figure 82 IPF contour plots through the columnar zone of the TWIP21 grade (top) and TWIP14 grade (bottom)

Figure 82 shows contour IPF plots through both of the TWIP steels, while the difference in cooling rate and composition means they are not directly comparable, the higher cooling rate for TWIP21 shows far more aggressive elimination of unfavourable grains than the lower cooling rate seen for TWIP14. Indicating that the hypothesis developed from the low density steels considering columnar width at a given depth as simply a factor of the initial grain spacing and competition levels (themselves a factor of cooling rate), is not broad enough and additional factors need to be considered in order to reliably predict the rate of coarsening through the columnar region. Since both grain and SDAS data was obtained for the TWIP21 grade, Table 17 adds this data to that obtained for the LDS casts.

Table 17 SDAS and mushy length data, with the addition of the TWIP21 grade

	Nano Ingot	Nano 15mm cast	Nano 5mm cast	TWIP21
Cooling rate (K/s)	0.6	10	150	150
Mushy Length (µm)	26000	1600	110	440
SDAS (µm)	70	35	18	13
SDAS % of mushy length	0.27	2.2	16.4	3

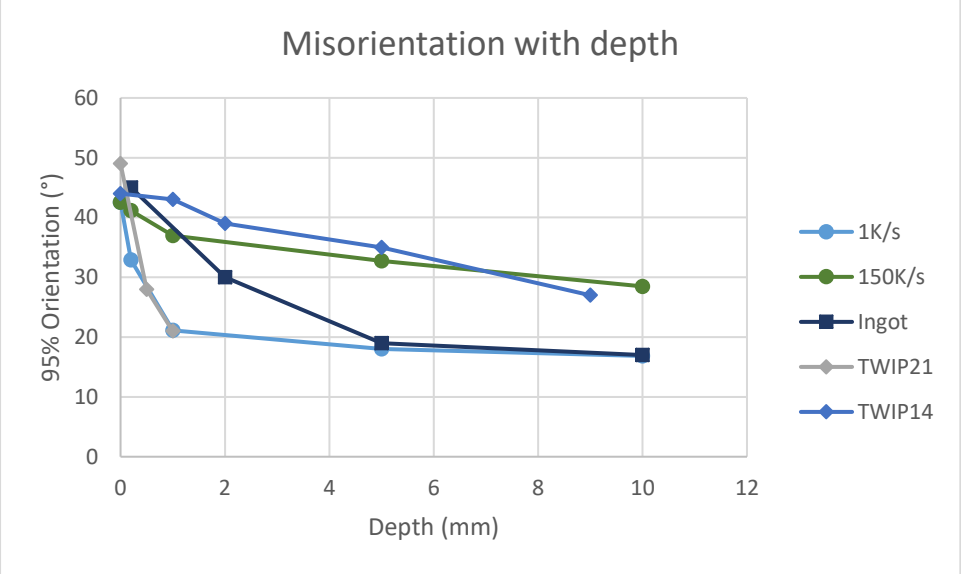

Figure 83 Adding the TWIP grades to the analysis of misorientation with depth for the Nano grade (Ingot) and two cooling rates of the Nano model. The angle range that includes 95% of grains is considered to exclude outliers.

Figure 83 adds the TWIP grades to the analysis of changes in maximum misorientation with depth, and the behaviour of the TWIP21 grade, which had a SDAS:mushy length ratio close to the insensitive region of the ingot and 15mm cast, closely followed the trend of the 1K/s model, and showed noticeably more aggressive elimination than the experimental results for the ingot. The more gradual elimination seen in the TWIP14 grade suggests the SDAS is a significantly larger fraction of the mushy length. A plausible explanation for this is the starting grain size, the TWIP21 grade had a fine chill zone while the TWIP14 grade had a much coarser chill zone and that considering depth as a function of the starting grain spacing, plotted against the maximum misorientation may show trends that are more consistent between materials.

7 Conclusions

Low density steels (LDS) are of interest as a potential material for automotive panels as they have excellent strength to weight characteristics. However, they are difficult to process due to their tendency to form large grain sizes on solidification. In this work solidification studies to investigate the effect of cooling rate on the secondary dendrite arm spacing (SDAS) were carried out using a confocal laser scanning microscope (CLSM) and studies into grain size were performed with ingot casting. Subsequent trials were then carried out with LDS grades to determine the influence of composition and cooling rate on the SDAS and solidification grain size in these materials. The ingot casts covered cooling rates of 0.6K/s up to around 150K/s and detailed analysis of the grain size development was performed by obtaining large scale EBSD maps of the samples. This was followed by modelling work in MICRESS aiming to replicate the structures in the LDSs then predict the structure of other grades.

7.1 Accademic and scientific

A summary of the output of this work related primarily to the academic approach and fundamental understanding.

- The CLSM allows for observation of solidification in situ on the surface of the material, showing SDAS development.
- Doping the samples with a small amount of Ta was found to reveal the dendritic structures in the bulk material using conventional techniques, without having a significant impact on the scale of SDAS. This allowed comparison between the surface in-situ observations and bulk measurements.
- Comparing the bulk SDAS to surface SDAS measurements showed that this technique produced results representative of those obtained using more conventional methods. This approach provides a new technique for obtaining the solidification structure of grades that are unsuitable for conventional techniques.
- The coarsening of grain structure was observed with increasing depth through the columnar zone, with an associated reduction in the range of grain orientation for both LDS investigated and for all cooling rates.
- The rates of grain elimination and misorientation reduction showed the same trends of rapid change near the surface but then slower change at greater depths. This indicates that grain growth competition was the significant factor, neither additional nucleation or post solidification grain coarsening significantly influenced the structure.

- Grain elimination is initially rapid but slows down as solidification progresses, and levels off, indicating that there is a stable orientation range where grains cannot grow far enough ahead of neighbours to outcompete them.
- The thinner casts, with higher cooling rates, suggested a more gradual elimination of misaligned grains than the larger, slower cooled ingots. These casts were too narrow to achieve a steady state so it is unclear if the grain sizes would level out at a different misorientation range.
- The difference in competition behaviour suggested two relationships that were tested later, one was a correlation between the cooling rate and the misorientation range at a given depth, and the second was a relationship between the SDAS:mushy length ratio and the rate at which the range of orientations is reduced.
- There appears to be a correlation between the misorientation range with depth and cooling rate. Under this model grain size through the columnar zone is purely a factor of the nucleation grain spacing and the rate of cooling, with a slower cooling rate leading to more rapid elimination of poorly aligned grains.
- Considering competition and misorientation ranges with depth as a function of the SDAS:mushy length ratio, this factors in composition both as in influence for nucleation spacing and on competition itself, it also uses microstructural and thermodynamic properties in order to explain variation in later grain growth. This hypothesis is that competition between grains is more intense when the SDAS is small compared to the mushy length, and slower when the SDAS is relatively large. The proposed mechanism being that with a smaller SDAS, dendrite arms can more readily block off neighbouring grains, and a longer mushy length allows more opportunity for the leading grains to develop dendrites that block off lagging grains.

- Results in MICRESS did not exactly match experimental results, but showed the same trends between cooling rates and materials, suggesting the current model can make qualitative predictions, but further improvement is needed to be able to make quantitative predictions.
- It is unclear how much further improvement is possible of a 2D model and how much of the limitations are inherent to a 2D simulation of a 3D system.

- The hypothesis relating columnar zone competition to cooling rate did not translate when applied to very different steel composition (TWIP steel that solidified as austenite compared to the LDS which solidified as delta ferrite).

- The hypothesis relating competition to SDAS:mushy length ratio was consistent with additional results from the TWIP grades, suggesting this correlation is worth further study.

7.2 Industrial applications

Since many of the outcomes of this work are focused more on the scientific questions, direct application to industry is limited.

- The CLSM methodology is suitable for confirming the scale of dendritic structures predicted by simulations of novel grades, even if the composition hinders conventional microstructure assessment techniques.
- Recrystalisation options are limited for single phase high Al steels due to their crack susceptibility and lack of renucleation from phase changes so further research into these grades should probably focus on twin roll casting as this has the highest cooling rate and produces the thinnest sheets.
- The proposed relationship between SDAS and mushy zone length could lead to models that are better able to better predict the microstructure in novel compositions.

8 Further work

This work leaves open several avenues of further research;

On the academic side one if these is further CLSM SDAS observation to find out how broadly applicable this technique is. This work carried out demonstrated it is reliable for the LDS grades that were studied, but further steel grades and alloys of other metals would further demonstrate the value of this technique. This work also provides useful data to understand the development of solidification structures, particularly in steels that undergo transformation following solidification sand consequently lose their solidification structure.

While it was not noticed in this work, another potential avenue of work based on the CLSM is to investigate dendritic coarsening. An obvious cause of problems here is that prolonged periods at high temperatures will make atmospheric control to minimise oxidation and other contamination from the air even more vital. Additionally since the dendrites are visible on the surface, this suggests that the dendrites protrude slightly from the interdendritic regions. This means effects of the solid-gas interface may influence the coarsening behaviour on the surface and it will need to be confirmed if the surface results are representative of coarsening in the bulk of the material where the solid-liquid interface has relatively minor compositional changes.

Another is further development of the MICRESS model, either by making further adjustments to the 2D system such as including predictive capability for nucleation (using a model for nucleation density related to composition and/or mould surface, although limited work in this project has indicated that mould surface has little influence on nucleation). Or using a time dependant cooling rate, which would give better simulation of actual casting conditions. The limitations identified in this work and in the literature for grain competition related to the 3d geometry and growth of dendrites means that extension of the model to 3d would be beneficial.

There is also an avenue to further explore the relationship between the SDAS:mushy zone width ratio and the range of grain orientations that is stable, as well as how this impacts the rate of competition. Since this work provides a partial data set for the TWIP grades, they would be an ideal material to use for this, but if the trend can be applied more broadly then any single phase steel should work, if that proves robust then determining if the relationship varies for different metals or is universal would be a valuable further expansion.

Additionally, while work on the TWIP steels did go against the hypothesis of the coarsening rate being determined by cooling rate, normalising length measurements in terms of the initial grain spacing rather than absolute measurements may also be worth pursuing.

9 Appendices

9.1 Appendix 1 Defining a grain

Lines beginning with a # are comments to aid with understanding and debugging the code, descriptions of the grains position, morphology, phase, and orientation are all readily apparent.

```
# Input data for grain number 1:
# Geometry?
# Options: round rectangular elliptic round_inverse
round
# Center x,z coordinates [micrometers], grain number 1?
30.9011
1.00000
# Grain radius? [micrometers]
2.00000
# Shall grain 1 be stabilized or shall
# an analytical curvature description be applied?
# Options: stabilisation analytical_curvature
stabilisation
# Should the Voronoi criterion be applied?
# Options: voronoi no_voronoi
no_voronoi
# Phase number? (integer)
1
# Rotation angle? [Degree]
36.5213000000000
```

9.2 Appendix 2 The effect of cubic symmetries

Developing this model required a greater understanding of the distribution of orientations in 3D space than the practical aspects, which is summarised here in order to explain some choices made during developing the model.

Steels typically solidify as either ferrite, which has a body centred cubic structure, or austenite which has a face centred cubic structure, although other structures such as martensite can be formed during solidification or cooling. So again this work will only look at cubic symmetries since the steels studies only contain cubic structures.

Due to restrictions imposed on crystal lattices, the cubic structures show the greatest assortment of symmetries of any possible 3d crystal (Tilley 2007), specifically there are 24 equivalent orientations (and another 24 in a more abstract sense that also considers reflections). Starting with a cube and

picking an axis passing through the centre of two opposite faces, there are 4 rotations around that axis that return to an indistinguishable state. Then this process can then be repeated after a rotation to switch to any of the 6 faces (each of these transformations can be performed in a single rotation as in Table 18, but these descriptions make it less clear that the end result is equivalent to the starting orientation, or that all possibilities are exhausted).

In two dimensions it is easy to picture a square, being the same after a rotation of 90°, can never be more than 45° away from a specified orientation. However in 3 dimensions the additional degrees of freedom mean that it is difficult to intuitively understand the system and some simple trigonometry is required to work out the maximum possible deviation. The maximum deviation of a direction from the axes of the cube will be a line connecting opposite corners of the cubes body. Taking a unit cube, first rotate such that only a plane including the body diagonal and one of the edge axes needs to be considered. This gives a right angle triangle with sides of lengths 1, √2, and √3, it is then easy to calculate the angle between axes and the maximum misalignment as 54.7°. If rotations around the axes are also considered the maximum misorientation is then 62.8°. Meaning that for any arbitrarily misoriented cube it is guaranteed that a single rotation of no more than 62.8° can (when the axis is suitably chosen) transform the arbitrarily rotated cube to one of the 24 orientations symmetrically identical to any chosen reference orientation.

Table 18 Single rotation descriptions of all equivalent orientations for a cube/cubic system

Axis	Rotation	Quantity
Any	0	1
<100>	90	6
<100>	180	3
<101>	180	6
<111>	120	8

10 References

2011. Bueler SumMet A guide to Materials Preperaton and Analysis. Buelher.

2018. *Computational Materials System Design*. Springer.

Access-e.V. 2018a. *Micress User guide Version 6.4*.

---. 2018b. Supplementary Information about Micress. https://web.micress.de/index_extra.html#micress-info.

Andersson, J. O., T. Helander, L. H. Hoglund, P. F. Shi & B. Sundman (2002) THERMO-CALC & DICTRA, computational tools for materials science. *Calphad-Computer Coupling of Phase Diagrams and Thermochemistry,* 26**,** 273-312.

Asta, M., C. Beckermann, A. Karma, W. Kurz, R. Napolitano, M. Plapp, G. Purdy, M. Rappaz & R. Trivedi (2009) Solidification microstructures and solid-state parallels: Recent developments, future directions. *Acta Materialia,* 57**,** 941-971.

Baricco, M., E. Bosco, E. Olivetti, M. Palumbo, P. Rizzi, A. Stantero & L. Battezzati (2004) Rapid solidification of alloys. *International Journal of Materials & Product Technology,* 20**,** 358-376.

Bellet, M., O. Cerri, M. Bobadilla & Y. Chastel (2009) Modeling Hot Tearing during Solidification of Steels: Assessment and Improvement of Macroscopic Criteria through the Analysis of Two Experimental Tests. *Metallurgical and Materials Transactions a-Physical Metallurgy and Materials Science,* 40A**,** 2705-2717.

BJJD. 2010. http://www.jd-met.com/webcontent/?pageID=95.

Borgenstam, A., A. Engstrom, L. Hoglund & J. Agren (2000) DICTRA, a tool for simulation of diffusional transformations in alloys. *Journal of Phase Equilibria,* 21**,** 269-280.

Bottger, B., M. Apel, J. Eiken, P. Schaffnit & I. Steinbach (2008) Phase-field simulation of solidification and solid-state transformations in multicomponent steels. *Steel Research International,* 79**,** 608-616.

Boultbee, E. F. & G. A. Schofield. 1981. *Typical Microstructures of Cast Metals New Revised Edition*. Birmingham: IBF Publications.

Bulent Biner, S. 2017. *Programming Phase Field Modelling*. Springer International Publishing.

Butt, H.-J., K. Graf & M. Kappl. 2006. *Physics and Chemistry of Interfaces* Wiley-Vch.

Calvo, J., J. M. Cabrera, A. Rezaeian & S. Yue (2007) Evaluation of the hot ductifity of a C-Mn steel produced from scrap recycling. *Isij International,* 47**,** 1518-1526.

Campbell, P., W. Blejde, R. Mahapatra & R. Wechsler (2004) Recent progress on commercialization of CASTRIP((R)) direct strip casting technology at nucor Crawfordsville. *Metallurgist,* 48**,** 507-514.

Carlsson, G., R. Nystrom, H. Sandberg, W. Reichelt & U. Urlau (1997) Single belt casting. A promising technique for the production of steel strip. *Scandinavian Journal of Metallurgy,* 26**,** 242-248.

Chang, Y. A., S. L. Chen, F. Zhang, X. Y. Yan, F. Y. Xie, R. Schmid-Fetzer & W. A. Oates (2004) Phase diagram calculation: past, present and future. *Progress in Materials Science,* 49**,** 313-345.

Chen, S. P., R. Rana, A. Haldar & R. K. Ray (2017) Current state of Fe-Mn-Al-C low density steels. *Progress in Materials Science,* 89**,** 345-391.

Connolly, B. M., J. Paules & A. DeArdo (2015) The effects of composition and thermal path on hot ductility of forging steels. *Metallurgia Italiana***,** 3-9.

Daamen, M., O. Guvenc, M. Bambach & G. Hirt (2014) Development of efficient production routes based on strip casting for advanced high strength steels for crash-relevant parts. *Cirp Annals-Manufacturing Technology,* 63**,** 265-268.

Ding, G. L., W. D. Huang, X. Huang, X. Lin & Y. H. Zhou (1996) On primary dendritic spacing during unidirectional solidification. *Acta Materialia,* 44**,** 3705-3709.

Djukanovic, G. 2016. Alcoa's Micromill Technology for future cars. http://aluminiuminsider.com/alcoas-micromill-technology-for-future-cars/: Aluminium Insider.

Doherty, R. D., P. D. Cooper, M. H. Bradbury & F. J. Honey (1977) COLUMNAR TO EQUIAXED TRANSITION IN SMALL INGOTS. *Metallurgical Transactions a-Physical Metallurgy and Materials Science,* 8**,** 397-402.

Du, Y., J. C. Schuster, Z. K. Liu, R. X. Hu, P. Nash, W. H. Sun, W. W. Zhang, J. Wang, L. J. Zhang, C. Y. Tang, Z. J. Zhu, S. H. Liu, Y. F. Ouyang, W. Q. Zhang & N. Krendelsberger (2008) A thermodynamic description of the Al-Fe-Si system over the whole composition and temperature ranges via a hybrid approach of CALPHAD and key experiments. *Intermetallics,* 16**,** 554-570.

Elorez, P.-S. & J. Antonio. 2017. *Solidification and Solid-State Transformations in Metals and Alloys*. Elsevier.

Emi, T. & H. Fredriksson (2005) High-speed continuous casting of peritectic carbon steels. *Materials Science and Engineering a-Structural Materials Properties Microstructure and Processing,* 413**,** 2-9.

Engstrom, A., L. Hoglund & J. Agren (1994) COMPUTER-SIMULATION OF DIFFUSION IN MULTIPHASE SYSTEMS. *Metallurgical and Materials Transactions a-Physical Metallurgy and Materials Science,* 25**,** 1127-1134.

Ennis, B. L., E. Jimenez-Melero, R. Mostert, B. Santillana & P. D. Lee (2016) The role of aluminium in chemical and phase segregation in a TRIP-assisted dual phase steel. *Acta Materialia,* 115**,** 132-142.

Ermakova, V. P., O. Y. Sheshukov & L. A. Marshuk (2010) EFFECT OF LIQUID METAL COMPOSITION AND COOLING RATE ON THE STRUCTURE OF ALLOYS OF THE SYSTEM Fe - Al. *Metal Science and Heat Treatment,* 52**,** 349-353.

Fischer, H. & M. Schaperkotter (2010) Recent developments and Future Potentials of Near Net Shape Casting Belt Casting Technology. *Thermec 2009, Pts 1-4,* 638-642**,** 3622-3627.

Flemings, M. C. 1974. *Solidification Processing*. USA: McGraw-Hill.

Fredriksson, H. 2012. *Solidification and Crystallization Processing in Metals and Alloys*. Wiley.

Fredriksson, H. & J. Stjerndahl (1982) SOLIDIFICATION OF IRON-BASE ALLOYS. *Metal Science,* 16**,** 575-585.

Fultz, B. 2014. *Phase Transitions in Materials*. Cambridge University Press.

Ganguly, S. & S. K. Choudhary (2009) Quantification of the Solidification Microstructure in Continuously-Cast High-Carbon Steel Billets. *Metallurgical and Materials Transactions B-Process Metallurgy and Materials Processing Science,* 40**,** 397-404.

Gao, H. Y., Z. X. Xie, Y. Yu, Y. Fang, J. Wang & B. D. Sun (2009) Dynamic Recrystallization Behavior of Twin Roll Cast Low Carbon Steel Strip. *Isij International,* 49**,** 546-552.

Ge, S., M. Isac & R. I. L. Guthrie (2012) Progress of Strip Casting Technology for Steel; Historical Developments. *Isij International,* 52**,** 2109-2122.

--- (2013) Progress in Strip Casting Technologies for Steel; Technical Developments. *Isij International,* 53**,** 729-742.

Ghosh, A. (2001) Segregation in cast products. *Sadhana-Academy Proceedings in Engineering Sciences,* 26**,** 5-24.

Girgensohn, A., A. R. Buchner & K. H. Tacke (2000) Twin roll strip casting of low carbon steels. *Ironmaking & Steelmaking,* 27**,** 317-323.

Glenn, A. M., S. P. Russo & P. J. K. Paterson (2003) The effect of grain refining on macrosegregation and dendrite arm spacing of direct chill cast AA5182. *Metallurgical and Materials Transactions a-Physical Metallurgy and Materials Science,* 34A**,** 1513-1523.

Glicksman, M. E. 2011. *Principles of Solidification*. Springer.

Greer, A. L., P. S. Cooper, M. W. Meredith, W. Schneider, P. Schumacher, J. A. Spittle & A. Tronche (2003) Grain refinement of aluminium alloys by inoculation. *Advanced Engineering Materials,* 5**,** 81-91.

Grässel, O., L. Krüger, G. Frommeyer & L. Meyer (2000) High strength Fe–Mn–(Al, Si) TRIP/TWIP steels development—properties—application. *International Journal of Plasticity,* 16**,** 1391-1409.

Guthrie, R. I. L. & M. Isac (2014) Horizontal Single Belt Casting of Aluminum and Steel. *Steel Research International,* 85**,** 1291-1302.

Guy, A. G. & J. J. Hren. 1974. *Elements of Physical Metallurgy*. Addison-Wesley Publishing Company Inc.

Honeycombe, R. W. K. & H. K. D. H. Bhadeshia. 1995. *Steels: Microstructure and Properties*. London: Edward Arnold.

Hurtuk, D. J. & A. A. Tzavaras (1982) SOLIDIFICATION STRUCTURES AND CONTINUOUS-CASTING OF STEEL REVISITED. *Journal of Metals,* 34**,** 40-45.

Imagumbai, M. (1994) RELATIONSHIP BETWEEN PRIMARY-DENDRITE AND SECONDARY-DENDRITE ARM SPACING OF C-MN STEEL UNI-DIRECTIONALLY SOLIDIFIED IN STEADY-STATE. *Isij International,* 34**,** 986-991.

Jacobson, N., B. Hollinger & H. Fredriksson (1993) ON THE DEVELOPMENT OF A THIN STRIPCASTER. *Scandinavian Journal of Metallurgy,* 22**,** 75-82.

Kang, S. E., A. Tuling, J. R. Banerjee, W. D. Gunawardana & B. Mintz (2011) Hot ductility of TWIP steels. *Materials Science and Technology,* 27**,** 95-100.

Kato, T., Y. Ito, M. Kawamoto, A. Yamanaka & T. Watanabe (2003) Prevention of slab surface transverse cracking by microstructure control. *Isij International,* 43**,** 1742-1750.

Kim, H., D. W. Suh & N. J. Kim (2013) Fe-Al-Mn-C lightweight structural alloys: a review on the microstructures and mechanical properties. *Science and Technology of Advanced Materials,* 14**,** 11.

Kimura, K., S. Fukumoto, G. Shigesato & A. Takahashi (2013) Effect of Mg Addition on Equiaxed Grain Formation in Ferritic Stainless Steel. *Isij International,* 53**,** 2167-2175.

Krauss, G. (2003) Solidification, segregation, and banding in carbon and alloy steels. *Metallurgical and Materials Transactions B-Process Metallurgy and Materials Processing Science,* 34**,** 781-792.

Kurz, W. & D. J. Fisher. 2005. *Fundamentals of Solidification*. Trans Tech Publications.

Lee, J. C. 2011. *Thermal Physics*

Entropy and Free energies World Scientific Publishing.

Li, X. P., J. K. Park, J. Choi & C. H. Yim (1999) The effects of ferritic transformation on hot ductility of medium carbon steel. *Metals and Materials-Korea,* 5**,** 25-32.

Lin, X., W. Huang, J. Feng, T. Li & Y. Zhou (1999) History-dependent selection of primary cellular/dendritic spacing during unidirectional solidification in aluminum alloys. *Acta Materialia,* 47**,** 3271-3280.

Liu, H. T., Z. Y. Liu, Y. Q. Qiu, G. M. Cao, C. G. Li & G. D. Wang (2009a) Characterization of the solidification structure and texture development of ferritic stainless steel produced by twin-roll strip casting. *Materials Characterization,* 60**,** 79-82.

Liu, H. T., Z. Y. Liu & G. D. Wang (2009b) Texture Development and Formability of Strip Cast 17% Cr Ferritic Stainless Steel. *Isij International,* 49**,** 890-896.

Liu, Z. Q., B. K. Li & F. Tsukihashi (2015) Instability and Periodicity of Asymmetrical Flow in a Funnel Thin Slab Continuous Casting Mold. *Isij International,* 55**,** 805-813.

Liu, Z. Y., M. Lin, D. Yu, X. W. Zhou, Y. X. Gu & H. Z. Fu (2013) Dependence of Competitive Grain Growth on Secondary Dendrite Orientation During Directional Solidification of a Ni-based Superalloy. *Metallurgical and Materials Transactions a-Physical Metallurgy and Materials Science,* 44A**,** 5113-5121.

Liu, Z. Y., Z. S. Lin, Y. Q. Qiu, N. Li, X. H. Liu & G. D. Wang (2007) Segregation in twin roll strip cast steels and the effect on mechanical properties. *Isij International,* 47**,** 254-258.

Liu, Z. Y., G. P. Zhou, Y. Q. Qiu & G. D. Wang (2010) Inversed Phosphorus Segregation in Twin Roll Cast Strips for Improvement of Mechanical Properties and Weathering Resistance. *Isij International,* 50**,** 531-539.

Lukas, H. L. 2007. *Computational Thermodynamics: The CALPHAD Method*. Cambridge University Press.

Ma, D. X. (2004) Development of dendrite array growth during alternately changing solidification condition. *Journal of Crystal Growth,* 260**,** 580-589.

Mackenzie, J. K. (1958) Second Paper on Statistics Associated with the Random Disorientation of Cubes. *Biometrika,* 45**,** 229-240.

Mahapatra, R., W. Blejde, F. Fisher, P. Campbell & G. McQuillis (2008) The Castrip process - the current status of commercial low-carbon steel strip casting. *Stahl Und Eisen,* 128**,** S107-+.

Mahapatra, R. B. & F. Weinberg (1987) THE COLUMNAR TO EQUIAXED TRANSITION IN TIN-LEAD ALLOYS. *Metallurgical Transactions B-Process Metallurgy,* 18**,** 425-432.

Makkonen, L. (2000) Spacing in solidification of dendritic arrays. *Journal of Crystal Growth,* 208**,** 772-778.

Maleki, A., A. Taherizadeh & N. Hosseini (2017) Twin Roll Casting of Steels: An Overview. *Isij International,* 57**,** 1-14.

Mapelli, C. & S. Baragiola (2008) Development of solidification microstructures in continuously cast billets of boron and resulphurised steel grades. *Ironmaking & Steelmaking,* 35**,** 441-451.

Meng, X. B., Q. Lu, X. L. Zhang, J. G. Li, Z. Q. Chen, Y. H. Wang, Y. Z. Zhou, T. Jin, X. F. Sun & Z. Q. Hu (2012) Mechanism of competitive growth during directional solidification of a nickel-base superalloy in a three-dimensional reference frame. *Acta Materialia,* 60**,** 3965-3975.

Miyake, S., H. Yamane, M. Yukumoto & M. Ozawa (1991) STRIP QUALITY OF HIGHLY ALLOYED METALS BY TWIN ROLL CASTING. *Isij International,* 31**,** 689-695.

Mizoguchi, T., K. Miyazawa & Y. Ueshima (1996) Relation between surface quality of cast strips and meniscus profile of molten pool in the twin roll casting process. *Isij International,* 36**,** 417-423.

Moon, S.-C. 2015. The Peritectic Phase Transformation and Continous Casting Practice. In *Faculty of Engineering and Information Sciences*. Research Online: Univerist of Wollongong.

Mortensen, A. (1991) ON THE RATE OF DENDRITE ARM COARSENING. *Metallurgical Transactions a-Physical Metallurgy and Materials Science,* 22**,** 569-574.

Mukunthan, K., P. D. Hodgson, P. Sellamuthu, L. Strezov, Y. Durandet & N. Stanford (2013) Castability and Microstructural Development of Iron-based Alloys under Conditions Pertinent to Strip Casting - Specialty Fe-Cr-Al Alloys. *Isij International,* 53**,** 1803-1811.

Niknafs, S. & R. Dippenaar (2014) Experimentally-aided Simulation of Directional Solidification of Steel. *Isij International,* 54**,** 526-532.

Nystrom, R., W. Reichelt & M. Dubke (2000) Strip casting experiences at MEFOS. *Scandinavian Journal of Metallurgy,* 29**,** 93-100.

Ocansey, P. M. N. & D. R. Pourier (1996) Equilibrium partition ratios of C, Mn, and Si in a high carbon steel. *Materials Science and Engineering a-Structural Materials Properties Microstructure and Processing,* 211**,** 10-14.

Pariser, G., P. Schaffnit, I. Steinbach & W. Bleck (2001) Simulation of the gamma-alpha-transformation using the phase-field method. *Steel Research,* 72**,** 354-360.

Pepper, D. W. & J. C. Heinrich. 2017. The Finite Element Method. CRC Press.

Pfeiler, W. 2007. *Alloy Physics*. Wiley-VCH.

Pickering, E. J. (2013) Macrosegregation in Steel Ingots: The Applicability of Modelling and Characterisation Techniques. *Isij International,* 53**,** 935-949.

Piekarski, B. (2010) The influence of Nb, Ti, and Si additions on the liquidus and solidus temperatures and primary microstructure refinement in 0.3C-30Ni-18Cr cast steel. *Materials Characterization,* 61**,** 899-906.

Porter, D. A., K. E. Easterling & M. Y. Sherif. 2009. *Phase Transitions in Metals and Alloys*. CRC Press, Taylor and Francis Group.

Presoly, P., R. Pierer & C. Bernhard. 2012. Linking up of HT-LSCM and DSC measurements to characterize phase diagrams of steels. In *13th International Conference on Modeling of Casting, Welding and Advanced Solidification Processes (MCWASP)*. Schladming, AUSTRIA: Iop Publishing Ltd.

Ridolfi, M. R. (2014) Hot Tearing Modeling: A Microstructural Approach Applied to Steel Solidification. *Metallurgical and Materials Transactions B-Process Metallurgy and Materials Processing Science,* 45**,** 1425-1438.

Rodriguez-Ibabe, J. M. 2007. *Thin Slab Direct Rolling of Microalloy Steels*. Switzerland: Trans Tech Publications.

Sasaki, M., K. Matsuura, K. Ohsasa & M. Ohno (2009) Effects of Addition of Titanium and Boron on Columnar Austenite Grain in Carbon Steel. *Isij International,* 49**,** 1367-1371.

Saunders, N. & A. P. Miodownik. 1998. *Calphad, Calculation of Phase Diagrams A comprehensive Guide*. Pergamon.

Schwerdtfeger, K. (2001) Belt Casting for Steel - A Critical Review. *International Report Japan***,** 59-66.

Schwerdtfeger, K., K. H. Spitzer, J. Kroos, P. Funke & K. H. Hower (2000) Further results from strip casting with the single-belt process. *Isij International,* 40**,** 756-764.

Shibata, H., S. Itoyama, Y. Kishimoto, S. Takeuchi & H. Siekiguchi (2006) Prediction of equiaxed crystal ratio in continuously cast steel slab by simplified columnar-to-equiaxed transition model. *Isij International,* 46**,** 921-930.

Shibuya, K. & M. Ozawa (1991) STRIP CASTING TECHNIQUES FOR STEEL. *Isij International,* 31**,** 661-668.

Shin, D. & J. Saal. 2018. *Computational Materials System Design*. Springer.

Software, T.-C. 2019. *References for DICTRA and its Applications*.

Sohn, S. S., B. J. Lee, S. Lee & J. H. Kwak (2013) Effects of aluminum content on cracking phenomenon occurring during cold rolling of three ferrite-based lightweight steel. *Acta Materialia,* 61**,** 5626-5635.

Sosinsky, D. J., P. Campbell, R. Mahapatra, W. Blejde & F. Fisher (2008) The CASTRIP(A (R)) process - recent developments at Nucor steel's commercial strip casting plant. *Metallurgist,* 52**,** 691-699.

Spencer, P. J. (2008) A brief history of CALPHAD. *Calphad-Computer Coupling of Phase Diagrams and Thermochemistry,* 32**,** 1-8.

Spinelli, J. E., J. P. Tosetti, C. A. Santos, J. A. Spim & A. Garcia (2004) Microstructure and solidification thermal parameters in thin strip continuous casting of a stainless steel. *Journal of Materials Processing Technology,* 150**,** 255-262.

Stefanescu, D. M. 2002. *Science and Engineering of Casting Solidification*. Kluwer Academic/Plenum Publishers.

Steinbach, I., B. Bottger, J. Eiken, N. Warnken & S. G. Fries (2007) CALPHAD and phase-field modeling: A successful liaison. *Journal of Phase Equilibria and Diffusion,* 28**,** 101-106.

StJohn, D. H., M. Qian, M. A. Easton & P. Cao (2011) The Interdependence Theory: The relationship between grain formation and nucleant selection. *Acta Materialia,* 59**,** 4907-4921.

Strezov, L. & J. Herbertson (1998) Experimental studies of interfacial heat transfer and initial solidification pertinent to strip casting. *Isij International,* 38**,** 959-966.

Sundman, B., B. Jansson & J. O. Andersson (1985) THE THERMO-CALC DATABANK SYSTEM. *Calphad-Computer Coupling of Phase Diagrams and Thermochemistry,* 9**,** 153-190.

Suwas, S. & R. K. Ray. 2014. *Crystallographic Texture of Materials*. London.

Takaki, T., S. Sakane, M. Ohno, S. Y, T. Aoki & C.-A. Gandin (2018) Competitive grain growth during directional solidification of a polycrystalline binary alloy: Three-dimensional large-scale phase-field study. *Materialia***,** 104-113.

Tilley, R. J. D. 2007. *Crystals and Crystal Structures*. John Wiley & Sons Ltd.

Tourret, D. & A. Karma (2015) Growth competition of columnar dendritic grains: A phase-field study. *Acta Materialia,* 82**,** 64-83.
Villafuerte, J. C., E. Pardo & H. W. Kerr (1990) THE EFFECT OF ALLOY COMPOSITION AND WELDING CONDITIONS ON COLUMNAR-EQUIAXED TRANSITIONS IN FERRITIC STAINLESS-STEEL GAS-TUNGSTEN ARC WELDS. *Metallurgical Transactions a-Physical Metallurgy and Materials Science,* 21**,** 2009-2019.
Volkova, O., H. P. Heller & D. Janke (2003) Microstructure and cleanliness of rapidly solidified steels. *Isij International,* 43**,** 1724-1732.
Walinjkar, D. & A. K. P. Rao (2015) C-DC and MC-DC casting of Al-alloys - A comsol approach. *Materials Letters,* 161**,** 698-700.
Wang, T. M., J. J. Xu, J. Li, W. X. Huang, S. C. Liu & T. J. Li (2010) In situ study on dendrite growth of metallic alloy by a synchrotron radiation imaging technology. *Science China-Technological Sciences,* 53**,** 1278-1284.
Wang, Y. Q., J. C. Wang & J. J. Li (2012a) Phase field modeling of the growth and competition behavior of tilted dendrites in directional solidification. *Acta Physica Sinica,* 61**,** 7.
Wang, Z. J., J. J. Li & J. C. Wang (2011) Predicting growth direction of tilted dendritic arrays during directional solidification. *Journal of Crystal Growth,* 328**,** 108-113.
Wang, Z. J., J. J. Li, J. C. Wang & Y. H. Zhou (2012b) Phase field modeling the selection mechanism of primary dendritic spacing in directional solidification. *Acta Materialia,* 60**,** 1957-1964.
Wannasin, J., R. Canyook, S. Wisutmethangoon & M. C. Flemings (2013) Grain refinement behavior of an aluminum alloy by inoculation and dynamic nucleation. *Acta Materialia,* 61**,** 3897-3903.
Wans, J., J. Bausch, J. Hecken & J. Schluter (2010) Near-net-shape casting of steel - The Belt Casting Technology. *Thermec 2009, Pts 1-4,* 638-642**,** 3634-3639.
Wasserman, A. L. 2012. *Thermal Physics*

Concepts and Practice New York: Cambridge University Press.
Wechsler, R. (2003) The status of twin-roll casting technology. *Scandinavian Journal of Metallurgy,* 32**,** 58-63.
Woodruff, D. P. 1973. *The Solid-Liquid Interface*. Cambridge University Press.
WorldSteel.org. 2016. Sustainable Steel:Policy and Indicators 2016. https://www.worldsteel.org/publications/bookshop/filter-by-subject/Sustainability.html.
---. 2017. World Steel in Figures 2017. https://www.worldsteel.org/publications/bookshop/filter-by-subject/Data-and-statistics.html.
Xu, H., L. D. Xu, S. J. Zhang & Q. Han (2006) Effect of the alloy composition on the grain refinement of aluminum alloys. *Scripta Materialia,* 54**,** 2191-2196.
Yamada, H., T. Takenouchi, T. Takahashi, M. Funazaki, T. Iwadate & S. I. Nakada (1995) INFLUENCE OF ALLOYING ELEMENTS ON THE SEGREGATION OF HIGH-PURITY CRMOV STEEL. *Isij International,* 35**,** 686-692.
Yasunaka, H., K. Taniguchi, M. Kokita & T. Inoue (1995) SURFACE QUALITY OF STAINLESS-STEEL TYPE-304 CAST BY TWIN-ROLL TYPE STRIP CASTER. *Isij International,* 35**,** 784-789.
Yi, H. L. (2014) Review on delta-Transformation-Induced Plasticity (TRIP) Steels with Low Density: The Concept and Current Progress. *Jom,* 66**,** 1759-1769.
Zapuskalov, N. & M. Vereschagin (2000) Wear of Roll Surface in Twin-roll Casting of 4.5% Si Steel Strip. *ISIJ International,* 40**,** 589-596.
Zettlemoyer, A. C. 1969. *Nucleation*. New York: Marcel Dekker Inc.
Zhang, D. & M. Strangwood (2019) Interdendritic microsegregation development of high-strength low-alloy steels during continuous casting process. *Materials Science and Technology*.
Zhang, Z. F., J. M. Kim & C. P. Hong (2005) Numerical simulation of grain structure evolution in solidification of an Al-5.0wt%Cu alloy under electromagnetic stirring and its experimental verification. *Isij International,* 45**,** 183-191.

Zhou, G. P., Z. Y. Liu, Y. Q. Qju & G. D. Wang (2009) The improvement of weathering resistance by increasing P contents in cast strips of low carbon steels. *Materials & Design,* 30**,** 4342-4347.
Zhou, G. P., Z. Y. Liu, S. C. Yu, J. Chen, Y. Q. Qiu & G. D. Wang (2011) Formation of Phosphorous Surface Inverse Segregation in Twin-Roll Cast Strips of Low-Carbon Steels. *Journal of Iron and Steel Research International,* 18**,** 18-23.
Ziv, I. & F. Weinberg (1989) THE COLUMNAR-TO-EQUIAXED TRANSITION IN AL 3 PCT CU. *Metallurgical Transactions B-Process Metallurgy,* 20**,** 731-734.